Microstructure and Tribology of Fe–Cr–B-Based Alloys

Ahmad A. Sorour

Doctor of Philosophy

Department of Mining and Materials Engineering

McGill University
Montreal

April 2014

A thesis submitted to McGill University in partial fulfillment of the requirements of the degree of Doctor of Philosophy

© Ahmad A. Sorour, 2014

Table of Contents

List of Figures

List of Tables

Abstract

Wear causes loss of materials of moving parts and tools used in many fields. Wear can be reduced by employing appropriate materials and coatings, which requires an understanding of their microstructure, properties and tribological behavior. One of the high wear resistant materials is the Fe–Cr–B-based alloy system. Fe–Cr–B-based alloys have been fabricated using thermal spray, welding and sintering processes; and it has been found that their microstructure, properties and tribological performance vary from process to process. This dissertation focuses on advances made by employing recent processes to fabricate these alloys. The primary aim of this research is to understand the microstructure and tribology of the Fe–Cr–B-based alloys fabricated by the controlled short-circuit metal inert gas (CSC-MIG) welding and spark plasma sintering (SPS) processes.

CSC-MIG was used to weld a Fe–28.2Cr–3.8B–1.5Si–1.5Mn (wt.%) cored wire alloy onto 1020 carbon steel substrate. SPS was employed to consolidate a Fe–45Cr–5.9B–2Si–0.1C (wt.%) gas-atomized powder alloy. Solidification behaviors of the gas-atomized powder and weldments were investigated through thermodynamic calculations. Microstructure characterizations, hardness measurements and tribology testings were performed for these fabricated alloys.

Upon cooling, the primary $(Cr,Fe)_2B$ phase began to form, followed by eutectic formation of the $(Cr,Fe)_2B$ and body-centered cubic (BCC) Fe-based solid solution phases. Because the powder contained a small amount of C, $(Cr,Fe)_7C_3$ was precipitated at the end of the solidification. The CSC-MIG weldment was composed of 44 wt.% primary and secondary orthorhombic $(Cr,Fe)_2B$ plates embedded in 56 wt.% BCC Fe-based solid solution, containing Fe, Cr, Mn and Si. The SPS specimen contained 65 wt.% $(Cr,Fe)_2B$ plates and 1 wt.% $(Cr,Fe)_7C_3$ precipitates dispersed in 34 wt.% BCC Fe-based solid solution, containing Fe, Cr and Si. The $(Cr,Fe)_2B$ phase was bigger in the weldment than the sintered specimen. The hardness of $(Cr,Fe)_2B$ was 24 GPa, independent of the alloy's composition and process parameters. As the B content increased, the fraction of $(Cr,Fe)_2B$ increased. As the $(Cr,Fe)_2B$ fraction increased, the bulk hardness of the specimens increased linearly. When the specimen's hardness and $(Cr,Fe)_2B$ size increased, abrasive wear resistance increased, while sliding wear resistance was independent of hardness but improved as the $(Cr,Fe)_2B$ size increased. The abrasive wear mechanism was microcutting, while sliding wear mechanisms were adhesion and mild oxidation.

Résumé

L'usage cause la perte du matériel de pièces mobiles et d'outils utilisés dans plusieurs domaines. L'usage peut être réduit en utilisant des matériaux appropriés et des revêtements dont l'utilisation demande la compréhension de leure microstructure, leures propriétés et leur comportement tribologique. Un des matériaux aillant une haute résistance à l'usage est le système d'alliage Fe–Cr–B. Les alliages à base Fe–Cr–B sont fabriqués par pulvérisation thermal, soudure et des processus de frittage. C'était découvert que la microstructure, les propriétés et la performance tribologique varie d'une procédé à l'autre. Cette dissertation est centré sur les avances conçues en utilisant des récentes procédés pour fabriquer ces alliages. Le but primaire de cette recherche est de comprendre la microstructure et la tribology des alliages Fe–Cr–B fabriqués par soudure controlled short-circuit metal inert gas (CSC-MIG) et frittage flash (SPS).

CSC-MIG était utilisé pour souder un alliage fillamenté Fe–28.2Cr–3.8B–1.5Si–1.5Mn (wt.%) sur un substrat d'acier 1020. SPS était utilisé pour consolider un alliage en poudre Fe–45Cr–5.9B–2Si–0.1C (wt.%) fabriqué par atomization à gaz. Les comportements de solidification du poudre atomizé par gaz et des soudures étaient étudiés à travers des calculs thermodynamiques. Une caractérisation microstructurielle, des mesures de dureté et des tests de tribology étaient performés pour ces alliages.

Durant la refroidissement, la phase primaire $(Cr,Fe)_2B$ a commencé à se développer suivi par une formation eutectique du $(Cr,Fe)_2B$ et de la phase en solution solide corps-centré cubique (BCC) à base de fer. Puisque la poudre contenait des petites quantités de C, le $(Cr,Fe)_7C_3$ a précipité à la fin du solidification. La soudure CSC-MIG était composée de plaques orthorhombiques de phase primaire et secondaire de $(Cr,Fe)_2B$ à 44 wt.% integré dans 56 wt.% d'une solution solide à base de Fe BCC content du Fe, Cr, Mn et Si. Le spécimen préparé par SPS contenait des plaques de 65 wt.% $(Cr,Fe)_2B$ et des précipités de 1 wt.% $(Cr,Fe)_7C_3$ dispersées dans une solution solide à base de Fe BCC de 34 wt.% aillant du Fe, Cr et Si. La phase $(Cr,Fe)_2B$ était plus grand dans la soudure que dans le spécimen fritté. La dureté du $(Cr,Fe)_2B$ était 24 GPa sans dépendance sur la composition de l'alliage ni les paramètres de procédé. Pendant que la quantité de B s'accroissait, la fraction du $(Cr,Fe)_2B$ s'accroissait aussi. Pendant que la fraction de $(Cr,Fe)_2B$ s'accroissait, la dureté entière des spécimens s'accroissait d'une façon linéaire. Quand la dureté du spécimen et la taille du $(Cr,Fe)_2B$ s'accroissaient, la résistance abrasif d'usage s'accroissait pendant que la résistance glissant d'usage était indépendant de la dureté mais s'améliorait pendant que la taille du $(Cr,Fe)_2B$ s'accroissait. Le méchanism de l'usage abrasif était la microcoupure pendant que le méchanism de l'usage glissant était l'adhésion de l'oxidation mineure.

Acknowledgments

I would like to express my deep gratitude to Richard R. Chromik and Mathieu Brochu, my supervisors, for their wise guidance, encouragement and support during my entire PhD degree. Thanks are also expressed to King Fahd University of Petroleum & Minerals (KFUPM, Dhahran, Saudi Arabia) for the scholarship granted to me to pursue the PhD program here at McGill University.

I also gratefully acknowledge Dave Shepard and Ilir A. Beta from Netzsch Instruments North America (LLC applications laboratory, Burlington, MA) for the assistance with DSC measurements, Liquidmetal Coatings (CA, USA) for the supply of the Armacor M powder, Steven Budinsky from Bud Labs (Rochester, NY, USA) for the assistance with the abrasive wear testing, Michel Trudeau and Lisa Rodrigue from the Institut de Recherche d'Hydro-Québec (IREQ, Varennes, Canada) for the thin foil preparation, and Zhanli Guo from Surrey Technology Centre (Guildford, UK) for the assistance with the high temperature flow stress simulation.

Thanks also go to the members of the two research groups I worked with. Special thanks are expressed to Jason Milligan for his help with SPS, David Heard and Patrick Vespa for assistance with CSC-MIG, Holger W. Strauss for construction of the tribometer apparatus and Pantcho Stoyanov for assistance with AFM. I would like to thank all the lab technicians who helped me in carrying out the experiments, and

especially, Nicolas Brodusch, Monique Riendeau and Helen Campbell for assistance with SEM and XRD. Acknowledgments are also due to all of the other staff members of the department for their administrative and technical assistance, including but not limited to Barbara Hanley, Robert Paquette and Florence Paray.

Gratitude is also extended to everyone else not listed here, who have in some way or another contributed to any stage of this research.

Preface and Contribution of Authors

This dissertation is based on a collection of manuscripts that were published in peer-reviewed journals or are in the process of being published. I am the primary author for all of the manuscripts included in this dissertation. I have performed the experimental work, analyzed the resulting data and written the manuscripts.

Other contributors of these manuscripts were included as co-authors. Richard R. Chromik and Mathieu Brochu supervised this PhD research and reviewed all of the manuscripts. Raynald Gauvin provided access to the SU8000 SEM and reviewed the manuscript in Chapter 4. In-Ho Jung helped with FactSage thermodynamic calculations and reviewed the manuscript in Chapter 4. Holger W. Strauss was included as a co-author of the manuscript in Chapter 7 for his help in the tribometer construction.

CHAPTER 1

Introduction

Tribology is defined by Oxford dictionary as "The branch of science and technology concerned with interacting surfaces in relative motion and with associated matters (as friction, wear, lubrication, and the design of bearings)." Friction and wear cause significant loss of energy and materials of moving parts and tools used in the fields of transportation, power generation, turbomachinery and industrial processes [1–4]. Energy dissipation due to undesired friction can be simply reduced by introducing a lubricant interfacial film. However, loss of materials due to undesired wear cannot be easily mitigated. It has been shown that a slight improvement in wear resistance contributes to a significant economical saving, better efficiency, better performance, and fewer breakages. Wear resistance can be improved by using appropriate materials, coatings and surface modifications [2, 5]. To select the best material, we need to understand the microstructure, properties and tribological behavior of the materials used.

One of the material classes that is becoming more frequently used in applications requiring excellent wear resistance is a metal matrix composite (MMC). The MMCs are multiphase materials that have many advantages over monophase materials,

including improved strength, modulus and wear resistance [6]. They can be used as bulk materials or coatings on a metallic substrate. The MMCs usually consist of a metallic matrix with embedded ceramic reinforcing phases. The reinforcing phase can have various sizes and shapes, such as continuous fibers, discontinuous fibers, whiskers and particulates (platelets) [6]. The reinforcing phase possesses high hardness and strength while the matrix is weaker, softer and tougher. Ideally, these composites combine the best and suppress the worst properties of the individual phases, yielding high hardness and fracture toughness. The MMCs are tailorable materials; that is, their properties can be controlled by microstructural parameters: the hardness, shape, size, fraction and orientation of the reinforcing phase as well as the properties of the matrix and the interfacial bonding between the reinforcing phases and the matrix [7].

Fe–Cr–B-based alloys are MMCs. They usually contain a ferritic α-Fe-based matrix with embedded hard $(Cr,Fe)_2B$ boride reinforcement [8–14]. It has been shown that the Fe–Cr–B-based alloys have high hardness [9–12, 14] and exhibit high sliding and abrasive wear resistance [8, 11, 14–17]. These alloys have been extensively deposited by thermal spray processes: the twin wire arc thermal spray (TWAS) [18, 19], high velocity oxygen fuel (HVOF) [9, 14, 16, 19–22] and detonation gun [13, 23–25]. They have also been deposited by welding processes: plasma transferred arc (PTA) [9,10,20] and high-energy electron beam irradiation (HEEBI) [8, 17, 26]. Along with these deposition methods, consolidation of gas-atomized Fe–Cr–B-based alloy powders has been reported, including powder-injection molding (PIM) [11, 15, 27], metal injection molding [28], supersolidus liquid-phase sintering (SLPS) [29] and hot-isostatic pressing (HIP) [29].

It has been shown that the microstructure of Fe–Cr–B-based alloys is affected by the process parameters and the alloy's composition. While the shape and size of $(Cr,Fe)_2B$ vary from process to process [29], the fraction of $(Cr,Fe)_2B$ is mainly controlled by the B content [30]. The size, shape and fraction of the $(Cr,Fe)_2B$ phase determine the properties and wear performance of the Fe–Cr–B-based alloys [8–12, 27, 30]. Since the performance and properties of the Fe–Cr–B-based alloys are affected by their microstructure that is determined by the fabrication process, the selection of the fabrication process is important. In this research, the Fe–Cr–B-based alloys were fabricated using two of the most effective and advanced welding and sintering processes: controlled short-circuit metal inert gas (CSC-MIG) welding and spark plasma sintering (SPS).

The CSC-MIG welding process is a modified version of the MIG welding process [31]. In CSC-MIG, the position and speed of the electrode wire are controlled to achieve the short circuiting mode and thus to reduce the heat input and spatter while increasing transfer rate [31]. While the conventional MIG process is one of the most widely used arc welding processes for metals and alloys, the CSC-MIG process provides many advantages when compared to MIG, such as higher transfer rate, lower heat input and higher welding stability, which results in negligible spatter [31].

The SPS process uses uniaxial pressure and a pulsed high-DC current to sinter powders [32]. The SPS process has many advantages over conventional sintering processes, including higher heating rate, lower sintering temperature, shorter holding time, complete consolidation of difficult-to-sinter powders, and elimination of the need for sintering aids [32–34]. In addition, the SPS process produces materials

with improved properties, such as mechanical, optical and electrical properties [32]. Moreover, it can be used as cladding or for co-sintering of dissimilar powders to fabricate clad layer.

Outline

This dissertation has been organized in a manuscript-based style and contains eight chapters. Chapter 1 presents the context and rationale of the current research. It also provides the outline of this dissertation. Chapter 2 presents the fundamental background and a literature review of the processes used, the Fe–Cr–B-based alloys and tribology. Chapter 3 states the primary aim of this research and describes the overall approach and methodology utilized to achieve the objectives.

The following four chapters present studies containing the results and discussion as well as a specific literature review and the experimental procedures appropriate to each study. Chapter 4 presents the solidification and microstructure of the Fe–Cr–B-based alloy that was fabricated by the CSC-MIG process. Chapter 5 presents the hardness and tribology of the Fe–Cr–B-based alloy fabricated by the CSC-MIG process. Chapter 6 presents the densification and microstructure of the Fe–Cr–B-based alloy fabricated by the SPS process. Chapter 7 presents the hardness and tribology of the Fe–Cr–B-based alloy fabricated by the SPS process.

The dissertation ends with final conclusions (Chapter 8). It includes the general summary that reflects the entire body of research presented in all manuscripts, the original contribution to the advancement of knowledge in the research area and ideas for future directions.

CHAPTER 2

Background and Literature Review

This chapter presents the fundamental background and a review of the literature. It is divided into three sections. Section 2.1 delivers the background on the welding and sintering processes used in this research. Section 2.2 provides the basic background and the reported characterization findings of the Fe–Cr–B-based alloys. Section 2.3 provides the fundamental background about tribology in general and the tribology of MMC materials in particular. In addition, it focuses on what researchers have managed to obtain about the effects of microstructure and hardness for the Fe–Cr–B-based alloys on the wear performance and behavior.

2.1 Fabrication Processes

2.1.1 Welding

Welding is a process that makes two parts one by obtaining continuity between the parts [35]. Metallurgical continuity and bringing atoms together can be established by one or more of three mechanisms: diffusion, mechanical force and epitaxy [35].

Table 2.1 lists examples of welding techniques classified according to the nature of the energy transfer process used to obtain the continuity at the boundary [35].

Table 2.1: Welding techniques classified according to the nature of the energy transfer process [35]

Transfer process	Examples
Gas	gas fusion welding
	brazing or braze welding
Electric arc	TIG welding
	arc welding with electrode
Radiation	electron beam welding
	laser welding
Mechanical effect	friction welding
	ultrasonic welding
Electric current passage	resistance spot welding
	resistance brazing

Fusion welding is a joining process that uses fusion of the base metal to create the weld [36]. Table 2.2 presents the heat sources and examples of welding techniques for each fusion welding type. As the power density of the heat source increases, the heat input to the workpiece decreases (Figure 2.1). In the gas welding, the portion of the workpiece material exposed to a gas flame heats up very slowly and before any melting can occur, a large amount of heat is already absorbed by the bulk of the workpiece [36]. Excessive heating can cause damage to the workpiece, such as weakening and distortion. On the contrary, the same material exposed to a sharply focused electron or laser beam can melt a small portion of the workpiece; and before much heat is absorbed by the workpiece, welding is completed [36].

Table 2.2: Fusion welding process types, heat sources and techniques [36]

Fusion welding type	Heat source	Welding process
Gas welding	gas flame	oxyacetylene welding (OAW)
Arc welding	electric arc	shielded metal arc welding (SMAW) gas-tungsten arc welding (GTAW) plasma arc welding (PAW) gas-metal arc welding (GMAW) flux-cored arc welding (FCAW) submerged arc welding (SAW)
High-energy beam welding	high-energy beam	electron beam welding (EBW) laser beam welding (LBW)

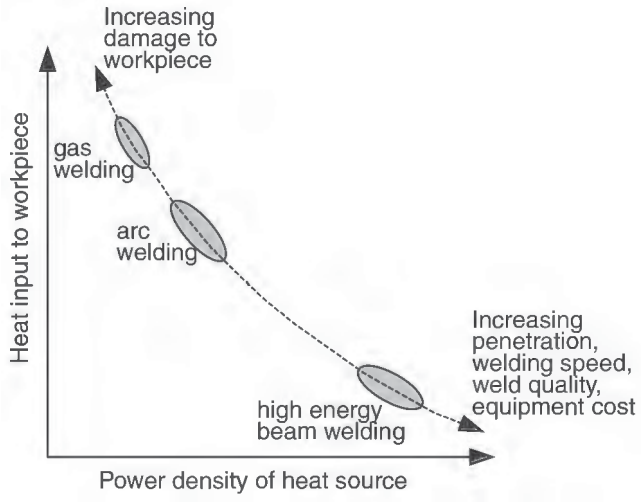

Figure 2.1: Heat input to the workpiece vs. power density of the heat source [36]

The GMAW/MIG process

Gas-metal arc welding (GMAW), or metal-inert gas (MIG), is a welding process that melts and joins materials by heating them with an arc generated between a continuously fed consumable wire electrode (anode) and a workpiece (cathode) [36], as illustrated in Figure 2.2. The energy flux of the arc melts the wire electrode to form droplets and part of the workpiece to form a weld pool. The arc and the molten weld pool are usually shielded by inert (argon, nitrogen or helium) or noninert (CO_2) gases [36]. This process is one of the most widely used arc welding processes for metals and alloys. While the GMAW process provides a high deposition rate at any angle/position, its gun has difficulty in reaching small areas and corners.

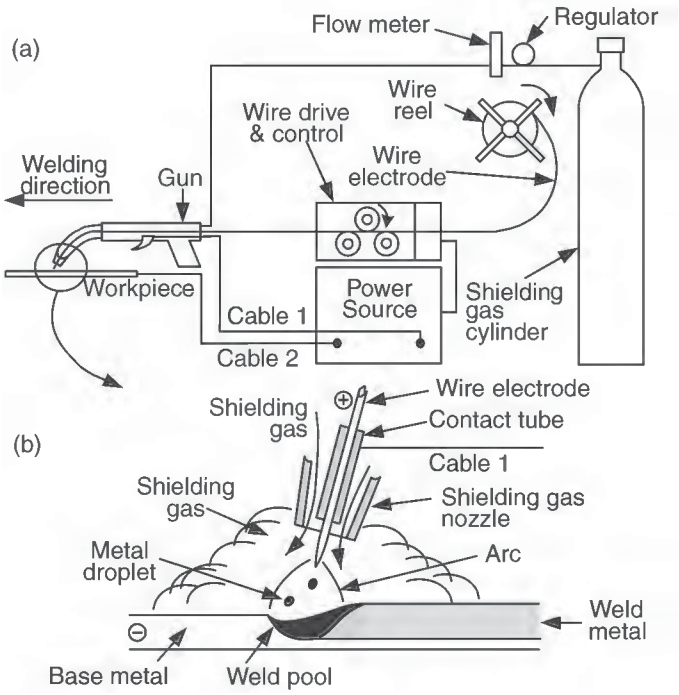

Figure 2.2: Gas-metal arc welding (a) overall process and (b) welding area [36]

The molten droplets at the electrode tip are transfered to the weld pool by one of three modes: globular, spray or short-circuit [36]. The globular transfer mode (Figure 2.3a) occurs at a low welding current, which forms large droplets (larger than the wire's diameter). Since the electromagnetic forces from the welding current are low compared to the surface tension force at the wire's tip, the transfer rate is low. The transfer rate can be improved by increasing the current. When the current reaches a high critical level, the spray transfer mode occurs (Figure 2.3b). In the spray mode, welding stability is improved and spatter is avoided. However, this high current generates a high heat input that overheats the workpiece and causes distortion. To overcome these drawbacks, the short-circuit transfer mode should be utilized. In this mode, both the voltage and current are kept low until a droplet is formed. Then, the wire is moved quickly toward the substrate to periodically dip the electrode tip into the weld pool to release the droplet into the pool.

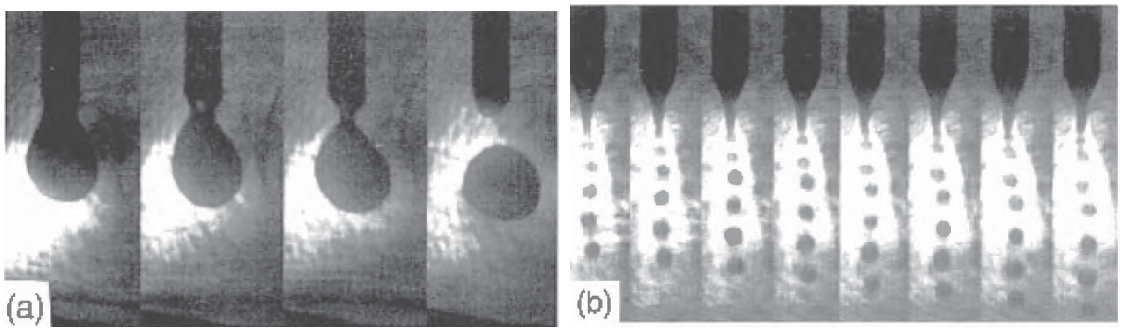

Figure 2.3: Material transfer during the GMAW process: (a) globular and (b) spray transfer [36]

The CSC-MIG process

The controlled short-circuit metal inert gas (CSC-MIG) process [31, 37] , also called the cold metal transfer (CMT) process [38], is a modified version of the MIG welding process. In the CSC-MIG process, the position and speed of the electrode wire are controlled to achieve the short-circuit mode and thus to reduce the heat input and spatter [31].

The CSC-MIG process comprises four phases [31], as demonstrated in Figure 2.4. First, the current is applied to generate the arc (Figure 2.4a) that melts the wire tip (forming the droplet) and the portion of the substrate (forming the weld pool). Then, the wire is moved toward the substrate (Figure 2.4b) until the droplet contacts the weld pool, at which point the short-circuit phase begins (Figure 2.4c). During this phase, the droplet is transfered to the pool. Finally, the wire is retracted (Figure 2.4d) to break the liquid connection between the wire tip and the weld pool. Figure 2.5 shows the transitions of current and voltage during the process. High voltage and current are applied to generate the arc (phase a), while low voltage and current occur at the short-circuit activation (phase c).

The main advantages of the CSC-MIG process over the conventional MIG process are higher transfer rate, lower heat input and higher welding stability, which leads to negligible spatter [31]. It has been used for the fabrication of carbon and low alloy steels [37]. It is suitable for joining thin sheet steel and for all welding of thicker sections [37].

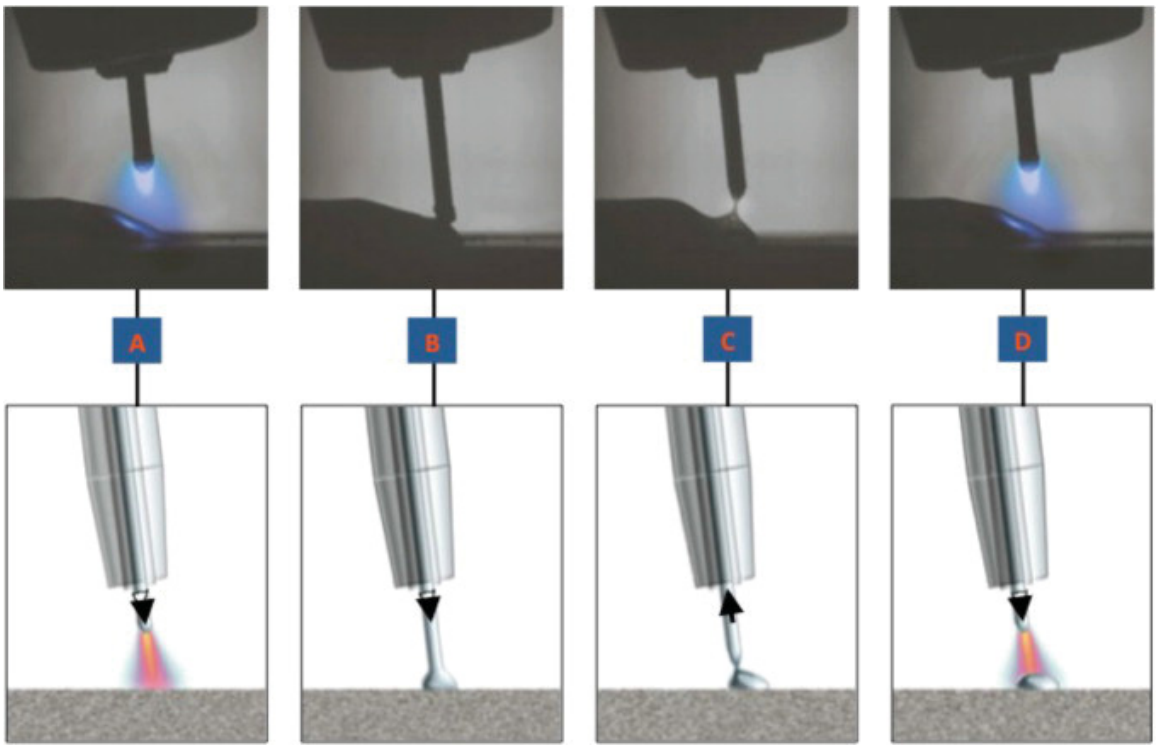

Figure 2.4: The CSC-MIG process phases [37]
(a) arc initiation
(b) wire feeding
(c) short-circuit
(d) wire retracting

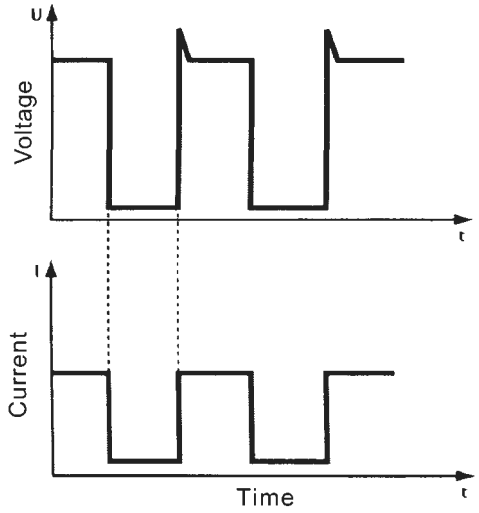

Figure 2.5: Transitions of current and voltage during the CSC-MIG process [38]

2.1.2 Sintering

Sintering has been utilized for thousands of years. In 6000 BC, the ancient civilization of Mesopotamia formed bricks by heating clay blocks [32]. In 3000 BC, the ancient Egyptians sintered metals and ceramics [32]. The Incas of South America used sintering to fabricate gold-platinum jewelry [32]. Solid-state sintering of metals and alloys began during the period of 1920–1950 [32].

Figure 2.6 presents different techniques developed to sinter materials. Sintering with the aid of pressure, as in the hot isostatic pressing (HIP) process, is the most commonly used. In HIP, the cycle can last up to eight hours or even more. Sintering can also be activated and enhanced by the use of an electromagnetic field, known as electric current activated/assisted sintering (ECAS) [32, 33]. The use of a current or electric discharge to aid the sintering of powders was patented as early as 1933 [32]. Research on spark sintering was performed by Lenel at RPI by scientists at the

Lockheed Missile and Space Company (CA, USA) in the 1950s and Inoue (Japan) in the 1960s and 1970s [32]. Over the past few decades, commercial units have been developed, including plasma-assisted sintering (PAS), pulse electric current sintering (PECS), electric pulse assisted consolidation (EPAC) and spark plasma sintering (SPS) [32, 39].

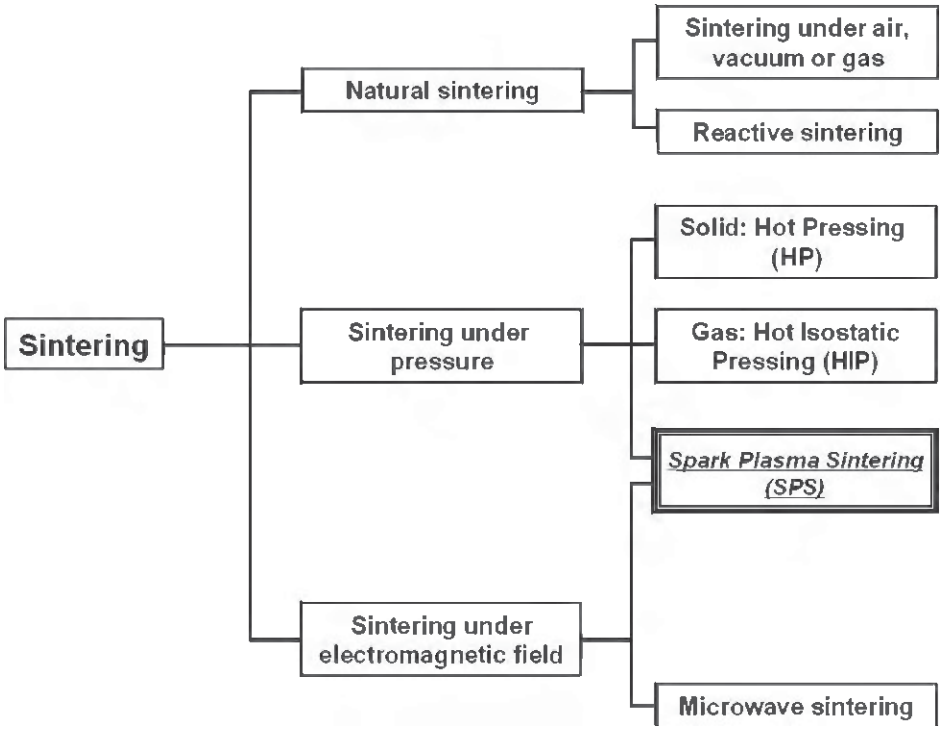

Figure 2.6: Sintering techniques [39]

The use of an electric current with simultaneous application of pressure in sintering provides many advantages over conventional methods. It yields a higher heating rate, lower sintering temperature, shorter holding time, complete consolidation of difficult-to-sinter-powders, elimination of the need of sintering aids, and marked comparative improvements of the properties of consolidated materials [32–34]. The

lower sintering temperatures and shorter processing times allow nanomaterial or metastable powders to be sintered with near theoretical density, little grain growth, little retention of metastability, minimum loosed materials by vaporization and clean grain boundaries [32–34]. Moreover, the shorter processing time can prevent undesired phase transformations or reactions in the starting powders [33, 34]. Therefore, shorter processing times and lower sintering temperatures result in economic and productivity gains [33, 34].

In solid state sintering, the sintering temperature is slightly above 70% melting point [39]. Sintering is affected by powder characteristics (morphology, grain size), process parameters (temperature, pressure, holding time) and atmosphere (vacuum, oxidation, inert gas) [39].

The SPS process

The spark plasma sintering (SPS) process is one of the most common processes used to consolidate powders under the simultaneous application of uniaxial pressure and a pulsed-high DC current [32]. The applied mechanical pressure and electric current can be constant or vary during the sintering stages [33]. The pressure has a direct effect on particle re-arrangement and the destruction of agglomerates [32]. The current provides Joule heating to the die and powder. In addition, the current creates plasma that is proposed to clean the particles' surface, which aids sintering [32].

Figure 2.7a shows the schematic of the SPS process. It consists typically of a vacuum chamber, electrodes, and a power supply. Figure 2.7b presents a schematic of the die/powder system. The die and plunger are usually made of high-purity/high-

density graphite. SPS can sinter single powder or dissimilar multiple powders. It has been shown that the SPS process produces materials with improved mechanical, optical, electrical, oxidation and corrosion properties [32]. To date, the SPS process has been successfully used to sinter only small and simple-shape parts. This is due to the lack of providing adequate electric current and homogeneous temperature distribution, which are very sensitive to the homogeneity of the density distribution [33].

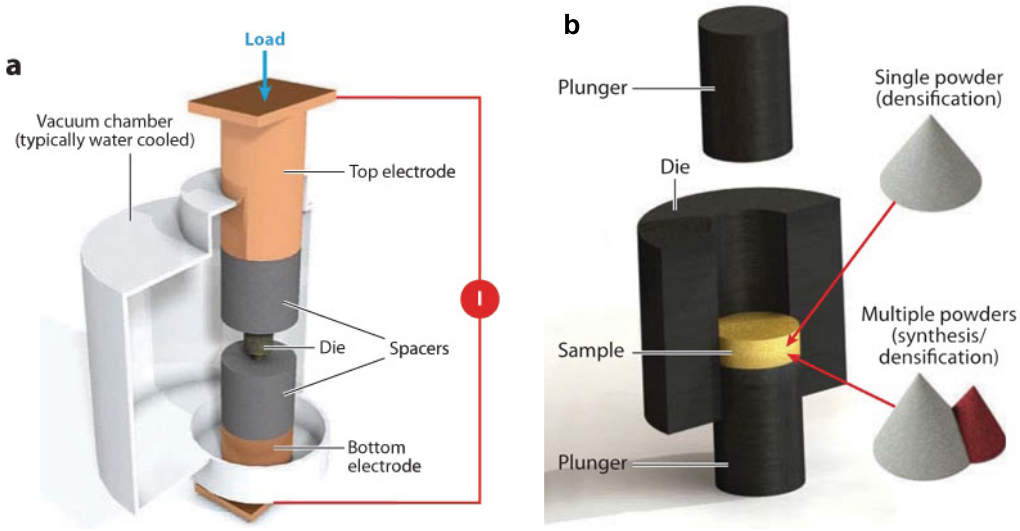

Figure 2.7: Schematic of (a) the SPS apparatus and (b) the die, plungers and powder [40]

Densification is the removing of porosity from the powder compact to produce low or free-pore material (95-98% of theoretical density) [40]. Zhaohui et al. [41] proposed the following sintering mechanisms; 1) activation and refining of the powder, 2) formation and growth of the sintering neck, 3) rapid densification and 4) plastic deformation densification. The activation and refining of the powder and the formation of the sintering neck stages are promoted by the spark discharge between particles.

This removes the powder surface oxide and favors the formation of the neck. The growth of the sintering neck, rapid densification and plastic deformation densification stages are promoted by the current that flows through the neck and heats up the powder by Joule effect. Figure 2.8 shows the transport mechanisms during sintering. While all of them promote neck formation, not all cause densification. Evaporation and surface diffusion do not cause densification but rather cause particle coarsening. To maximize densification, mass transport mechanisms that cause densification should be promoted.

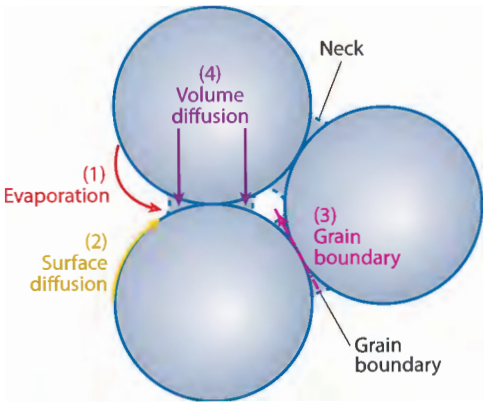

Figure 2.8: Mass transport mechanisms in sintering [40]

Helle et al. [42] have developed equations to calculate the plastic flow contribution to densification during hot-isostatic pressing. Densification by plastic deformation is instantaneous, and thus it can be calculated by:

$$\theta_{yield} = \left(\frac{(1-\theta_0)P}{1.3\sigma_y} + \theta_0^3 \right)^{\frac{1}{3}} \qquad \theta < 0.9 \tag{2.1}$$

$$\theta_{yield} = 1 - exp\left(-\frac{3P}{2\sigma_y}\right) \qquad \theta > 0.9 \tag{2.2}$$

where θ_{yield} is the relative density due to plastic yielding, θ_0 is the initial density, P is the applied pressure and σ_y is the flow stress of the material. Equation 2.1 is used for the initial stage ($\theta < 0.9$), when the powder particles are still recognizable and the densification is modeled by the growth of necks [42]. Equation 2.2 is applied for the final stage ($\theta > 0.9$), in which the remaining porosity is modeled as spherical holes that shrink as sintering proceeds [42].

Olevsky and Froyen [43] developed a constitutive model to describe the strain rates of the densification during SPS. The model takes into account power-law creep due to external load (Eq. 2.3), grain boundary diffusion due to external load (Eq. 2.4), electromigration due to electric current (Eq. 2.5) and sintering stress due to surface tension (Eq. 2.6) [43].

$$\dot{\varepsilon}_{crx} = -\left\{\left(\frac{3\theta}{2}\right)^{\frac{3}{2}}\left[\frac{3\alpha}{2G}(1-\theta)^2 - \bar{\sigma}_x\right]/A\,(1-\theta)^{\frac{5}{2}}\right\}^{\frac{1}{m}} \tag{2.3}$$

$$\dot{\varepsilon}_{gbx}^{load} = \frac{\delta_{gb}D_{gb}}{kT}\frac{\Omega}{(G+r_p)}\frac{\bar{\sigma}_x}{G^2} \tag{2.4}$$

$$\dot{\varepsilon}_{gbx}^{em} = -\frac{\delta_{gb}D_{gb}}{kT}\frac{Z^*e_q}{(G+r_p)^2}\frac{U}{l} \tag{2.5}$$

$$\dot{\varepsilon}_{gbx}^{st} = -\frac{3\delta_{gb}D_{gb}}{kT}\frac{\Omega}{(G+r_p)^2}\frac{\alpha}{G}\left[\frac{1}{r_p} - \frac{1}{2G}\right] \tag{2.6}$$

where $\delta_{gb}D_{gb}$ is the grain boundary diffusion coefficient, Ω is the atomic volume, k is Boltzmann's constant, T is the temperature, G is the particle size, r_p is the pore radius, m is the power-law creep exponent, Z^*e_q is the effect charge, U/l is the applied field and α is the surface tension.

The total strain (shrinkage) rate, $\dot{\varepsilon}_{total}$, can thus be calculated by Equation 2.7 and the total densification rate, $\dot{\theta}$, can then be calculated by Equation 2.8 as follows:

$$\dot{\varepsilon}_{total} = \dot{\varepsilon}_{crx} + \dot{\varepsilon}_{gbx}^{load} + \dot{\varepsilon}_{gbx}^{em} + \dot{\varepsilon}_{gbx}^{st} \tag{2.7}$$

$$\dot{\theta} = (1-\theta)\dot{\varepsilon}_{total} \tag{2.8}$$

Milligan et al. [44] added to the Olevsky and Froyen model the Helle et al. [42] equations to describe the densification of Al–12%Si alloy. The overall relative density, with all of these mechanisms, can be numerically calculated by [44]

$$\theta(t) = \dot{\theta} \times \Delta t + \Delta\theta_{yield} \tag{2.9}$$

where Δt is the time step and $\Delta\theta_{yield}$ is the change in density due to plastic flow, which changes as a function of temperature.

2.2 Fe–Cr–B-based Alloys

2.2.1 Phase Analysis

Solubility

The B solubility in an Fe-based alloys containing Cr has been found to be negligible. Guo and Kelly [45] found that the solubitity in an as-cast ferrite was 0.2–0.5 wt.%, and it decreased to 0.02–0.06 mass% after 750 ℃ tempering. When B content exceeds its solubility limit in Fe and Cr alloys, boride phases precipitate. These precipitates are typically Fe borides (FeB and Fe_2B) and/or Cr borides (CrB and Cr_2B).

It has been shown that third elements can replace Cr and Fe in these borides to form solid solutions without changing their structure. That is, about two-thirds of the Cr atoms in Cr_2B can be replaced by Fe, and the resulted phase is conventionally referred as $(Cr,Fe)_2B$ [46–48]. Figure 2.9 shows the solubility limit of Fe or Cr in Cr_5B_3, Cr_2B and Fe_2B as a function of temperature. Between 800–1000 ℃, about 60 at.% of Cr can be replaced by Fe for the Cr_2B phase. At 1250 ℃, the extension of Cr_2B reaches the composition $(Cr_{0.3}Fe_{0.7})_2B$, and for Fe_2B it is up to $(Cr_{0.25}Fe_{0.75})_2B$. The solubility limit of third elements in Cr and Fe borides is important to thermodynamically model the $(Cr,Fe)_2B$ and $(Fe,Cr)_2B$ solid solutions.

Alloying element addition, such as Si, Mo and Ni, cannot dissolve in the borides of the Fe–Cr–B-based alloys but diffuse into the matrix. In the boronized AISI 440C stainless steel, Cr and Mn dissolved in the coating by substituting Fe for Fe_2B and FeB, while Si was insoluble in the borides and precipitated at the interface with the coating [55].

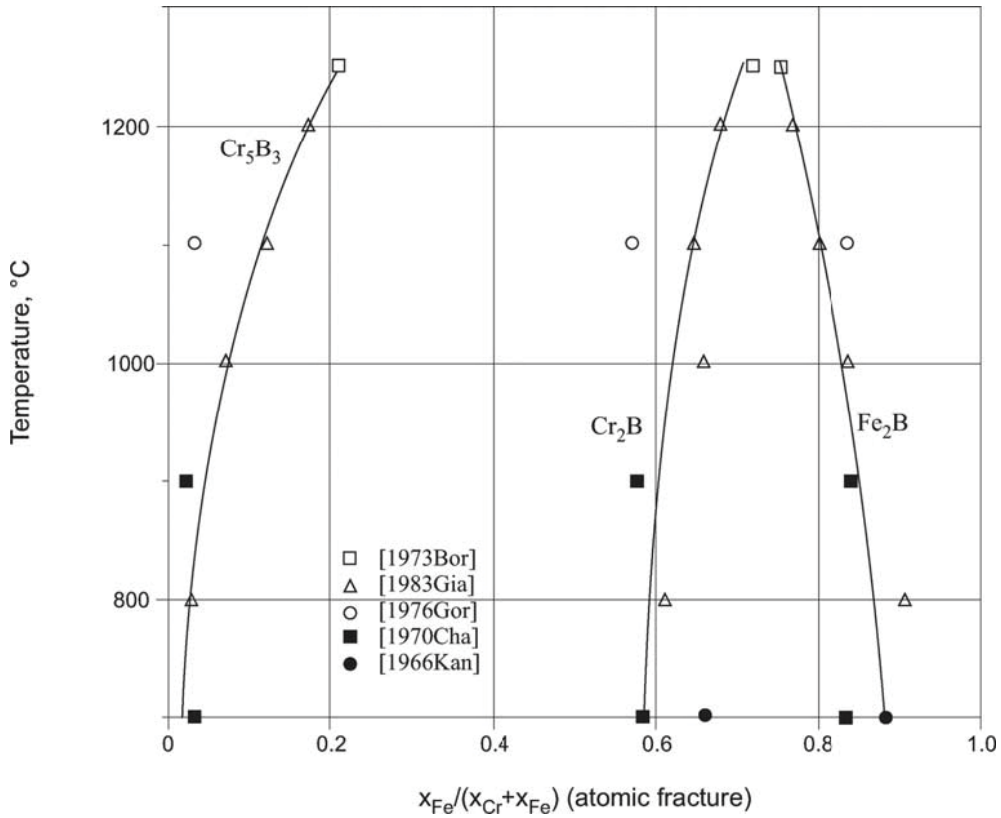

Figure 2.9: Composition of Cr_5B_3, Cr_2B and Fe_2B boride phases with the maximal solubility [49]. The curves were fitted on experimental data from 1973Bor [50], 1983Gia [51], 1976Gor [52], 1970Cha [53] and 1966Kan [54].

Estimating the Composition of Cr_2B

Table 2.3 presents the lattice parameters of Cr_2B as a function of the dissolved Fe content. As Fe content increases, the lattice parameters are reduced. Brown and Beernsten [46] found that the orthorhombic lattice parameters for a single crystal of $Cr_{0.9}Fe_{1.1}B_{0.9}$ were $a = 14.57$ Å, $b = 7.32$ Å, and $c = 4.22$ Å. Aronsson and Aselius [47] found that the lattice parameters for the boride with a similar Cr/Fe ratio were $a = 14.58$ Å, $b = 7.33$ Å, and $c = 4.21$ Å.

Table 2.3: Lattice parameters of $(Cr,Fe)_2B$ as a function of Fe content (at.%) [48]

Cr/(Fe+Cr)	a (Å)	b (Å)	c (Å)
1.00	14.7118	7.4090	4.2499
0.48	14.5830	7.3799	4.2452
0.34	14.5100	7.2550	4.2335
0.22	14.2781	7.2237	4.2300

Kayser and Kayser [56] established the relation between the composition of $(Cr,Fe)_2B$ in Fe–Cr–B alloys as a function of the measured lattice parameters (a, b and c), as shown in Figure 2.10. Christodoulou and Calos [48] measured the lattice parameters of $(Cr,Fe)_2B$ with various chemical compositions and established a similar relation (Figure 2.11). They found that the lattice parameters were in a good agreement with that measured by EPMA and presented in Table 2.3. This relation is linear, and it can be described by

$$a = 14.608 - 0.046(Fe/Cr) \tag{2.10}$$

where Fe/Cr ratio represents the weight ratio. These results (Figures 2.10 and 2.11) were used in this research to estimate the composition of the $(Cr,Fe)_2B$ phase. The lattice parameters of $(Cr,Fe)_2B$ were experimentally measured by the XRD analysis.

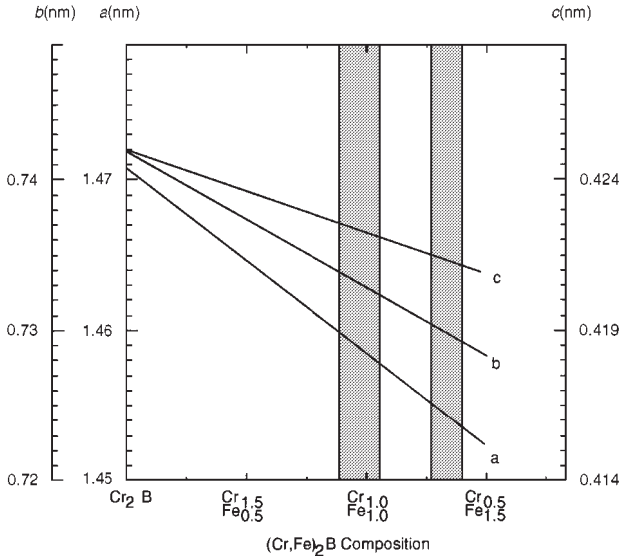

Figure 2.10: Lattice parameters as a function of the Fe and Cr concentration (at. %) in $(Cr,Fe)_2B$ [56]

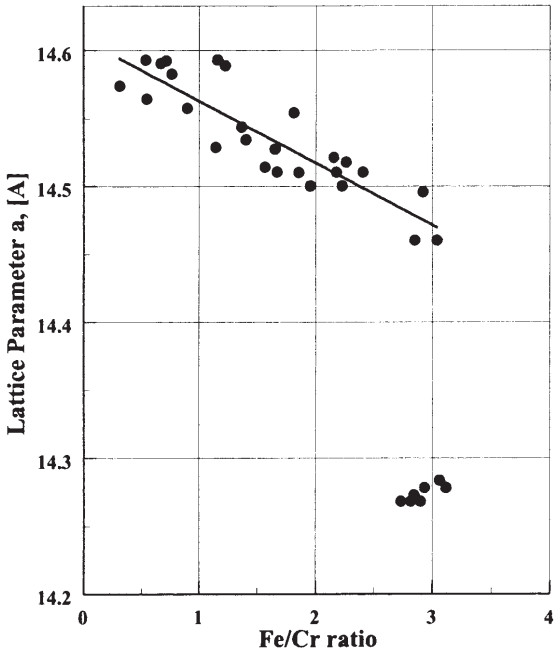

Figure 2.11: Lattice parameter a vs. Fe/Cr ratio (wt.%) for the orthorhombic $(Cr,Fe)_2B$ phase [48]

Phase Equilibria

Phase equilibriums of the ternary Fe–Cr–B alloy system have been studied [49–54]. Figure 2.12 shows the partial liquidus surface projection of the ternary Fe–Cr–B alloy system (up to 20 at.% Cr and 30 wt.% B). This diagram can provide overall information about the phases evolution during solidification. However, a more detailed diagram need to be reproduced to cover the full range of Cr and up to 30 at.% B.

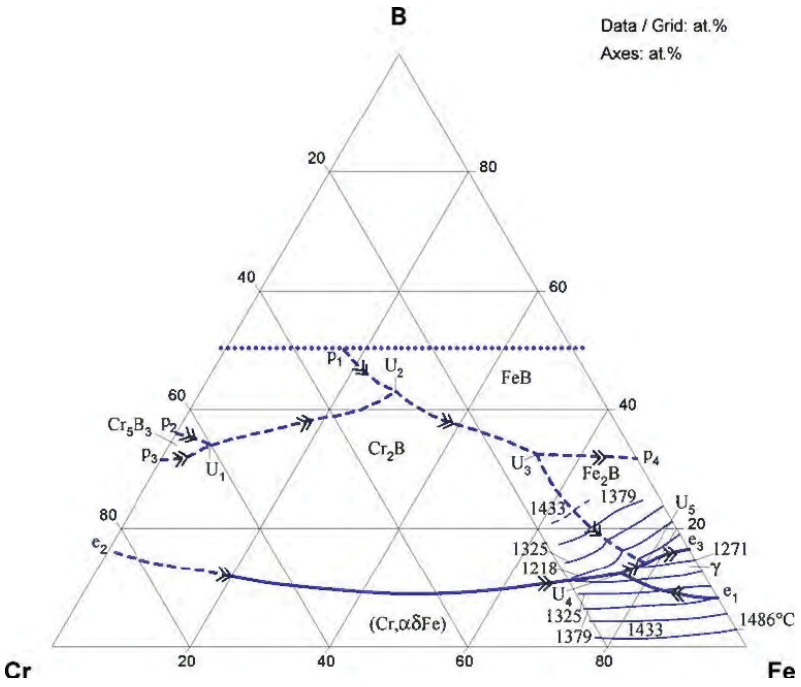

Figure 2.12: Partial liquidus surface projection for B–Cr–Fe system [49]

Figure 2.13 shows the isothermal phase diagrams of the ternary Fe–Cr–B alloy system at 1250 ℃ [50], 1100 ℃ [51, 52], 900 ℃ [53], and 700 ℃ [53, 54]. These diagrams were created at a period between 1966–1983. The dotted lines represent results that had not been fully confirmed at that time. In this system, no stable ternary compounds were found [49]. These diagrams identify the equilibrium phases for the Fe–Cr–B alloy, without alloying elements, at specific temperatures. Therefore, in this research, the thermodynamic calculations were performed to take into account other alloying elements (Si, Mn and C) and all temperature range.

Recently, Do et al. [12] calculated the isothermal phase diagrams of the ternary Fe–Cr–B system using the Thermo-Calc thermodynamic calculation program and TCFE2000 database, as shown in Figure 2.14. These diagrams agree with the diagrams in Figure 2.13b and d. They calculated the volume fractions of $(Cr,Fe)_2B$ using the thermodynamic analysis, and they were 5% less than that measured by image analysis. Hence, in the current research, the volume fraction of the phases composed the Fe–Cr–B alloys were calculated by the thermodynamic analysis and compared to the measured ones by image analysis.

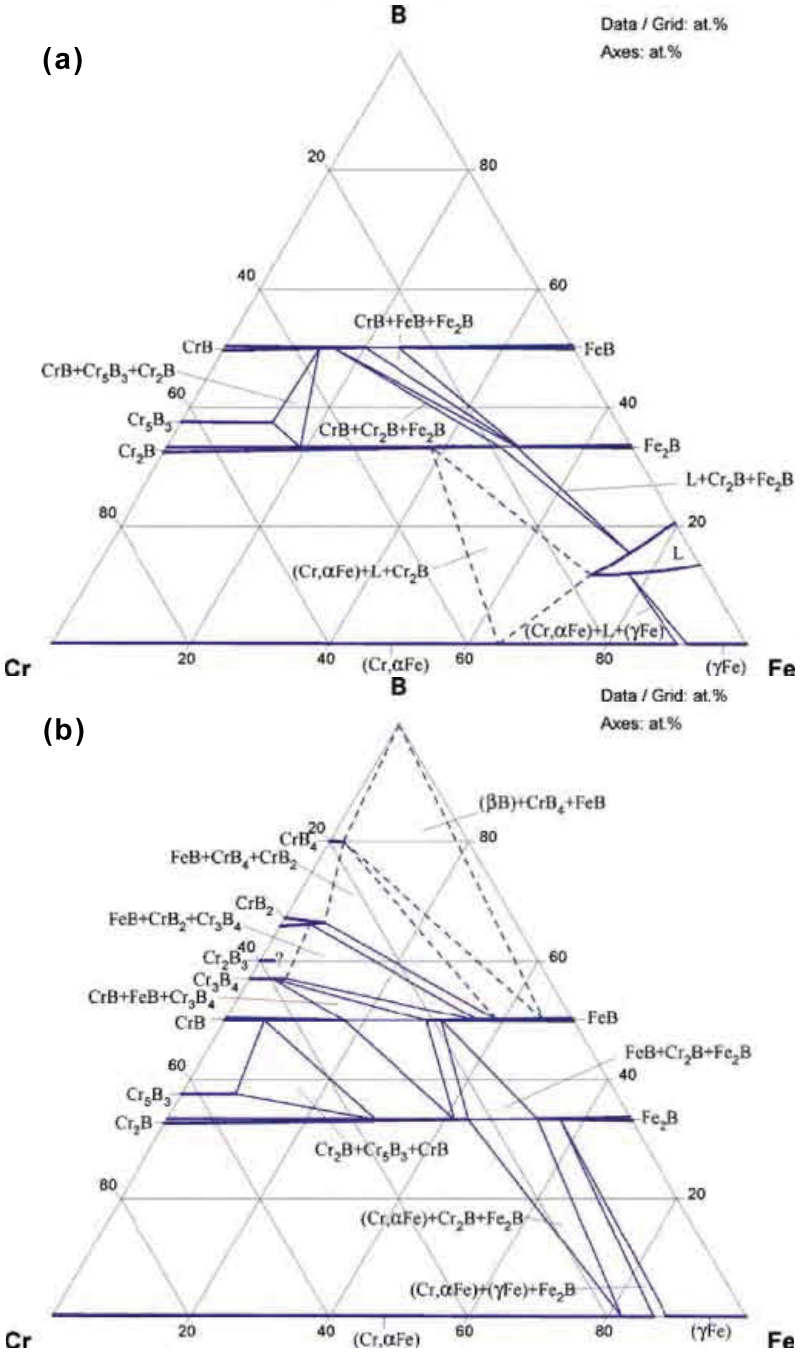
(a)
B
Data / Grid: at.%
Axes: at.%
20
80
40
60
CrB+FeB+Fe2B
CrB
FeB
CrB+Cr5B3+Cr2B
60
40
Cr5B3
CrB+Cr2B+Fe2B
Cr2B
Fe2B
L+Cr2B+Fe2B
80
20
L
(Cr,αFe)+L+Cr2B
(Cr,αFe)+L+(γFe)
Cr
20
40
(Cr,αFe)
60
80
(γFe)
Fe
(b)
B
Data / Grid: at.%
Axes: at.%
(βB)+CrB4+FeB
20
80
CrB4
FeB+CrB4+CrB2
CrB2
FeB+CrB2+Cr3B4
40
60
Cr2B3
?
Cr3B4
CrB+FeB+Cr3B4
CrB
FeB
FeB+Cr2B+Fe2B
60
40
Cr5B3
Cr2B
Fe2B
Cr2B+Cr5B3+CrB
80
20
(Cr,αFe)+Cr2B+Fe2B
(Cr,αFe)+(γFe)+Fe2B
Cr
20
40
(Cr,αFe)
60
80
(γFe)
Fe

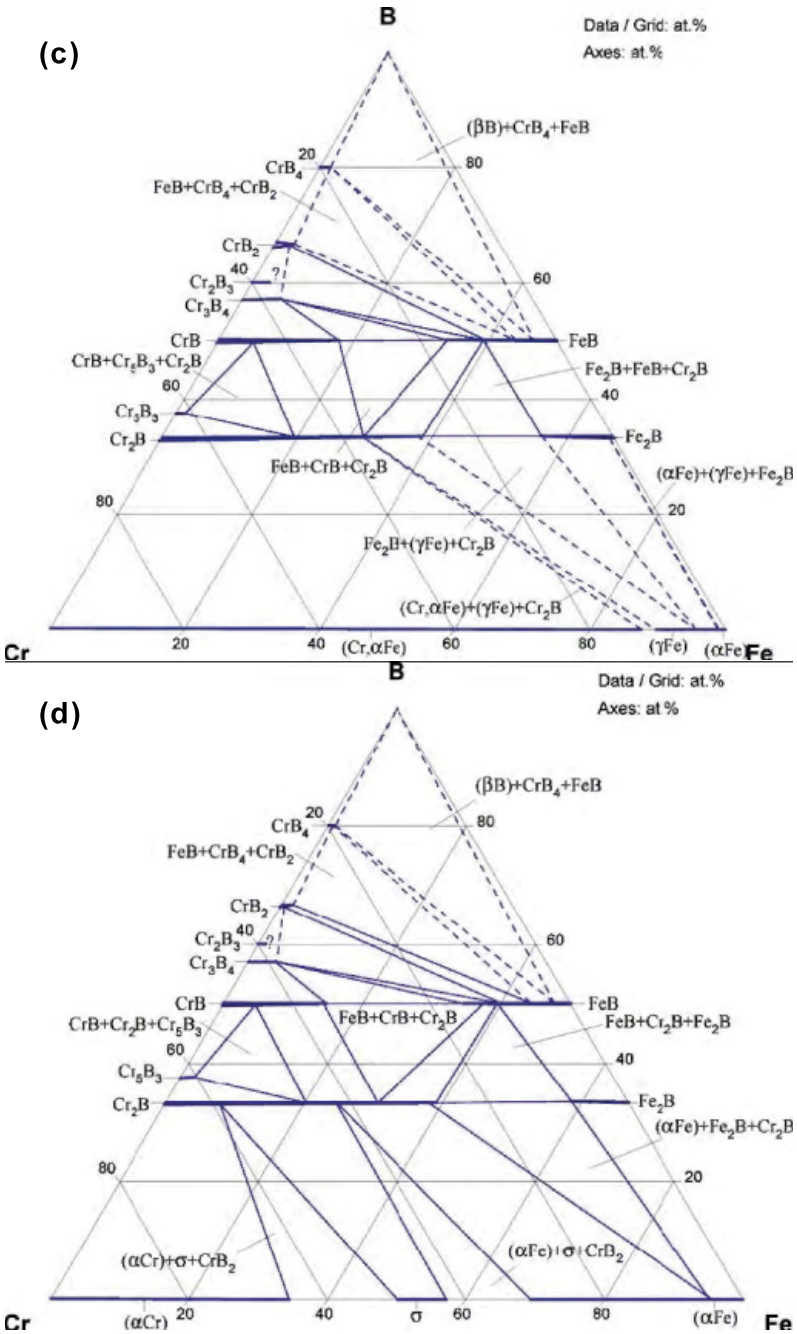

Figure 2.13: Ternary Fe–Cr–B isothermal phase diagrams at (a) 1250 ℃, (b) 1100 ℃, (c) 900 ℃ and (d) 700 ℃ [49]

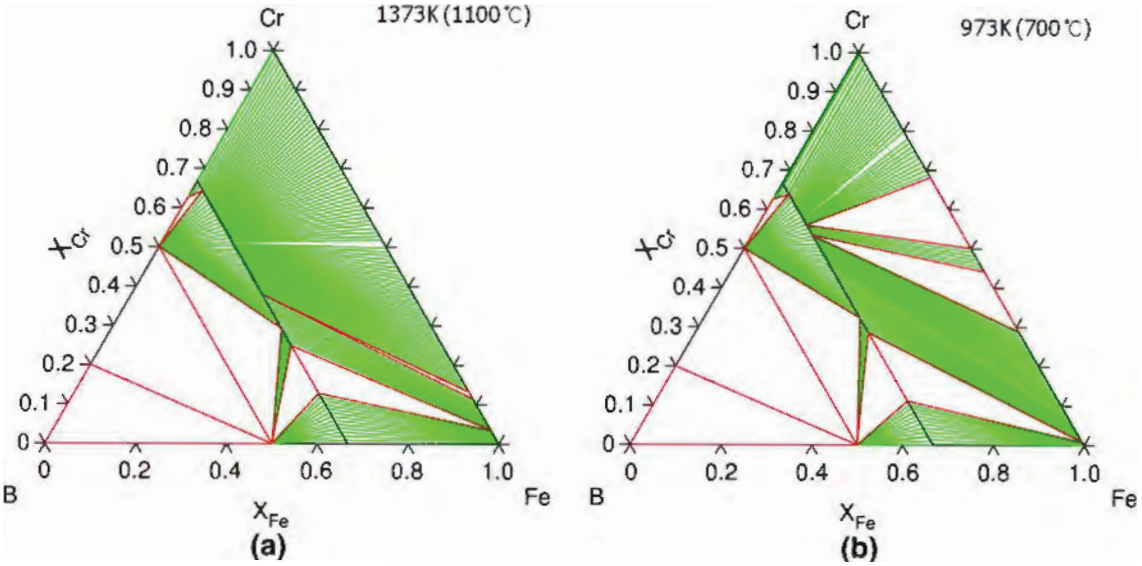

Figure 2.14: Ternary Fe–Cr–B isothermal phase diagrams at (a) 1100 ℃ and (b) 700 ℃ calculated by Thermo-Calc program based on the upgraded version of TCFE2000 database [12]. The compositions are in atomic fraction. The shaded areas represent the binary phases, while the unshaded areas represent the ternary phases.

Equilibrium Phases of Fe–Cr–B-Based Alloys

Table 2.4 presents the phases of the fabricated Fe–Cr–B-based alloys using various processes: high-energy electron beam irradiation (HEEBI), plasma transferred arc (PTA), powder-injection molding (PIM), detonation gun and high velocity oxygen fuel (HVOF). The phases and their structure were independent of the fabrication process but determined by the composition of the alloy. The fabricated alloys usually contained $(Cr,Fe)_2B$ and ferrite α-Fe-based containing alloying elements, such as Si, Mo and Mn. When the alloy contained Ni (Fe–Cr–B–Ni-based alloy), austenite γ-Fe-based became stable.

Table 2.4: The fabricated Fe–Cr–B-based alloys using various processes and the formed phases

Alloy composition (wt.%)	Process	Phases	Ref.
Fe–44Cr–5.6B–1.8Si–0.17C	HEEBI	$(Cr,Fe)_2B$ + α-Fe	[8]
Fe–45Cr–5.9B–2Si–0.17C	PTA	$(Cr,Fe)_2B$ + α-Fe	[9]
Fe–45Cr–5.9B–2Si–0.17C	PTA	$(Cr,Fe)_2B$ + α-Fe	[10]
Fe–43Cr–5.6B–1.8Si–0.17C	PIM	$(Cr,Fe)_2B$ + α-Fe	[11]
Fe–43Cr–5.6B–1.8Si–0.17C	PIM	$(Cr,Fe)_2B$ + α-Fe	[12]
Fe–25Cr–4B–4Mo–2Si	detonation gun	$(Cr,Fe)_2B$ + α-Fe	[13]
Fe–45Cr–5.9B–2Si–0.17C	HVOF	$(Cr,Fe)_2B$ + α-Fe	[9]
Fe–45Cr–5.9B–2Si–0.17C	HVOF	$(Cr,Fe)_2B$ + α-Fe + amorphous + Fe_2O_3	[14]
Fe–20Cr–3.6B–5.5Mo–6W–3.5Mn–1Si–0.4C	HVOF	$(Cr,Fe)_2B$ + α-Fe + amorphous	[22]
Fe–30Cr–17Ni–10Co–4Mo–4B–2.5Cu–1.5Si	PIM	$(Cr,Fe)_2B$ + γ-Fe	[11]
Fe–30Cr–17Ni–10Co–4Mo–4B–2.5Cu–1.5Si	PIM	$(Cr,Fe)_2B$ + γ-Fe	[15]
Fe–31Cr–12Ni–3.6B–0.6C	HVOF	$(Cr,Fe)_2B$ + γ-Fe	[21]
Fe–32Cr–8Ni–4.6B–0.6C	HVOF	$(Cr,Fe)_2B$ + γ-Fe	[21]

Guo and Kelly [45] casted a Fe–12Cr–1.4B–2Ni–1.1Mn–0.5Si–0.36C–0.4Cu alloy, which consisted of a martensitic matrix and orthorhombic M_2B containing a high level of Cr and a low level of Fe and B. When the as-cast alloy was tempered at 750 ℃, secondary boro-carbides — $M_7(C,B)_3$, $M_{23}(C,B)_6$ and $M_6(C,B)$ — were precipitated from the matrix grain. However, these precipitates disappeared at 1050 ℃. The composition of these precipitates was different from the original M_2B. They contained a higher level of Fe and a lower level of Cr. Do et al. [12] also showed that after 1200 ℃heat treatment for 30 min, fine carbides were precipitated in the ferrite matrix.

Other phases, namely amorphous and oxides, can also be stable. While Kim et al. [9] have not found amorphous and oxides phases for the alloy fabricated by HVOF, Dent et al. [14] has found some amorphous phase and Fe_2O_3 stringers. Chokethawai

et al. [22] also claimed 50 wt.% partially amorphous phase in the HVOF-sprayed coatings of Fe-20Cr-3.6B-5.5Mo-6W-3.5Mn-1Si-0.4C (wt.%) alloy. They found that crystallization of the amorphous phase started at about 640 ℃, below which the coatings were thermally stable. Below 750 ℃, only α-Fe and $Fe_{1.1}Cr_{0.9}B_{0.9}$ phases formed, but above 750 ℃ a fine scale precipitate of $M_{23}C_6$ formed as well. Branagan et al. [16] also reported amorphous coatings for the deposited Fe–8Cr–2Mo–17B–5C–1Si–4Al (at.%) alloy using HVOF and plasma spray. The complete amorphous coating formed because the critical cooling rate for metallic glass formation of this alloy was low (10^4 K/s) compared to the typical cooling rate of HVOF (10^9 K/s).

2.2.2 Microstructure

The effects of the composition and process parameters on the microstructure of the Fe–Cr–B-based alloys have been studied. Yoo et al. [57] studied the effect of B concentration in Fe–20Cr–1.7C–1Si–xB (x = 0–2 wt.%) alloy prepared by the arc-melting process. When the B content was lower than 2 wt.%, the alloy was hypoeutectic, with primary austenite dendrites interspaced by eutectic carbides and borides. When the B content exceeded 2 wt.%, the microstructure changed to hypereutectic and was composed of primary coarse borides in an interdendritic eutectic phase.

Jin et al. [13, 23, 24] studied the effect of fuel gas conditions on the microstructure of a Fe–24Cr–3B–9Ni–5Mo–2Si (wt.%) alloy deposited by the detonation gun thermal spray process. The coatings (Figure 2.15) were composed of $(Cr,Fe)_2B$ particles, an Fe-Cr solid solution splat matrix supersaturated with Si and B and $FeCr_2O_4$ spinel

oxide inclusions. The boride particles were highly faulted, though they did not explain the origin of this faults. The matrix was a BCC structure and consisted of two regions; micro-crystalline (0.1–0.5 µm grain size) and nano-crystalline (about 10 nm grain size). As the fuel gas content increased, the fraction of the oxide inclusions increased, but the unmelted particles and pores decreased.

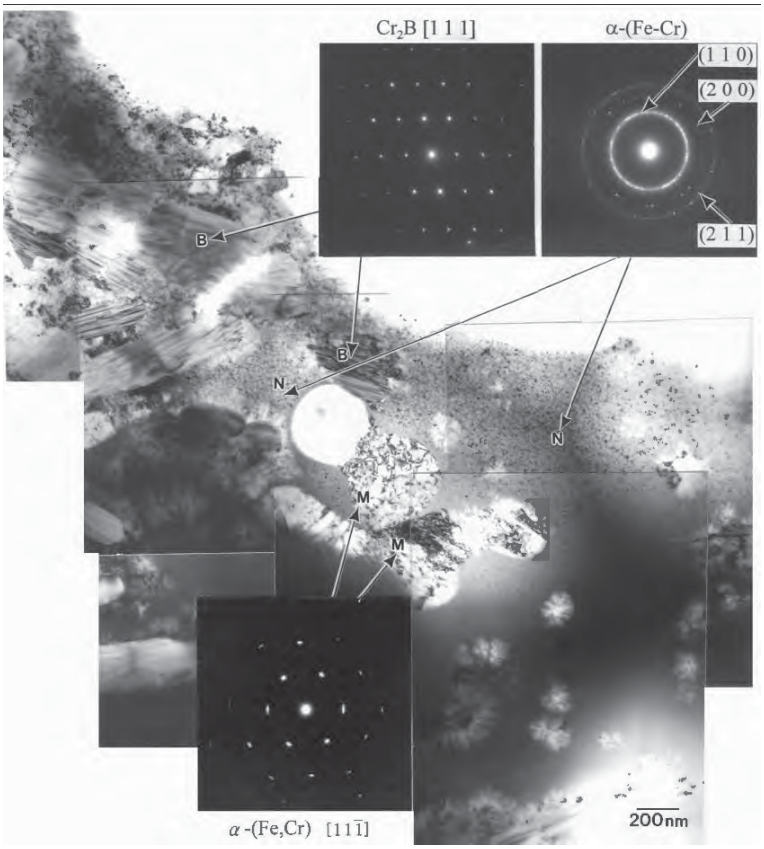

Figure 2.15: TEM micrograph for a Fe–24Cr–3B–9Ni–5Mo–2Si (wt.%) alloy (X28 specimen) as-sprayed using a detonation gun [23]

Jin et al. [25] investigated the effect of heat treatment on the structure of the matrix of a 56Fe–24Cr–3B–9Ni–5Mo–2Si (wt.%) alloy using an in-situ TEM heating experiment, as shown in Figure 2.16. The as-sprayed coating by detonation gun consisted of $(Cr,Fe)_2B$ and matrix composing of nano-crystalline α-(Fe,Cr) (<10 nm grain size). When the as-sprayed coating was annealed at 670 K, the nano-crystalline phase grew but maintained its size and density for a longer time, which indicated good thermal stability. At 800 K annealing, grain size and density of the matrix slightly increased; and, similarly, no effect on annealing time was observed. At 960 K, the crystallization process was completed, and coarsening of α-(Fe,Cr) was observed.

Manna et al. [58] studied the effect of mechanical attrition on the microstructural evolution of a gas-atomized Fe–50Cr–8B–3Si–0.17C and Fe–32Cr–4B–9Co–4Mo–2.4Cu–1.4Si–0.12C (wt.%) alloy powders. While the first alloy consisted of $(Cr,Fe)_2B$ and ferrite matrix, the second one consisted of $(Cr,Fe)_2B$ and austenite matrix. Low-intensity attrition nominally refined the grains of the ferrite in the first alloy and transformed the austenite phase in the second alloy into two fine grain phases (austenite and boride). High-intensity milling dissolved the boride phase in the fine-grained (40–50 nm) ferrite phase by 10 h and yielded a single-phase nanocrystanlline (20–25 nm) microstructure by 20 h of milling. After 30 h, the grain size was less than 15 nm. The region between nanocrystalline grains was amorphous.

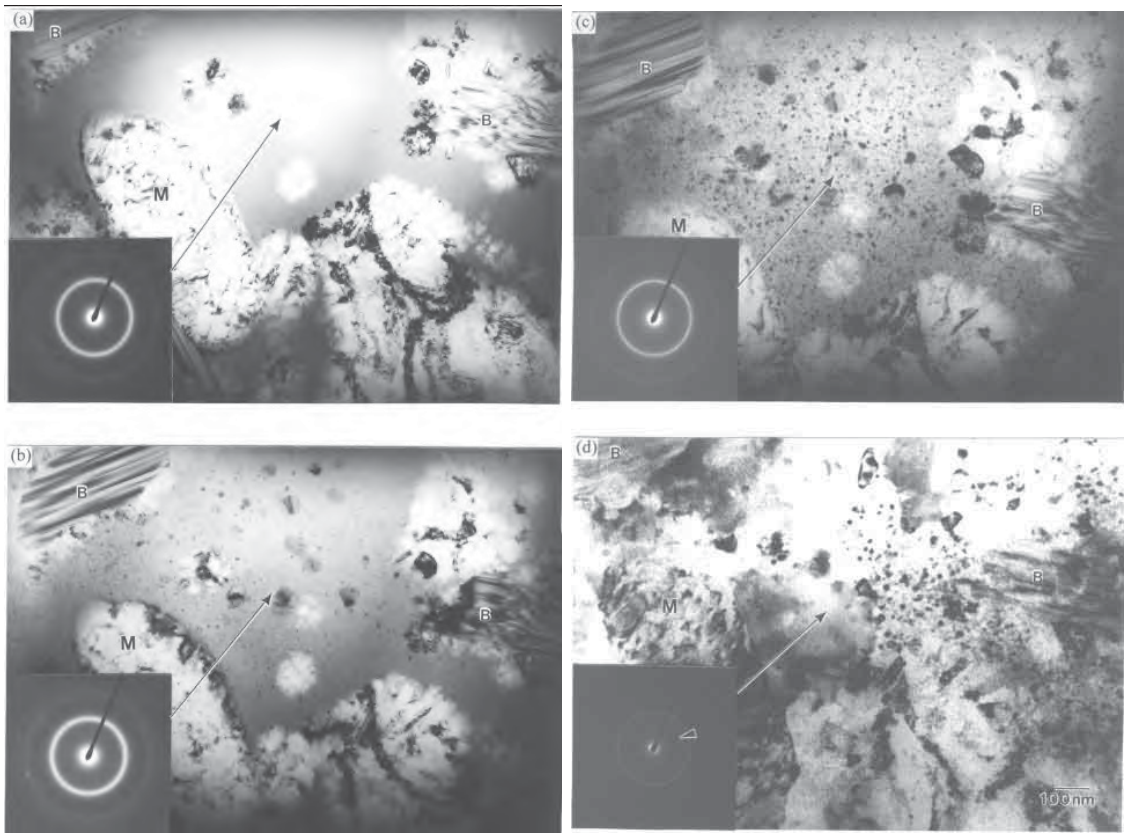

Figure 2.16: Sequential bright field TEM micrographs and corresponding selected area electron diffraction patterns (SADPs) from the matrix region obtained during the in-situ heating of Fe–24Cr–3B–9Ni–5Mo–2Si (wt.%) alloy: (a) as-sprayed specimen, (b) specimen annealed at 670 K for 30 min, (c) specimen annealed at 800 K for 20 min and (d) specimen annealed at 960 K for 20 min [25]

Morphology of $(Cr,Fe)_2B$

The size of $(Cr,Fe)_2B$ has been shown to vary from process to process. While HVOF produced small particles (Figure 2.17) [9, 14, 20], PTA produced a long and larger primary $(Cr,Fe)_2B$ phase (Figure 2.18) [10]. A small secondary $(Cr,Fe)_2B$ phase can also form with PTA (Figure 2.18a), depending on the composition. The HVOF process produced smaller particles because it yielded higher solidification rate.

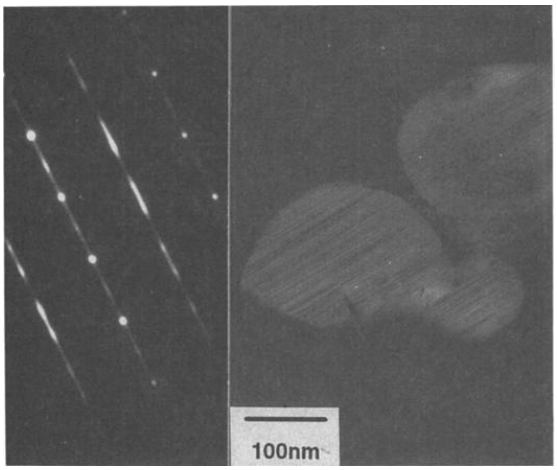

Figure 2.17: TEM image of $(Cr,Fe)_2B$ precipitates of the Fe–45Cr–5.9B–2Si–0.17C deposited by HVOF [14]

Table 2.5 presents the shape of $(Cr,Fe)_2B$ in the Fe–Cr–B-based alloys fabricated with different processes. The HVOF thermal spray process produced a spherical shape (Figure 2.17), while coating deposited by detonation gun thermal spray showed rod-shaped $(Cr,Fe)_2B$ particles (Figure 2.15).

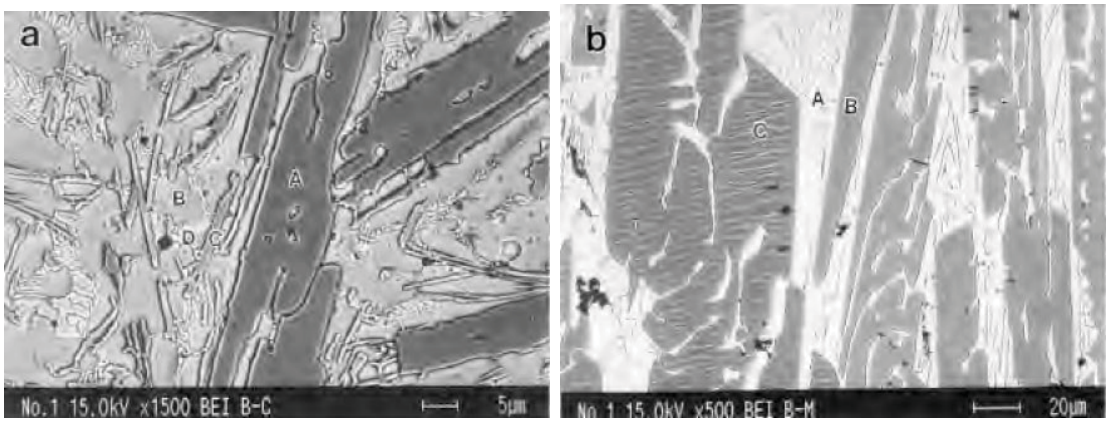

Figure 2.18: BSE micrographs of (a) Armacor C and (b) Armacor M coatings deposited by the PTA process [10]

Table 2.5: The shape of $(Cr,Fe)_2B$ in the Fe–Cr–B-based alloys fabricated using various processes

Alloy composition (wt.%)	Process	$(Cr,Fe)_2B$ shape	Ref.
Fe–45Cr–5.9B–2Si–0.17C	HVOF	sphere	[14]
Fe–24Cr–3B–9Ni–5Mo–2Si	detonation gun	rod	[23]
Fe–31Cr–4.1B–1.7Si–0.16C	casting	needle/rod	[12]
Fe–11Cr–1.4B–1.2Si–1.1Ni–0.9Mo–0.7V–0.6Cu–0.2Mn–0.2C	casting	plate	[59]
Fe–12Cr–3.5B–4Ni–3.3Mo–2Si–0.2Mn–2C–1.2Cu	SLPS	square	[29]
Fe–12Cr–3.5B–4Ni–3.3Mo–2Si–0.2Mn–2C–1.2Cu	HIP	lamellar	[29]

Do et al. [12] reported the shape of $(Cr,Fe)_2B$ particles for the as-cast alloy as needle/rod (Figure 2.19a). However, the shape seems to be plate-like. The shape changed to spherical/elliptical (Figure 2.19b) after a 30 min heat treatment at 1200 ℃. Guo and Kelly [59] showed that the $(Cr,Fe)_2B$ phase of the casted alloy were irregular plates (Figure 2.20), which were in contact with each other. When the alloy was heat treated, the thickness of the plates increased and the connection between them became more prominent.

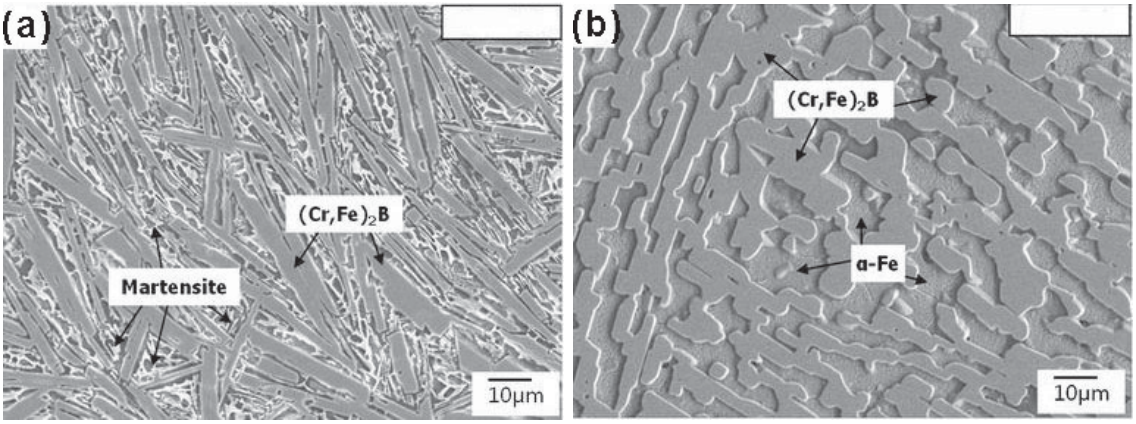

Figure 2.19: SEM micrographs of a Fe–31Cr–4.1B–1.7Si–0.16C alloy (a) as-casted and (b) heat-treated for 30 min at 1200 ℃ [12]

Rottger et al. [29] found that the shape of the hard M_2B phases in the Fe–12Cr–3.5B–4Ni–3.3Mo–2Si–0.2Mn–2C–1.2Cu (wt.%) alloy powder changed from process to process, as shown in Figure 2.21. They were squared for the SLPS process but lamellar shape for the HIP process because of a long sintering duration. In SLPS, the sintering occurred under vacuum at 1150 ℃ for 10 min; in HIP, the powder was pressed by 100 MPa, and the sintering occurred at 1000 ℃ for 2 h.

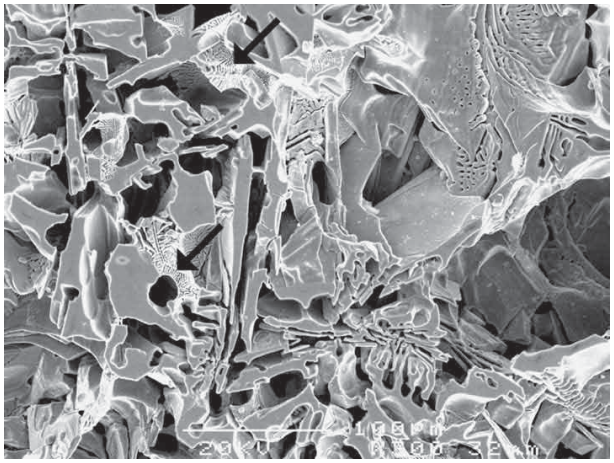

Figure 2.20: Morphology of the $(Cr,Fe)_2B$ phase in the Fe–11Cr–1.4B–1.2Si–1.1Ni–0.9Mo–0.7V–0.6Cu–0.2Mn–0.2C (wt.%) alloy [59]

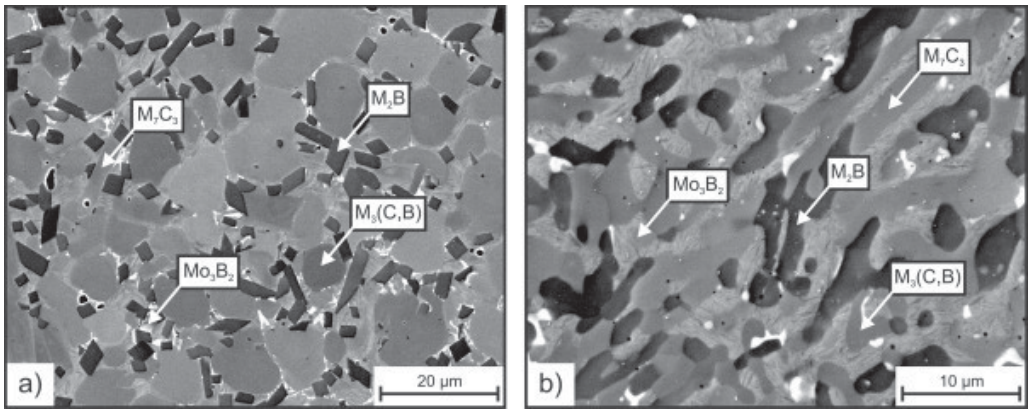

Figure 2.21: Microstructure of a Fe-12Cr-3.5B-4Ni-3.3Mo-2Si-0.2Mn-2C-1.2Cu (wt.%) alloy fabricated by (a) SLPS and (b) HIP [29]

Fraction of $(Cr,Fe)_2B$

It has been shown that the fraction of the $(Cr,Fe)_2B$ phase is mainly determined by the B content in the Fe–Cr–B-based alloys. Do et al. [12, 27] found that as the content of B increased, the fraction of equilibrium $(Cr,Fe)_2B$ increased. The calculated volume fraction of $(Cr,Fe)_2B$ by thermodynamic (Thermo-calc software and TCFE2000 database) matched the measured one.

The process parameters could also affect the fraction of $(Cr,Fe)_2B$. Jin et al. [13, 23, 24] deposited a Fe–24Cr–3B–9Ni–5Mo–2Si (wt.%) alloy onto carbon steel using the detonation gun thermal spray process with various fuel gas conditions. As the fuel gas content increased the fraction of the boride particles decreased as a result of boride thermal dissolution increasing during the spraying. Kim et al. [15] found that as the sintering temperature increased, the $(Cr,Fe)_2B$ fraction increased for the Fe–30Cr–17Ni–10Co–4Mo–4B–2.5Cu–1.5Si (wt.%) alloy during the PIM process.

2.2.3 Hardness

In section 2.2.2, it was shown that the composition and process parameters can affect the microstructure of Fe–Cr–B-based alloys. In this section, the parameters that determine hardness are addressed.

Table 2.6 presents the bulk hardness of the Fe–Cr–B-based alloys fabricated using various processes. The hardness has varied from 319 to 1,200 HV because of the $(Cr,Fe)_2B$ fraction variation, which depends on the B content and process parameters. Hardness increases as the $(Cr,Fe)_2B$ fraction increases (Figure 2.22) [11, 12, 27, 30]. However, the matrix hardness did not change as the B content increases [26].

Table 2.6: The hardness of the Fe–Cr–B-based alloy composites fabricated using various processes

Alloy composition (wt.%)	Process	Indentation load (g)	Hardness (HV)	Ref.
Fe–44Cr–5.6B–1.8Si–0.17C	HEEBI	300	541 ± 21	[8]
Fe–45Cr–5.9B–2Si–0.17C	PTA	500	925–1065	[9]
Fe–45Cr–5.9B–2Si–0.17C	PTA	5,000	699–864	[10]
Fe–43Cr–5.6B–1.8Si–0.17C	PIM	300	$1,059 \pm 30$	[11]
Fe–45Cr–5.9B–2Si–0.17C	HVOF	500	914–1110	[9]
Fe–42Cr–6B–2Si	HVOF	200	662–1016	[14]
Fe–43Cr–5.6B–1.8Si–0.17C	casing	300	760 ± 33	[12]
Fe–27Cr–5.6B–1.8Si–0.17C	casing	300	$1,200 \pm 8$	[12]
Fe–31Cr–4B–1.7Si–0.15C	casing	300	735 ± 14	[12]
Fe–30Cr–17Ni–10Co–4Mo–4B–2.5Cu–1.5Si	PIM	300	319 ± 20	[11]
Fe–30Cr–17Ni–10Co–4Mo–4B–2.5Cu–1.5Si	PTA	5,000	501–650	[10]
Fe–12Cr–3.5B–4Ni–3Mo–2Si–0.2Mn–2C–1Cu	SLPS	30,000	949 ± 3	[29]
Fe–12Cr–3.5B–4Ni–3Mo–2Si–0.2Mn–2C–1Cu	HIP	30,000	870 ± 5	[29]

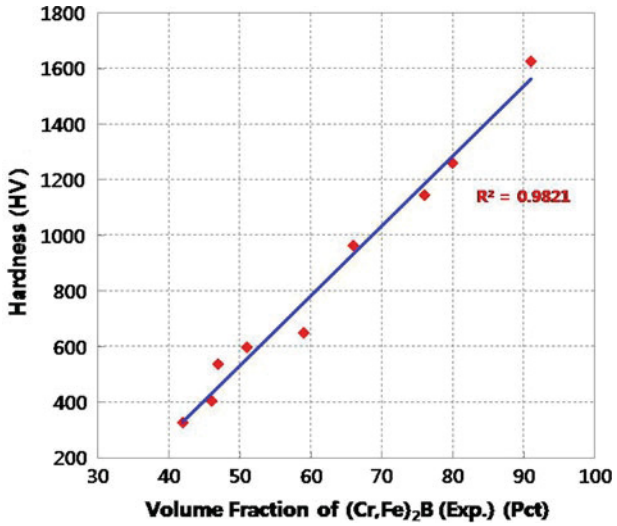

Figure 2.22: Hardness of the Fe–Cr–B-based alloys vs. the measured volume fraction of $(Cr,Fe)_2B$ [12]

In addition to the alloy's composition effect, the hardness values have varied from process to process as a result of the microstructural variation. As shown in Table 2.6, the hardness of Fe–45Cr–5.9B–2Si–0.17C (wt.%) (Armacor M) alloy varies from 541 to 1,110 HV. For the same alloy's composition and fabrication process, the measured hardness decreased as the indentation load increased. Rottger et al. [29] found that the hardness of the sintered alloy changed between SLPS and HIP (Table 2.6) even though they were heat treated with same conditions. As the sintering temperature of the SLPS process increases, the hardness increases. Sercombe and Schaffer [28] showed similar behavior for the sintered Fe–16Cr–2.2Ni–2B–0.8Si–0.8Mn–0.5Mo–0.2C (wt.%) alloy by the metal injection molding process. As a result of higher sintering temperature, the density and hardness increased (Figure 2.23). While they claimed that the hardness decreased when the specimen was sintered above 1,170 ℃ as a result of the boride coarsening, the hardness based on the error bars was similar.

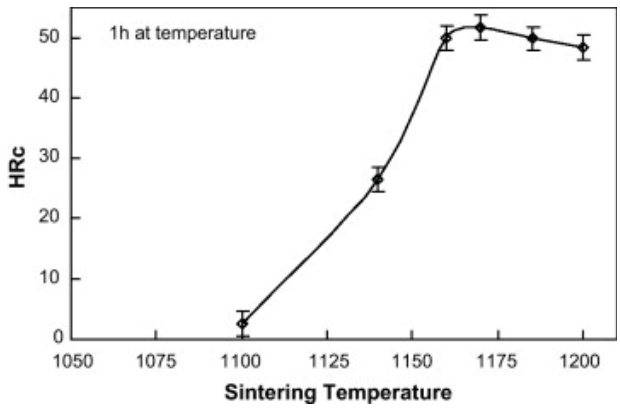

Figure 2.23: The effect of sintering temperature on the hardness of the Fe–16Cr–2.2Ni–2B–0.8Si–0.8Mn–0.5Mo–0.2C alloy processed by the metal injection molding process [28]

Other researchers also addressed the effect of heat treatment on the hardness of Fe–Cr–B-based alloys and found that heat treatment could increases or decreases hardness. Kim et al. [9] found that the hardness of the Fe–21Cr–6.5Ni–3.3Mo-3B–2.4Cu–1.8Si–1Mn–0.2C (wt.%) (Armacor 16) fabricated by the HVOF process was decreased after heat treatment for 1 h, because of phase transformation from the α (ferrite) to the γ (austenite) phase. This transformation did not occur in the heat-treated HVOF Armacor M alloy, though its hardness decreased. On the other hand, Branagan et al. [16] showed that the hardness of the as-sprayed plasma-sprayed Fe–8Cr–2Mo–17B–5C–1Si–4Al (at.%) alloy was increased from 10.7 ± 0.32 GPa to 12.8 ± 0.76 GPa after heat treatment at 800 ℃ for 1 h. The hardness of the as-deposited HVOF sample was increased from 10.2 ± 0.85 GPa to 11.4 ± 0.98 GPa after a 750 ℃ heat treatment for 1 h. Chokethawai et al. [22] measured the hardness of as HVOF-sprayed coatings of an Fe-20Cr-3.6B-5.5Mo-6W-3.5Mn-1Si-0.4C (wt.%) alloy as 9.2 GPa. When the alloy was heat treated above 550 ℃, the hardness increased. It increased significantly at 650 ℃ and 750 ℃, but slightly at 950 ℃.

Jin et al. [13, 23, 24] found that as the fuel gas content of detonation gun increased, the hardness of the Fe–24Cr–3B–9Ni–5Mo–2Si (wt.%) alloy coating increased though the fraction of the boride particles decreased. The hardness increased because the porosity decreased.

2.3 Tribology

Tribology is the science and technology of contacting surfaces in relative motion [5]. Tribology encompasses studies of all types of friction and wear. While the term "tribology" is relatively new, it is a phenomenon as old as the human race. In 3500 BC, wheels were already being used to reduce friction in translational motion of large blocks and stones because rolling friction is much less than sliding friction (dragging) [2].

Friction and wear are present in almost all systems that involve moving parts, and they can be preferred or unwanted [2]. Preferred friction is required in brakes, clutches, driving wheels and walking. Preferred wear is necessary in writing with a pencil, polishing, shaving and machining. Examples of undesirable friction and wear are in gears, bearings and cutting tools. Friction and wear are not material properties but a system response [2]. The purpose of research in tribology is to understand tribological behavior and principles to minimize the losses, which can lead to better efficiency, better performance, fewer breakdowns and significant savings.

Contact mechanics play a major role in understanding the behavior and performance of tribology. When two flat solid surfaces come into contact, the real area of contact is much smaller than the apparent area of contact [60], as demonstrated in Figure 2.24. The ratio of real-to-apparent area of contact can be as low as 10^{-4} and depends on surface irregularities, applied load and the yield stress of the softer material [60]. The real area during sliding is larger than that in the static state [60].

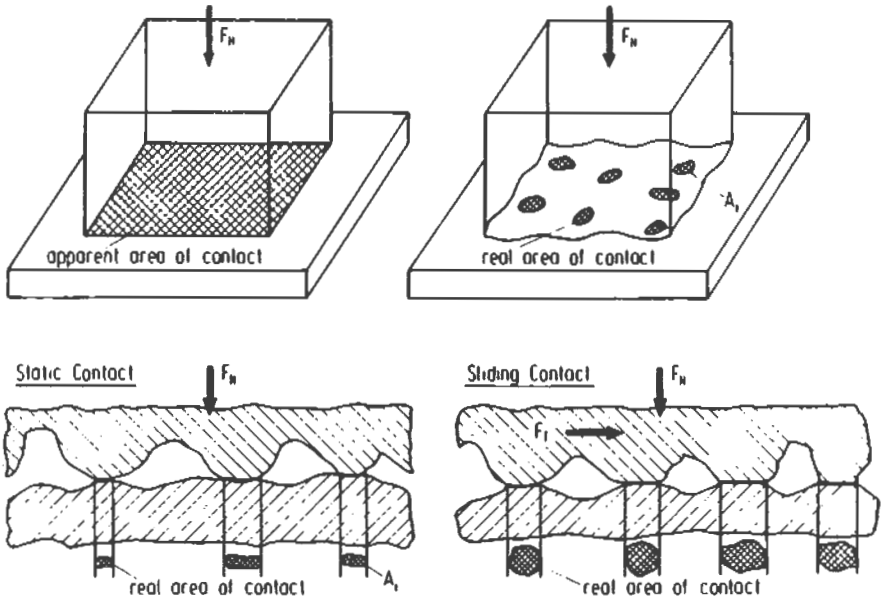

Figure 2.24: Apparent vs. real area of contact [60]

Friction

Friction is the resistance to movement of one body over another in contact during sliding [60, 61]. The law of friction was first introduced by Leonardo de Vinci (1452–1519) and rediscovered by Amontons (1663–1705) in 1699 [2]. The resistive force, in the opposite direction of motion, is called the friction force. The relation between this friction force (F) and the normal load (W) is known as the first law of friction, which was developed by Amontons as follows [2]:

$$F = \mu W \tag{2.11}$$

where μ is the coefficient of friction (COF). The friction force is linearly proportional to the applied load. The second law of friction states that the friction force (or

the COF) is independent of the apparent area of contact between the contacting bodies [2]. In addition to these two laws, Coulomb added a third rule that states that the friction force (or the COF) is independent of velocity [2]. However, the COF depends upon the mating materials, surface preparation and operating conditions (i.e. temperature, humidity, etc.) [2]. Typical values of the COF during unlubricated sliding for metals, alloys and ceramics are presented in Table 2.7.

Table 2.7: Typical values of the COF for metals, alloys and ceramics sliding on itself [2]

Material	COF
Al	0.8–1.2
Cr	0.5–0.6
Cu	0.8–1.2
Fe	0.8–1.5
Cast iron	0.8–1.0
Mild steel	0.7–0.8
Ni-based alloys	0.6–0.9
Al_2O_3	0.3–0.6
WC	0.3–0.7
Diamond	0.1–0.2

Wear

Wear is the surface damage or removal of material from solid surfaces in contact during relative motion [2, 62]. Wear usually occurs through surface interaction at asperities [2]. A material from the contacting surface may be initially deformed and then removed as a result of material transfer, or break loose as wear particles (debris).

The most common wear mechanisms (Figure 2.25) are adhesive, abrasive, fatigue and chemical (or corrosive) [2, 60, 62]. One or more of these wear mechanisms may occur at the same time in one particular tribological system [62].

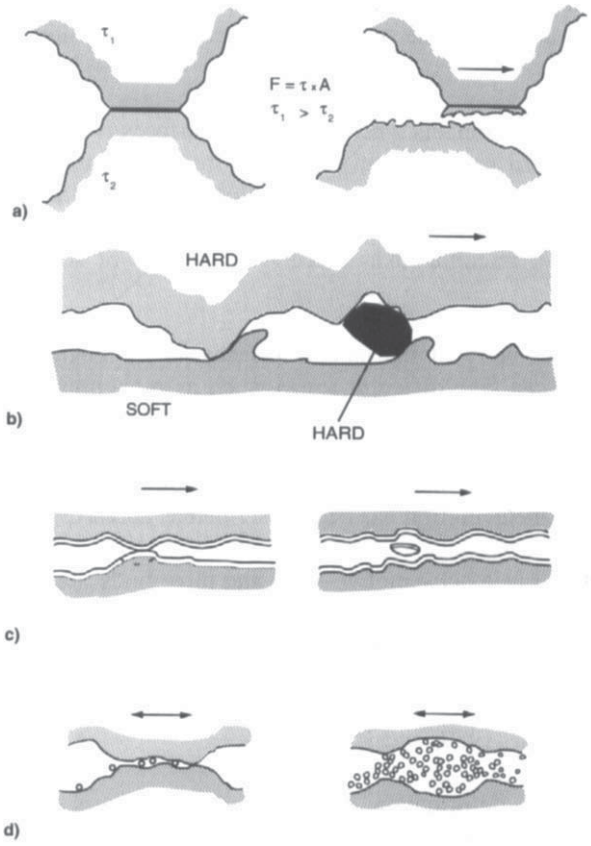

Figure 2.25: Schematic of basic wear mechanisms: (a) adhesive, (b) abrasive, (c) fatigue and (d) chemical [62]

Adhesive wear occurs when asperities of two surfaces come into contact and adhere to each other, forming asperity junctions (Figure 2.25a). The sliding motion of the surfaces causes deformation and/or material detachment [62].

Abrasive wear occurs when asperities of a rough-hard surface or hard particles penetrate and slide on a softer surface (Figure 2.25b), abrading or damaging the surface by plastic deformation or fracture [2, 63]. Abrasive wear processes are divided traditionally into two-body and three-body abrasion. In two-body abrasion, the hard surface or particles is part of one of the surfaces. In three-body abrasion, the hard surface is a third body caught between the two other surfaces. Common abrasive wear modes resulting from plastic deformation are cutting, ploughing and wedge-forming [7], as shown in Figure 2.26. In addition to these modes, the microcracking mode occurs with brittle materials.

Fatigue wear (delamination) occurs when repeated loading and unloading cycles are exposed to the materials and induce the formation of subsurface/surface cracks or wear debris (Figure 2.25c). After a critical number of cycles, these cracks will result in the breakup of the surface, leaving large pits in the surface. This effect is also known as pitting [2]. Chemical or corrosive wear occurs when sliding takes place in a corrosive environment [2]. Oxidation is the most common type of corrosive wear. A thin layer of oxides forms on metal surfaces. This layer is continuously removed, and new layers form again.

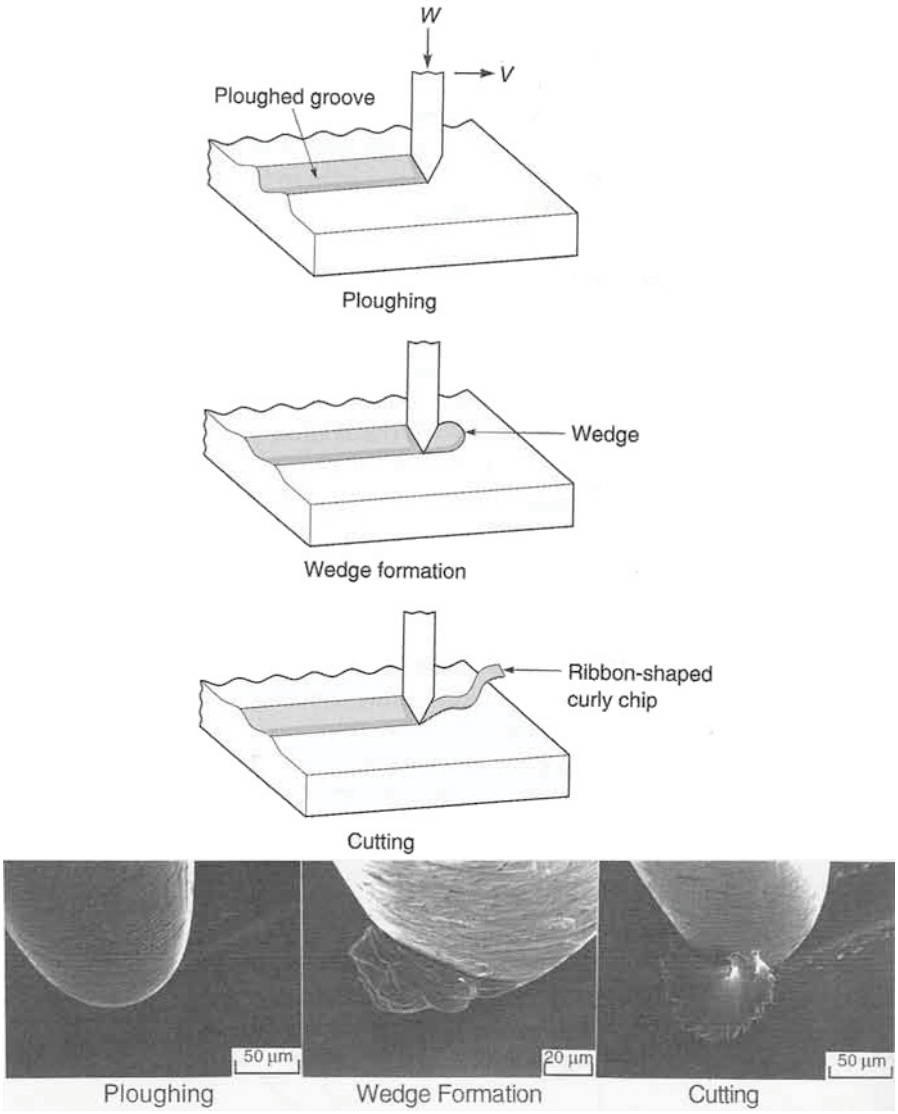

Figure 2.26: Schematic of abrasive wear modes [7]

Wear resistance and performance are typically quantified by wear rate, the volume or mass of material removed per unit of time or sliding distance. While the most common method to calculate wear rate is by measuring the weight loss after a tribology test, the wear volume can be directly determined using surface topography techniques, such as a profilometer. Wear rate is most commonly expressed in terms of the Holm wear relationship (Holm, 1946; Archard, 1953) [62]

$$Wear\ rate = \frac{K}{H} = \frac{V}{L \times d} \tag{2.12}$$

where V is the wear volume, d is the sliding distance, L is the normal load, K is a material constant known as the wear coefficient and H is the hardness. Like the COF, the material constant (K) is dependent upon the mating materials, surface preparation and operating conditions [2]. The wear rate of materials is typically presented in terms of mm^3/Nm, or the nondimensional wear coefficient (k). The wear resistance is the inverse of the wear rate [64]:

$$Wear\ resistance = \frac{1}{Wear\ rate} \tag{2.13}$$

2.3.1 Tribology of MMC

Materials for engineering applications are selected based on the required strength, toughness and size of the part. For tribology applications, if these materials do not have high wear resistance, coatings are applied to increase surface hardness or introduce lower friction. However, third bodies are created during wearing, and friction and wear rate evolve with time. Therefore, selecting the proper materials and

coatings to control friction and wear through a life time is important. Metal matrix composites (MMCs) have been shown to exhibited high hardness, toughness and wear resistance. Their wear resistance depends on different microstructural parameters, such as the hardness, shape, size, volume fraction and distribution of the embedded reinforcement, the properties of the matrix and the interfacial bonding between the reinforcement and the matrix [7].

Axen and Jacobson [64] developed a model to estimate the abrasive wear resistance of two-phase materials based on the rule of mixture. The model defines two modes of abrasive wear for two-phase materials, namely, equal wear rates of phases (EW) and equal pressure on phases (EP). In the EW mode, both phases are worn at the same linear rate. The EW mode corresponds to the upper limit of wear resistance (ideal state). The specific wear resistance ($\Omega = 1/(\text{specific wear rate})$) under the EW condition can be estimated by

$$\Omega = \frac{A_P}{A}\Omega_P + \frac{A_m}{A}\Omega_m \tag{2.14}$$

where Ω_P is the specific wear resistance of the particle, Ω_m is the specific wear resistance of the matrix, A_p/A is the fraction of the particle phase, and A_m/A is the fraction of the matrix. In the EP mode, the matrix is worn individually while the reinforcing phase is removed discretely. Thus, the reinforcing phase contributes slightly to wear resistance. The EP mode corresponds to the lower limit of wear resistance. The specific wear resistance under the EP condition can be estimated by

$$\Omega = \left(\frac{A_P}{A\Omega_P} + \frac{A_m}{A\Omega_m}\right)^{-1} \tag{2.15}$$

Equations 2.14 and 2.15 can typically be plotted as shown in Figure 2.27. The wear resistance of composite materials should fall somewhere between these limits, depending on the reinforcing particles' size and fraction, matrix hardness, abrasive grit size and inter-phase bonding.

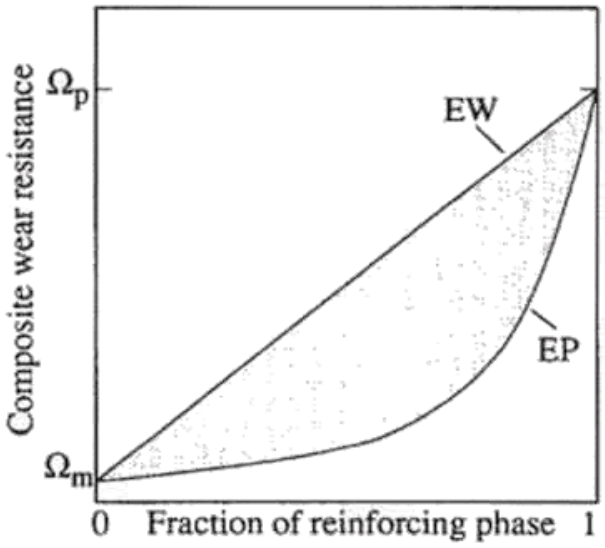

Figure 2.27: Schematic representation of composite wear resistance as a function of the reinforcing phase fraction as calculated by Equation 2.14 (EW) and Equation 2.15 (EP) [64]

This model was validated by tested Al reinforced with 20 µm SiC particles using a two-body abrasion test [64]. The authors concluded that to maximize the wear performance, EW should dominate. This can be achieved by large enforcing particles, small abrasive grit, low load and high wear resistance of the matrix.

Zum Gahr [7] has also reported the validation of the use of rules of mixtures to estimate wear resistance of multiphase materials if the reinforcing constituents are strongly fixed in the matrix and are not pulled out by abrasives. Moreover, wear resistance of two-phase materials was experimentally measured between the boundaries given by both rules of mixtures, as shown in Figure 2.28 [7]. Wear resistance of type B material (elongated reinforcement) increases significantly with the volume fraction of the reinforcing particles. In contrast, wear resistance of type A material is substantially increased only with large volume fractions of the reinforcing phase. The effect of the reinforcing phase depends on its material, size and distribution as well as on size and material of abrasive particles [7].

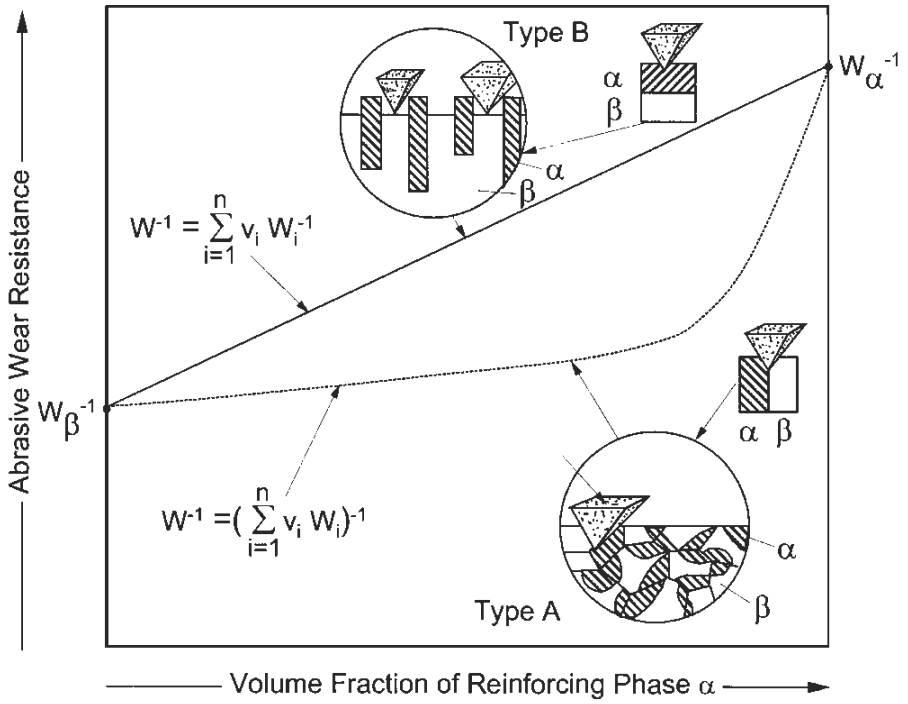

Figure 2.28: Abrasive wear resistance of two-phase materials as a function of the volume fraction of a reinforcing phase [7]

2.3.2 Tribology of Fe-Cr-B Alloys

Wear Performance

The abrasive and sliding wear performance of Fe–Cr–B-based alloys has been investigated. Dent et al. [14] performed dry rubber three-body abrasive wear tests for the Fe–45Cr–5.9B–2Si (wt.%) (Armacor M) and 25Fe–Cr–28Ni–4.3B–3.2Cu–4.4Mo–2.2Si (wt.%) (Armacor C) alloys deposited by the HVOF process. The alloys showed good abrasive wear resistance compared to other HVOF-sprayed alloys (Figure 2.29), and Armacor M had better resistance than Armacor C.

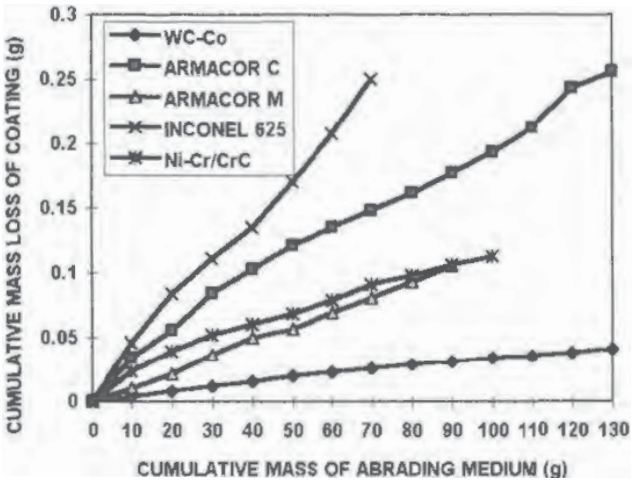

Figure 2.29: Abrasive wear data for the Fe–45Cr–5.9B–2Si (wt.%) (Armacor M) and 25Fe–Cr–28Ni–4.3B–3.2Cu–4.4Mo–2.2Si (Armacor C) alloys compared with other metallic alloys [14]

Kim et al. [9, 20] performed two-body abrasive and pin-on-disk sliding wear tests for Fe–45Cr–5.9B–2Si–0.1C (wt.%) (Armacor M) and Fe–21Cr–6.5Ni–3Mo–3B–2.4Cu–1.8Si–1Mn (wt.%) (Armacor 16) gas atomized powders deposited using the HVOF process. They [10] also welded Fe–44.5Cr–5.9B–2Si–0.2S (wt.%) (Armacor M) and Fe–

31Cr–18Ni–4Mo–4B–2.6Cu–1.4Si–10Co (wt.%) (Armacor C) using the PTA process. Armacor 16 exhibited the lowest wear resistance because it had the lowest hardness (627 HV) and the highest porosity. The PTA Armacor M showed better abrasive and sliding wear resistance than the HVOF Armacor M. This wear improvement was not due the hardness since they both had same hardness (992 HV), but because of the size and orientation of its boride phases. The sliding wear resistance of the different coatings followed a similar trend with the abrasive wear resistance. Armacor M showed better wear performance than Armacor C for all wear testings because of higher hardness and larger boride particles.

Son et al. [11] performed an abrasive wear test of an Fe–43Cr–5.6B–1.8Si–0.17C (wt.%) alloy (Armacor M) fabricated using the PIM process. The abrasive wear resistance of Armacor M was 3 times greater than the SS316L stainless steel. The wear resistance increased as the bulk hardness increased because of the increase of $(Cr,Fe)_2B$ fraction. Lee et al. [8] fabricated an Fe–43Cr–5.6B–1.8Si–0.17C (wt.%) (Armacor M) surface composite using the HEEBI process. The wear resistance was 77% higher than that of the plain carbon steel. Venugopal and Agrawal [18] found that the thermally sprayed an Fe–29Cr–3.75B–1.6Si–1.65Mn (wt.%) alloy cored wire using the twin wire arc thermal spray (TWAS) process showed good erosion resistance against solid particle impingement.

Other researchers have also studied the effect of microstrcture of Fe–Cr–B-based alloys on the wear performance. They have got same conclusion and found that as the fraction and size of $(Cr,Fe)_2B$ increased, the hardness and wear resistance improved [8,10]. The larger $(Cr,Fe)_2B$ particles counteracted more effectively chipping

and ploughing by the abrasives [29]. Moreover, the shape, orientation and distribution of the $(Cr,Fe)_2B$ phase can affect the wear resistance [9, 20, 26].

Wear Behavior

Many studies has investigated the wear behavior of the Fe–Cr–B-based alloys fabricated using various processes. The wear behavior and mechanisms were independent of the alloy's composition and fabrication process, which determine the microstructure. In sliding wear, the reported main wear mechanisms were delamination [10, 21] and tribo-oxidation [21].

During abrasive wear, the matrix was selectively removed more than the $(Cr,Fe)_2B$ phase, because it had lower hardness [10, 17]. Therefore, the load was supported by $(Cr,Fe)_2B$, which was cracked and pulled out. The reported wear mechanisms for two-body abrasive wear were microcutting [8, 29, 65] and microploughing [10, 29]. Softer alloys showed more severe scratches with wedge formation [10].

Metamorphic transformation

Scruggs [66] patented a composition of specific ternary alloys to protect the surface from wear by transforming the outer surface into an amorphous phase during wearing and to improve the wear performance. The coating was deposited as a crystalline phase. With wearing, its matrix was transformed into an amorphous phase (metamorphic transformation). Such metamorphic alloys essentially consist from 40–75 wt.% of the group of Fe, Co or Fe-Co; >20 wt.% of the group of Cr, Mo, W, Nb, V, Ti or a combination; and 2–6 wt.% of the group of B, C or B-C. They found the most

preferable transformable material was the 59Fe–36Cr–5B (wt.%) alloy.

Scruggs [19] fabricated a Fe–28Cr–3.7B (wt.%) alloy by TWAS and a Fe–32Cr–4B–28Ni–4Mo (wt.%) alloy by HVOF. As a result of abrasive and adhesive wear, the matrix phase at the wear surface transformed into an amorphous and fine nanocrystals. The transformed surface exhibited low COF (0.12–0.14) for alumina pin-on-disk wear tests. It was found that as the coating density increased, the wear performance improved.

Jin et al. [13, 23, 24] performed a ring-on-disc sliding wear test for a Fe–24Cr–3B–9Ni–5Mo–2Si (wt.%) alloy deposited by the detonation gun thermal spray process. After wearing, the crystalline phase of the matrix on the surface layer (Figure 2.15) transformed into the amorphous phase, as shown in Figure 2.30. However, the boride particles still remained in the crystalline state. As the fuel gas increased, the hardness increasing and porosity reduction, and thus the wear resistance was increased. However, the highest fuel gas content caused the oxide formation of Si and B that stabilized the crystalline phase, and resulted in a lower wear resistance because the absent of the amorphous layer formation. With 0.5 m/s and 4 kg load, the coating exhibited low COF (0.05–0.2), which is about $1/20^{\text{th}}$ of the COF usually obtained for most metallic alloys. As the amorphous phase formation reduced, the COF increased. The improvement in wear resistance was due to this low COF and the high hardness value that result from metamorphic transformation. Similar results were found after the grinding process.

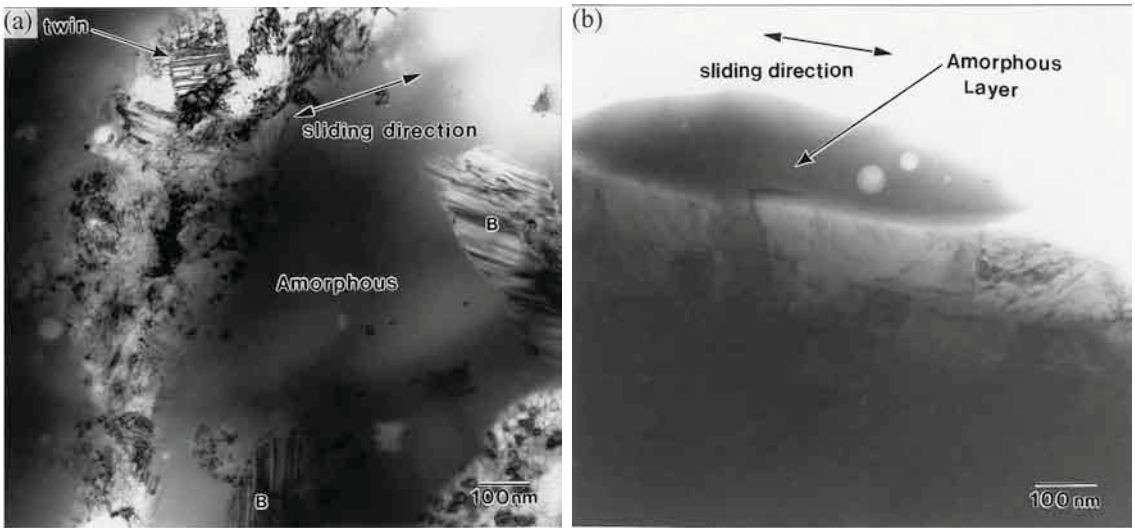

Figure 2.30: TEM micrographs after wear for a Fe–24Cr–3B–9Ni–5Mo–2Si (wt.%) alloy sprayed detonation gun [23]

Jin et al. [13, 23] found that this metamorphic transformation behavior during wear was similar to the solid state amorphization reaction (SSAR) [67], which occurs in the mechanical alloying of powders. They calculated, using the Egami criterion [68], the minimum required B content in the matrix to stabilize the amorphous phase during sliding, and it was found to be 10 at.%. Auger analysis showed that the matrix of the starting powder did not contain B, but the matrix of the deposition contained about 7 at.% B. They claim that the supersaturation of the matrix with B resulted from the rapid solidification upon the impact of the droplet on the substrate.

Kim et al. [9, 20] also found this crystalline-amorphous transformation on the uppermost layer after two-body abrasive and pin-on-disk sliding wear tests for the Fe–44.5Cr–5.9B–2Si and Fe–21Cr–6.5Ni–3Mo–3B–2.4Cu–1.8Si–1Mn (wt.%) alloys deposited by HVOF. They claimed that the wear resistance of these alloys depended more on density and microstructure than on the amorphous layer formation.

CHAPTER 3

Aim of The Research

3.1 Objective

As shown in the literature, the Fe–Cr–B-based alloys have been fabricated using various thermal spray, welding and sintering processes. Their microstructure and tribological performance vary from process to process. The welding processes have produced better depositions than thermal spray because of the absence of oxide phases, pores and unmelted particles as well as the higher coating adhesion, quality and wear resistance compared to that produced by thermal processes.

One of the recently developed welding processes—controlled short-circuit metal inert gas (CSC-MIG)—has not been used to fabricate these alloys. As CSC-MIG has been shown to offer a higher transfer rate, lower heat input and higher welding stability than the conventional MIG process, it was selected to fabricate this alloy in the present research. Moreover, the powder of these alloys has not been fully consolidated with solid-state mechanism by the conventional sintering processes. As the assistance of current in the spark plasma sintering (SPS) process has been shown to offer improved properties and full consolidation of difficult-to-sinter-powders for

shorter holding time compared to other methods, SPS was selected to consolidate the powder of this alloy.

Therefore, the primary focus of this research was to understand the microstructure and tribology of an Fe–28Cr–3.8B–1.5Si–1.5Mn (wt.%) alloy welded using CSC-MIG and an Fe–45Cr–5.9B–2Si–0.1C (wt.%) alloy powder sintered by SPS. This understanding can help to establish the relationship between process parameters, microstructure, hardness and wear performance for this MMC. This can help other researchers in understanding how to reduce wear of MMCs and to select the appropriate process and composition for a specific application. The specific objectives were:

- To understand the solidification behavior of these alloys using thermodynamic modeling;
- To develop a model that describes the densification of the powder during SPS;
- To investigate the effect of process parameters on the microstructure, which involves the phases and their morphology identification as well as their fraction measurement;
- To measure the hardness of the phases as well as bulk hardness of the fabricated alloys, and to correlate them with the microstructure;
- To evaluate and study the tribological performance and behavior of the fabricated alloys and to correlate them with their microstructure and hardness.

3.2 Research Approach and Methodology

Figure 3.1 highlights the overall methodology of the current research. The starting materials used in this research were a cored wire and a gas-atomized powder of the Fe–Cr–B-based alloy. Their chemical compositions are presented in Table 3.1. The wire was welded onto a 1020 carbon steel substrate using the CSC-MIG process. The powder was consolidated using the SPS process to form a bulk specimen.

The solidification behavior of the starting gas-atomized powder and the welded wire was studied by numerical thermodynamic calculation based on the Scheil-Gulliver model. The melting and transformational temperatures of the starting powder and the weldment were measured using a differential scanning calorimeter (DSC). Densification of the powder during the SPS process was modeled. The microstructure characterization, hardness measurements and tribology testings were performed for the alloys welded by CSC-MIG and sintered by SPS.

The volume fractions and chemical compositions of the phases were calculated by the thermodynamic analysis. The phases were experimentally identified using X-ray diffraction (XRD). Macrostructure analysis of the weldment was performed using light microscopy. The morphology and microstructure of the phases were investigated by scanning electron microscopy (SEM). Qualitative elemental analysis was carried out using energy dispersive spectroscopy (EDS). The volume fraction and aspect ratio of the phases were measured using image analysis. The hardness of the individual phases was measured by nanoindentation, and the bulk specimens' hardness was measured with Vicker microhardness.

Two-body abrasive wear testing was performed to evaluate wear resistance and to understand wear behavior. In addition, linear reciprocating ball-on-flat sliding wear testing was performed to measure the coefficient of friction (COF) and wear resistance as well as to understand the wear behavior.

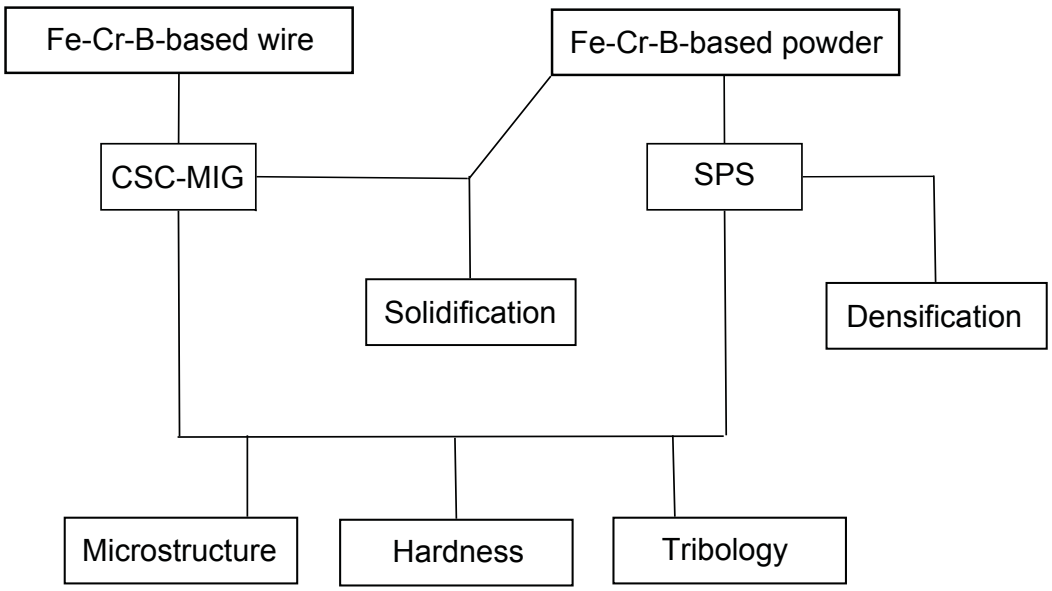

Figure 3.1: Schematic of the research methodology

Table 3.1: Chemical compositions of the starting alloys (wt.%)

Element	Fe	Cr	B	Si	Mn	C	S
Wire	Bal.	26.5–31.5	3.4–4.2	1.1–2.1	1.1–2.2	-	-
Powder	Bal.	43.0–46.0	5.6–6.2	1.8–2.3	-	0.17 max.	0.02 max.

CHAPTER 4

Understanding the Solidification and Microstructure Evolution During CSC-MIG Welding of Fe–Cr–B-Based Alloy

[1]Ahmad A. Sorour[*], Richard R. Chromik[*], Raynald Gauvin[*], In-Ho Jung[*] and Mathieu Brochu[*]

[*]Department of Mining and Materials Engineering, McGill University, 3610 University Street, Montreal, QC H3A 0C5, Canada

As the CSC-MIG process has been shown to offer higher transfer rate, lower heat input and higher welding stability than the conventional MIG process, the Fe–Cr–B-based alloy was fabricated by the CSC-MIG process. The solidification behavior was investigated and microstructural analysis was performed to identify the phases and the morphology of the boride phase. The volume fraction of the phases was measured.

[1]Published: A.A. Sorour, R.R. Chromik, R.Gauvin, I.Jung and M.Brochu, Materials Characterization, Vol.86, pp.127–138, 2013

Abstract

The present is a study of the solidification and microstructure of Fe–28.2%Cr–3.8%B–1.5%Si–1.5%Mn (wt.%) alloy deposited onto a 1020 plain carbon steel substrate using the controlled short-circuit metal inert gas welding process. The as-solidified alloy was a metal matrix composite with a hypereutectic microstructure. Thermodynamic calculation based on the Scheil-Gulliver model showed that a primary $(Cr,Fe)_2B$ phase formed first during solidification, followed by an eutectic formation of the $(Cr,Fe)_2B$ phase and a body-centered cubic Fe-based solid solution matrix, which contained Cr, Mn and Si. Microstructure analysis confirmed the formation of these phases and showed that the shape of the $(Cr,Fe)_2B$ phase was irregular plate. As the welding heat input increased, the weld dilution increased and thus the volume fraction of the $(Cr,Fe)_2B$ plates decreased while other microstructural characteristics were similar.

Keywords

Fe–Cr–B alloy; Metal matrix composite; CSC-MIG welding; Electron microscopy; Thermodynamic modeling

4.1 Introduction

Fe–Cr–B-based alloys are metal matrix composite materials, which usually consist of boride particles, such as $(Cr,Fe)_2B$, embedded in a Fe-based solid solution matrix [11–13, 22, 24, 27]. The Fe–Cr–B-based alloys have been reported to exhibit high hardness and excellent wear and corrosion resistance [8, 11, 13, 14, 69, 70]. Such alloys are typically deposited by thermal spray processes, such as detonation gun [13, 24], high velocity oxygen fuel (HVOF) [8, 14, 22] and twin wire arc spray (TWAS) [18]. In addition, the alloy has been deposited by welding processes, such as plasma transferred arc (PTA) [20].

Changes to the process parameters and the starting composition of this alloy have been shown to affect the solidification microstructure, which consequently affects the properties of the deposited alloy [11–13, 15, 24, 27]. Fe–Cr–B-based alloys deposited by the HVOF process are typically composed of small boride precipitates and oxides, an amorphous or mixed amorphous/crystalline matrix, pores and unmelted particles [8,14,22], whereas the detonation gun process produces similar phases without the amorphous phase, pores or unmelted particles [13, 24]. Alloys produced by the PTA welding have significantly different microstructure than the HVOF process. The PTA deposition consists of larger and longer boride particles in a complete crystalline matrix [20]. The PTA deposition shows better wear resistance because of the resulting microstructure. This indicates that the welding technique has the potential to provide better alloy performance.

It has been shown that the addition of boron to the Fe–Cr alloy lowers its melting temperature and leads to the Fe and Cr boride formation, such as $(Cr,Fe)_2B$ [30].

This boride has a hardness of about 24 GPa (Chapter 7). When the volume fraction of the $(Cr,Fe)_2B$ particles increases, the bulk hardness increases [11, 12, 15], which tends to improve the wear resistance [11]. While the effect of the $(Cr,Fe)_2B$ particles on the alloy properties has been investigated, little attention has been given to the effect of the fabrication process on the microstructural and solidification behavior for this alloy.

One of the most widely used welding processes is gas metal arc welding (GMAW), also known as metal inert gas (MIG) welding. In this process, an arc is stroked between an electrode wire (anode) and a workpiece (cathode). The arc melts the wire electrode and part of the workpiece, forming a weld pool. An upgraded version of this welding process, known as the controlled short-circuit (CSC-MIG) welding, was recently invented to reduce the heat input and spatter by accurate controlling of the position and speed of the electrode wire [31]. The deposition process in the CSC-MIG involves four stages [31]. First, the current is applied to generate the arc, forming the droplet and weld pool. Then, the wire is fed down toward the substrate until the droplet contacts the weld pool, activating a short circuit. Upon that, the droplet is released to the pool. Finally, the wire is retracted to break the liquid connection between the wire tip and weld pool. The main advantages of the CSC-MIG process over the conventional MIG process are higher transfer rate, lower heat input and higher welding stability, which leads to negligible spatter [31].

Understanding the microstructural and solidification behavior of this alloy is essential to optimize the process to obtain a desired microstructure in order to improve the mechanical and tribological properties. The main purpose of this work was to

investigate the microstructure development of the Fe–Cr–B-based alloy when deposited by the CSC-MIG process onto a plain carbon steel substrate. The microstructure investigation was carried out using X-ray diffraction (XRD), cold field emission scanning electron microscopy (CFE-SEM), energy dispersive spectroscopy (EDS), electron backscatter diffraction (EBSD) and scanning transmission electron microscopy (STEM). In addition, thermodynamic calculations and differential scanning calorimeter (DSC) analysis were performed to understand the solidification behavior of this alloy.

4.2 Experimental Procedures

A commercial Fe–Cr–B-based alloy, designated as Armacor M, was selected for this research. It was received as a cored wire with a diameter of 1.8 mm. This wire was designed for twin wire arc spray (TWAS) process. The chemical composition of this alloy, as given by the manufacturer's data sheet, is presented in Table 4.1.

Table 4.1: Chemical composition of the starting Fe–Cr–B-based alloy

Element	Fe	Cr	B	Si	Mn
wt.%	Bal.	26.5–31.5	3.4–4.2	1.1–2.1	1.1–2.2
at.%	Bal.	24.3–27.7	15.0–17.8	1.9–3.4	1.0–1.8

The deposition was performed using the CSC-MIG welding system, which is described in detail elsewhere [71]. Single beads of the Fe–Cr–B-based alloy were deposited onto a flat and ground plain carbon steel (AISI 1020) plates approximately 100 mm × 40 mm × 3 mm in size. Table 4.2 presents the welding parameters used to deposit three specimens designated as M1, M2 and M3. These parameters

were selected based on visual inspection of discontinuity, cracking and fusion to the substrate.

Table 4.2: The CSC-MIG welding process parameters

Welding parameter	M1	M2	M3
Heat input (J/mm)	78 ± 5	220 ± 5	450 ± 10
Arc voltage (V)	19	25	30
Arc current (A)	100	200	300
Arc time (s)	0.01	0.01	0.01
Short-circuit current (A)	75	150	200
Short-circuit time (s)	0.01	0.01	0.01
Wire feed speed (mm/s)	183	217	250
Shielding gas	Ar	Ar	Ar
Flow rate (m^3/s)	0.0189	0.0189	0.0189

For cross-sectional analysis, the specimens were cut perpendicular to the welding direction and hot mounted. Then, the specimens were ground and polished with standard metallography procedures with a final polish using colloidal silica. The polished specimens were cleaned in an ultrasonic bath with acetone for 10 min.

Macrostructure analysis of the cross-sectional welding beads was carried out by acquiring micrographs using a Nikon Epiphot 200 light microscopy. To measure the dilution ratio, image analysis was performed on three micrographs (50x magnification) for each deposition condition using a Clemex Vision Professional software. The dilution ratio was calculated by dividing the cross-sectional area corresponding to the portion of the substrate that melted during deposition by the total cross-sectional area of the weldment (filler + molten portion of the substrate).

Microstructure analysis was carried out using a Hitachi SU-8000 cold field emission scanning electron microscopy (CFE-SEM), using both secondary electron (SE) and

backscattered electron (BSE) imaging. The microscope was equipped with a X-MAX silicon drift detector (SDD) as energy dispersive spectroscopy (EDS) with a collection area of 80 mm^2, which was used for qualitative elemental analysis. To measure the volume fractions of the phases, image analysis was performed on twenty BSE micrographs (2500x and 3000x magnifications) of each polished specimen. To investigate the shape of the particles, the specimen was deeply etched in a solution composed of one part HCL, one part HNO_3 and one part H_2O for 5 min. The etched specimen was then analyzed using the SE mode at low accelerating voltage of 1 kV.

An electron backscatter diffraction (EBSD) system was used to acquire EBSD maps and patterns. The EBSD data were acquired and analyzed with the Channel 5 system software. In addition, a thin foil specimen was imaged using the scanning transmission electron microscopy (STEM) bright-field mode at 30 kV accelerating voltage with a YAG-type transmitted electron detector placed below the specimen. The thin foil was prepared using a Hitachi NB5000 focused ion beam (FIB).

To identify the phases and measure their lattice parameters, X-ray diffraction (XRD) analysis was performed using a Philips PW1070 diffractometer employing Cu Kα ($\lambda = 0.15406$ nm) radiation. The lattice parameters measurement was carried out using W powder as standard for peak position correction and the refinement of the patterns was carried out using XLAT software [72]. XRD scans were carried out under the operation conditions of 40 kV and 20 mA with a 2θ step size of 0.01 deg/s and a dwell time per step of 1 sec in the 2θ range of 30–100°. For XRD scan, multi-pass beads were welded into same plate above. Then, a 15×10 mm sample was cut from the welding beads, ground from the top surface progressively down to 800 grit to

produce a flat surface from the welded alloy. Before the XRD scan, the sample was cleaned in an ultrasonic bath with acetone for 10 min.

The differential scanning calorimeter (DSC) measurement was performed using a Netzsch DSC 404F1 Pegasus high temperature DSC. Small fragments were carefully cut from M2 weldment. The small fragments (17.5 mg) and the sapphire standard were placed in an alumina crucible and then heated from 22 ℃ to 1,600 ℃ at 20 K/min heating rate under argon gas (flow rate $\sim$ 1,000 mm^3/s).

4.3 Thermodynamic Modeling Procedures

Thermodynamic analysis using the FactSage thermochemical software with the FSStel database [73] was carried out to predict the partial liquidus surface projection, the isothermal equilibrium phase diagrams, the solidification paths and the chemical composition of each phase. As Cr_2B-rich and Fe_2B-rich solid solutions are not contained in the present FSStel database, these two solutions were newly modeled by the Compound Energy Formalism [74] using two sublattice, $(Cr,Fe)_2B$ and $(Fe,Cr)_2B$, to reproduce the phase diagram information [49] of the Fe_2B-Cr_2B section. The calculations were performed with a phase set reduced to LIQUID, BCC, FCC, orthorhombic Cr_2B-rich solid solution, tetragonal Fe_2B-rich solid solution and the other phases from the FSStel database. Because of the non-equilibrium solidification, the solidification path, solute distribution and phase fraction were calculated based on the Scheil-Gulliver model [75, 76] with 1 ℃ step size.

4.4 Results

4.4.1 Macrostructure of the Weldments

Figure 4.1 shows the weldment cross-sectional micrographs for M1, M2 and M3 specimens. The specimen M1 was deposited with the lowest heat input and the specimen M3 was deposited with the highest heat input. As the heat input increased, the deposition volume and weld dilution increased. There was no evidence of weld dilution in M1 specimen. The dilution volume percentage (vol.%) was calculated using the areas defined in Figure 4.1 as follows:

$$Dilution = \frac{P}{W + P} \times 100 \tag{4.1}$$

The dilution weight percentage (wt.%) was calculated, by assuming the depositions density as 7.4 g/cm^3, and presented in Table 4.3 along the estimated chemical compositions for M1, M2 and M3 specimens. After dilution, the chemical compositions of M1 and M2 specimens were similar while that of M3 was different. Although some porosity was observed in M1 specimen (deposited at low heat input), no porosity was observed at higher heat input within M2 and M3 specimens.

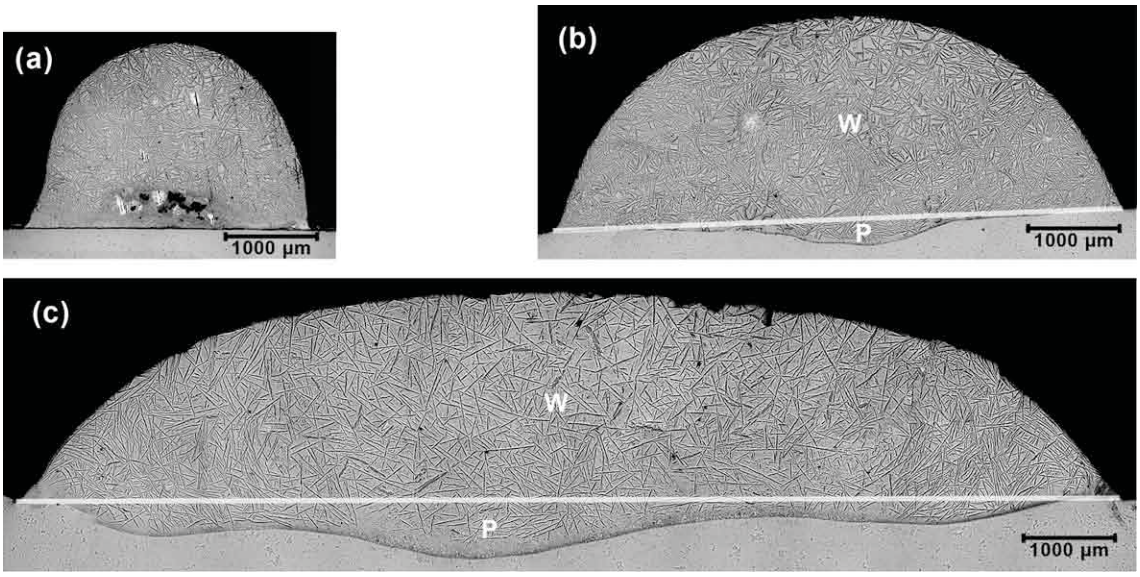

Figure 4.1: Cross-sectional light micrographs of the weldment of (a) M1, (b) M2 and (c) M3 specimens

Table 4.3: Dilution percentage and the chemical compositions of the deposited alloys

			Chemical composition after deposition					
Specimen	Dilution			Fe	Cr	B	Si	Mn
M1	vol.%	0	wt.%	Bal.	26.5–31.5	3.4–4.2	1.1–2.1	1.1–2.2
	wt.%	0	at.%	Bal.	24.3–27.7	15.0–17.8	1.9–3.4	1.0–1.8
M2	vol.%	3.0 ± 2.4	wt.%	Bal.	25.7–30.5	3.3–4.1	1.0–2.0	1.0–2.0
	wt.%	3.2 ± 2.6	at.%	Bal.	23.7–27.0	16.4–17.5	1.7–3.3	0.9–1.7
M3	vol.%	19 ± 6.0	wt.%	Bal.	22.0–26.3	2.8–3.5	1.0–1.8	1.0–1.8
	wt.%	20 ± 6.3	at.%	Bal.	20.7–23.9	12.7–15.3	1.7–3.0	0.9–1.5

4.4.2 Microstructure and Phase Analysis

Figure 4.2 shows BSE micrographs for the specimen M2. The as-deposited alloy was composed of dark-contrast big particles (denoted as β), dark-contrast small particles (denoted as β') and a light-contrast matrix. EDS analysis (Figure 4.3) showed that the dark-contrast particles (β and β') were rich in B, Cr and Fe while the matrix was rich in Fe, Cr, Mn and Si. It should be noted that the EDS spectrums of other particles were similar. Likewise, the EDS spectrums of the matrix throughout the deposition were similar. In addition, the ratios of Fe to Cr within the β particles as well as the matrix were similar.

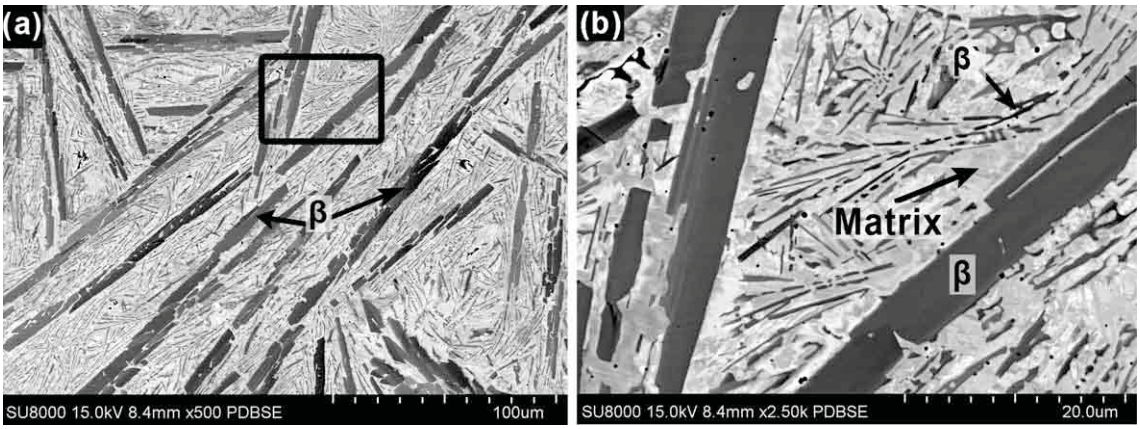

Figure 4.2: SEM/BSE micrographs of M2 specimen as polished at (a) low magnification and (b) high magnification. β and β' particles referred to $(Cr,Fe)_2B$ while the matrix referred to Fe-based solid solution

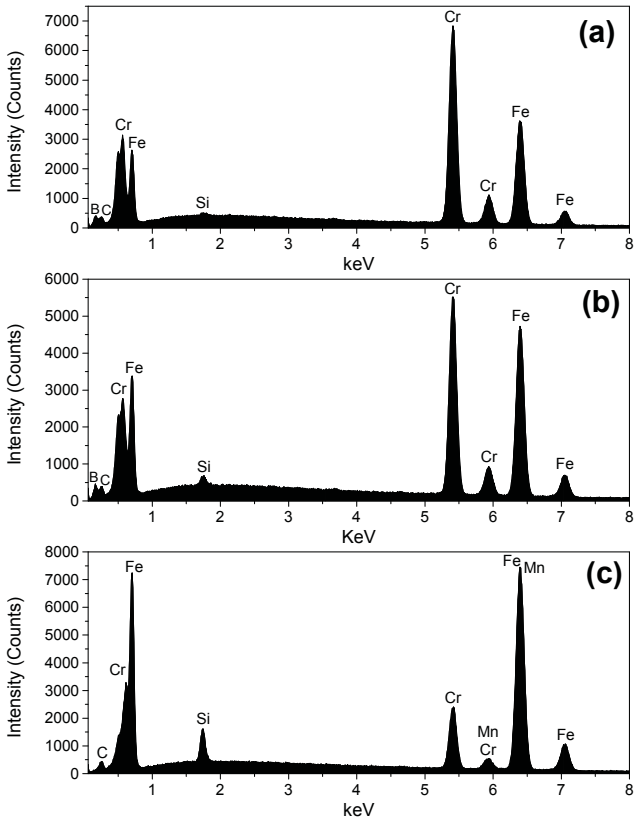

Figure 4.3: Typical EDS analysis at 15 keV of (a) β particle, (b) β' particle and (c) the matrix of M2 specimen

The volume fraction of the boride particles (β and β') and the matrix were measured using image analysis of the BSE micrographs for M1, M2 and M3 specimens, and the results are presented in Table 4.4. The particles volume fractions for M1 and M2 specimens were similar while that of M3 specimen was lower.

Table 4.4: Volume fractions of the particles and the matrix for M1, M2 and M3 specimens as well as the modeling alloy

	Measured by image analysis		Calculated by thermodynamic	
Specimen	Particles (β and β') (vol.%)	Matrix (vol.%)	Particles (β and β') (vol.%)	Matrix (vol.%)
M1	44.6 ± 3.9	55.5 ± 3.9	44.2	55.8
M2	44.2 ± 2.7	55.8 ± 2.8	44.2	55.8
M3	37.2 ± 2.6	62.9 ± 2.7	35.2	64.7

Figure 4.4 shows the XRD result for M2 specimen. The identified phases from this XRD result with their crystal structure and reported unit cell lattice parameters are provided in Table 4.5. The first set of peaks was referred to body-centered cubic (BCC) structure α-Fe. The second set corresponded to orthorhombic $Fe_{1.1}Cr_{0.9}B_{0.9}$, which is usually reported as $(Cr,Fe)_2B$ [46]. The lattice parameters of these phases were measured and provided in Table 4.5 as well. Similar patterns were obtained for M1 and M3 specimens.

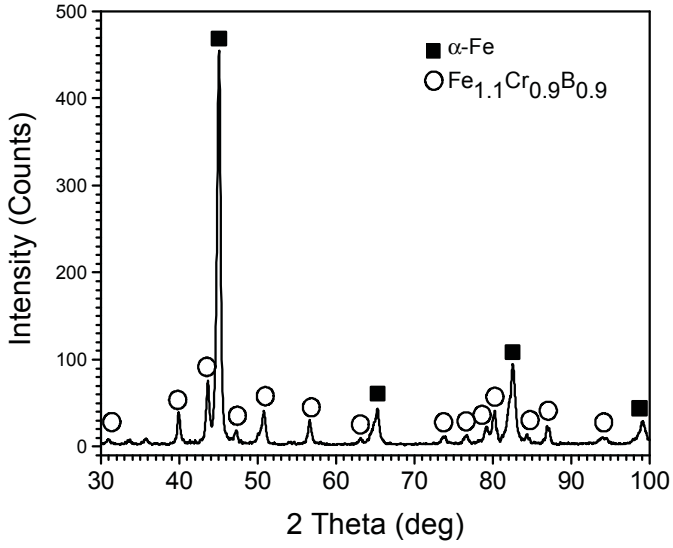

Figure 4.4: XRD result of the specimen M2

Table 4.5: Identified phases and their properties from XRD of M2 specimen

Compound name	JCPDS file #	Crystal system	Reported lattice parameters (Å)[1]				Measured lattice parameters (Å)[2]		
			a	b	c		a	b	c
α-Fe	006-0696	Cubic	2.866	2.866	2.866	[77]	2.878 ±0.006	2.878 ±0.006	2.878 ±0.006
$Fe_{1.1}Cr_{0.9}B_{0.9}$	072-1073	Orthorhombic	14.57	7.32	4.22	[46]	14.561 ±0.088	7.327 ±0.053	4.209 ±0.01

[1] These values were reported in the literature
[2] These values were measured using XRD for the investigated alloy

To investigate the shape of the boride particles, SE analysis of the deep etched specimen was performed, as shown in Figure 4.5. The shape of β and β' particles was irregular plate-like. These plates do not seem to be in contact with each other.

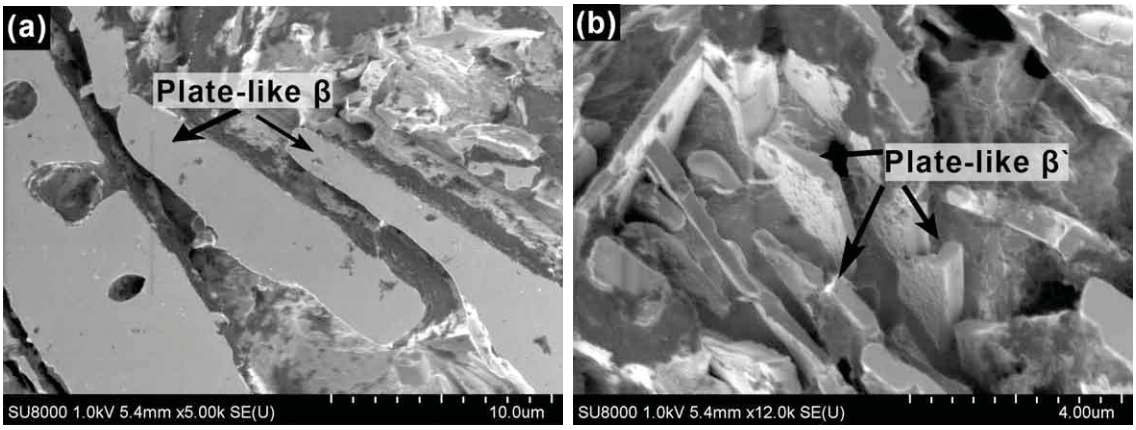

Figure 4.5: SEM/SE micrographs of the etched M2 specimen, showing the shape of (a) β particles and (b) β' particles

Figure 4.6 shows the BSE micrographs of the as-polished M2 specimen at low accelerating voltage (5 keV) at different tilt angles. The brightness level of the boride β particles was different from particle to particle (Figure 4.6a). These differences in

brightness changed when the specimen was tilted by 4° (Figure 4.6b); e.g., the particles labeled G became lighter while the particle labeled H became darker. Figure 4.7 shows the SEM micrograph of M2 specimen with EBSD patterns of three areas of β particles labeled as a, b and c. The EBSD patterns of the particles were well matched with the orthorhombic $(Cr,Fe)_2B$ (#072-1073, Table 4.5). Points a and b had similar orientation whereas that of point c was different.

Figure 4.8a shows the BSE micrograph of β particle at 5 keV accelerating voltage. The brightness level changing was also observed within β particle. The SE micrograph (Figure 4.8b) shows that this variation was not due to the topography. However, the EBSD map (Figure 4.8c) shows that it was due to the orientation changing. Although the BSE analysis was not able to detect similar fluctuation within the β' particles, parallel fringes were clearly shown in STEM analysis (Figure 4.9) but at much smaller scale size. These faults always lie parallel to the side of greater length. Unfortunately, the EBSD mapping of the β' was not being able to be done due to a low scattering of the electrons.

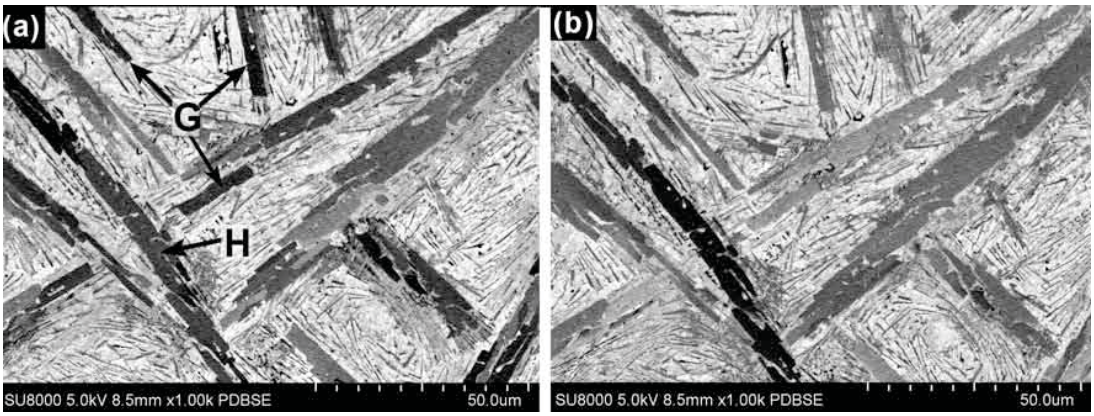

Figure 4.6: BSE micrographs of the as-polished M2 specimen at 5 keV accelerating voltage, showing a channeling contrast at (a) tilt angle = 0° and (b) tilt angle = 4°

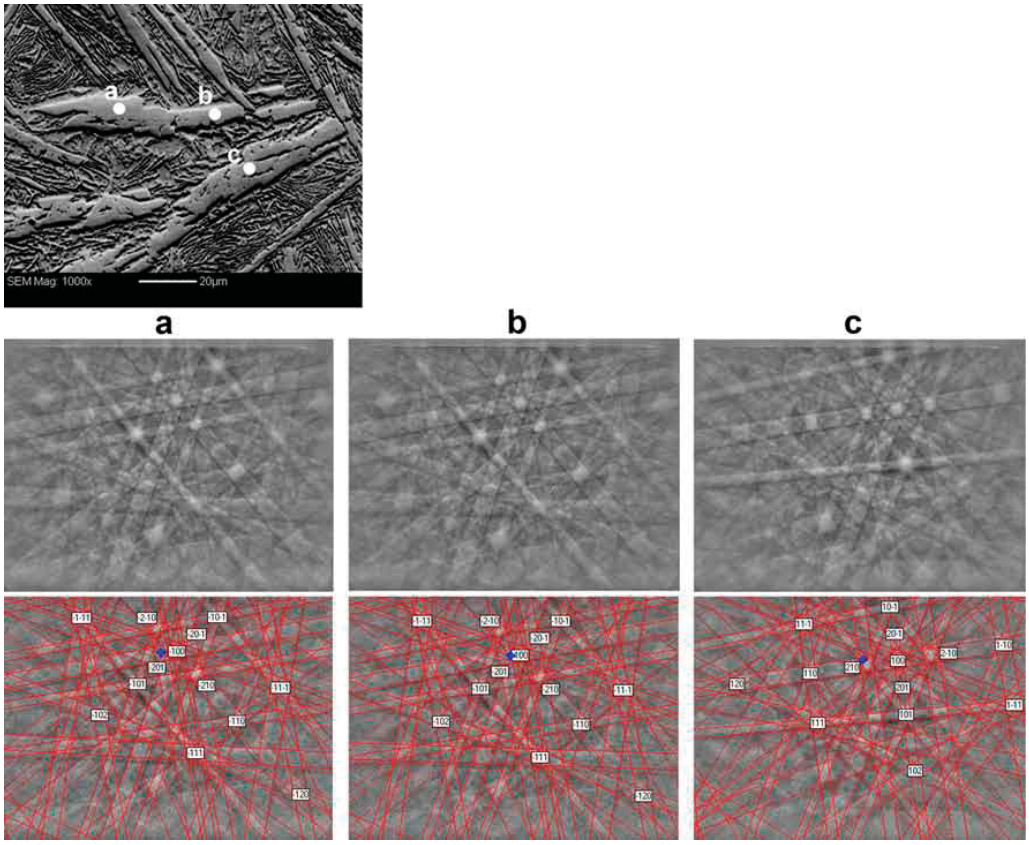

Figure 4.7: SEM micrograph of M2 specimen and EBSD patterns for three areas of β particles as labeled (a, b and c) with their computer simulation indexed as $Fe_{1.1}Cr_{0.9}B_{0.9}$

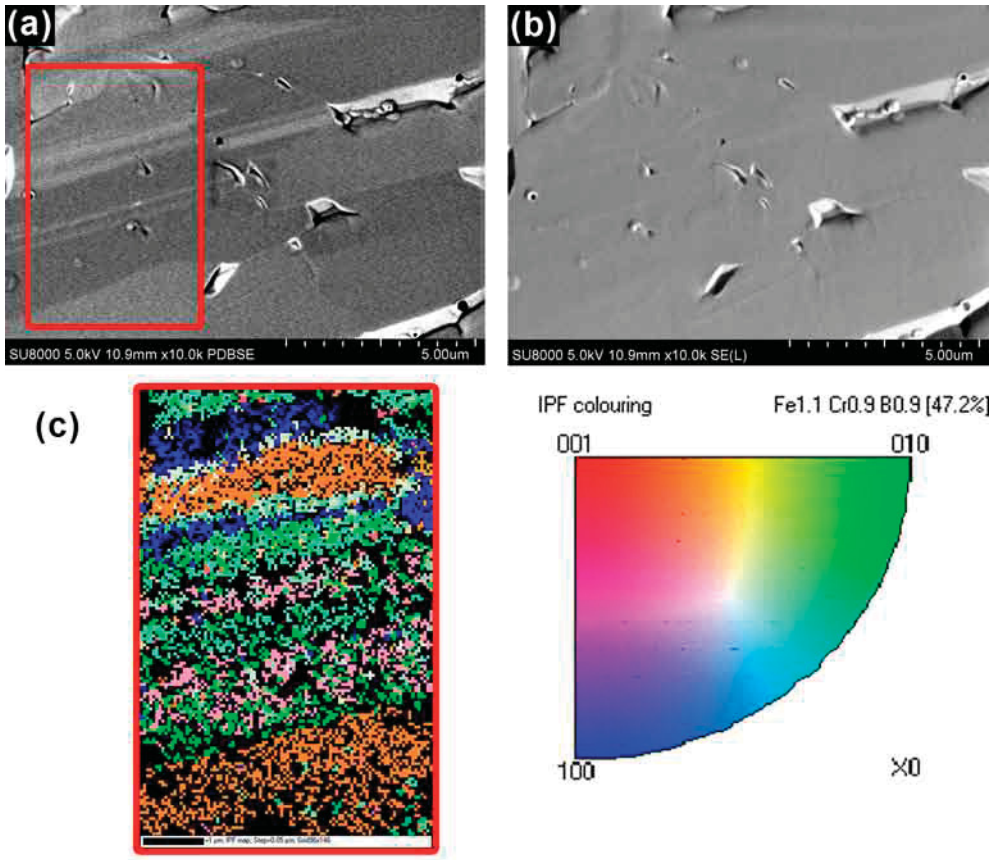

Figure 4.8: (a) SEM/BSE micrograph and (b) SEM/SE micrograph of β particle for M2 specimen at 5 keV accelerating voltage with a corresponding (c) EBSD orientation map

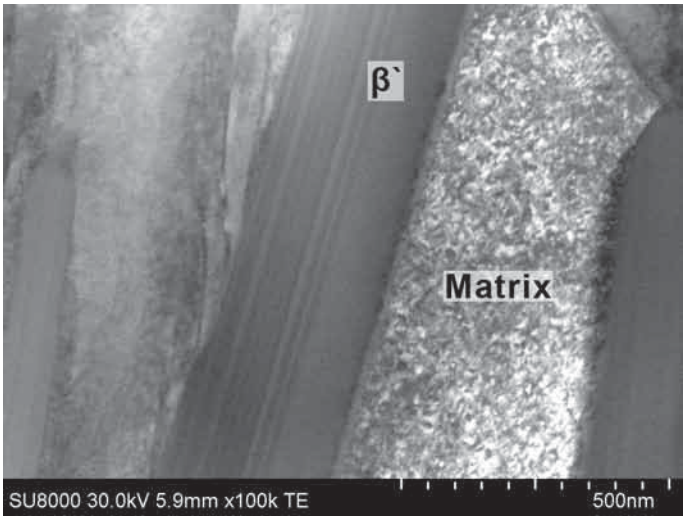

Figure 4.9: STEM imaging of M2 specimen thin foil at 30 keV accelerating voltage, showing parallel faults within the β' particle

4.5 Discussion

Prior to discussing the results on the microstructure, a thermodynamic analysis of the solidification was performed to better understand the difference in solidified structures and related them with the processing parameters. The thermodynamic analysis is presented in the following section.

4.5.1 Thermodynamic Analysis

Figure 4.10 shows the partial liquidus surface projection for the B–Cr–Fe ternary system calculated from the FactSage with the FSStel database and the new $(Cr,Fe)_2B$ and $(Fe,Cr)_2B$ solid solutions. In the diagram, the maximum ranges of solid solutions of $(Fe,Cr)_2B$, $(Cr,Fe)_2B$ and (Fe,Cr) BCC are also depicted as thick lines. One of

the most interesting features related to the solidification of $(Cr,Fe)_2B$ phase is the existence of local minimum (1,206 ℃) on the univariant line between $(Cr,Fe)_2B$ and BCC phase. Due to this local minimum, the solidification paths of M2 and M3 investigated in the present study can be:

$$L \rightarrow L + (Cr,Fe)_2B \rightarrow (Cr,Fe)_2B + \alpha$$

That is, $(Fe,Cr)_2B$ phase cannot be produced in the solidification process of M2 and M3 alloys.

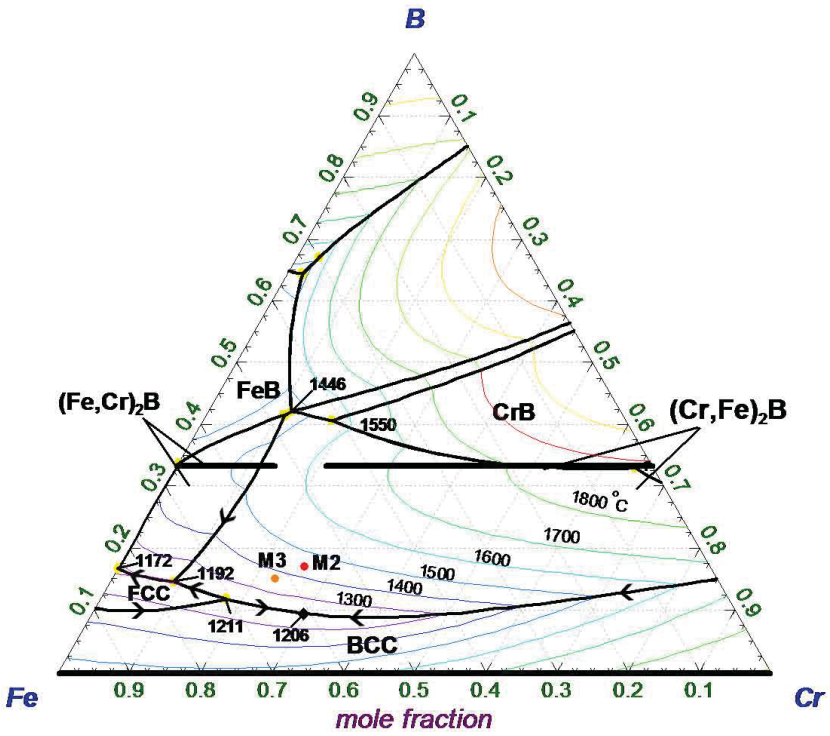

Figure 4.10: Partial liquidus projection for the B–Cr–Fe system. The circles represent approximately the composition of M2 and M3 alloys.

Figure 4.11 shows the calculated isothermal ternary B–Cr–Fe phase diagrams at 900 ℃ (1,173 K) and 1,100 ℃ (1,373 K). These diagrams are in agreement with the work of Do et al. [12], who also recently calculated the diagrams using Thermocalc with TCFE2000 database and two additional $(Cr,Fe)_2B$ and $(Fe,Cr)_2B$ solid solutions. Moreover, the diagrams are in reasonable agreement with the compiled diagrams by Villars et al. [78].

According to these diagrams, the equilibrium stable phases for M2 and M3 alloys at 1,100 ℃ were $(Cr,Fe)_2B$ and BCC solid solutions, which were in agreement with that predicted in Figure 4.10. The phase diagram at 900 ℃ indicates that if the deposited alloy heat treated at 900 ℃ for long duration time, some of BCC phase will transform to FCC. However, the FCC phase was not expected to form in the solidified specimen because the time duration upon solidification until the cooling down of the sample was not sufficient.

Heard et al. [79] found that the cooling rate of the Al-Si system deposited by the CSC-MIG process was about 10^3 ℃/s. Although the cooling rate of Fe–Cr–B-based alloy fabricated by the CSC-MIG process has not been measured, it was expected to be in the range of 10^2–10^4 ℃/s, which is too high to be considered as equilibrium solidification and too low to be considered as rapid solidification. As a first attempt to study the solidification behavior of this alloy, we used the Scheil-Gulliver model [75,76], which has been widely applied to study the solidification behavior of alloys [80–83]. This model assumes complete diffusion in the liquid phase and no diffusion in the solid phases. This model is expected to provide reasonable estimates of the evolution of the phase fractions and solute distribution during the non-equilibrium solidification.

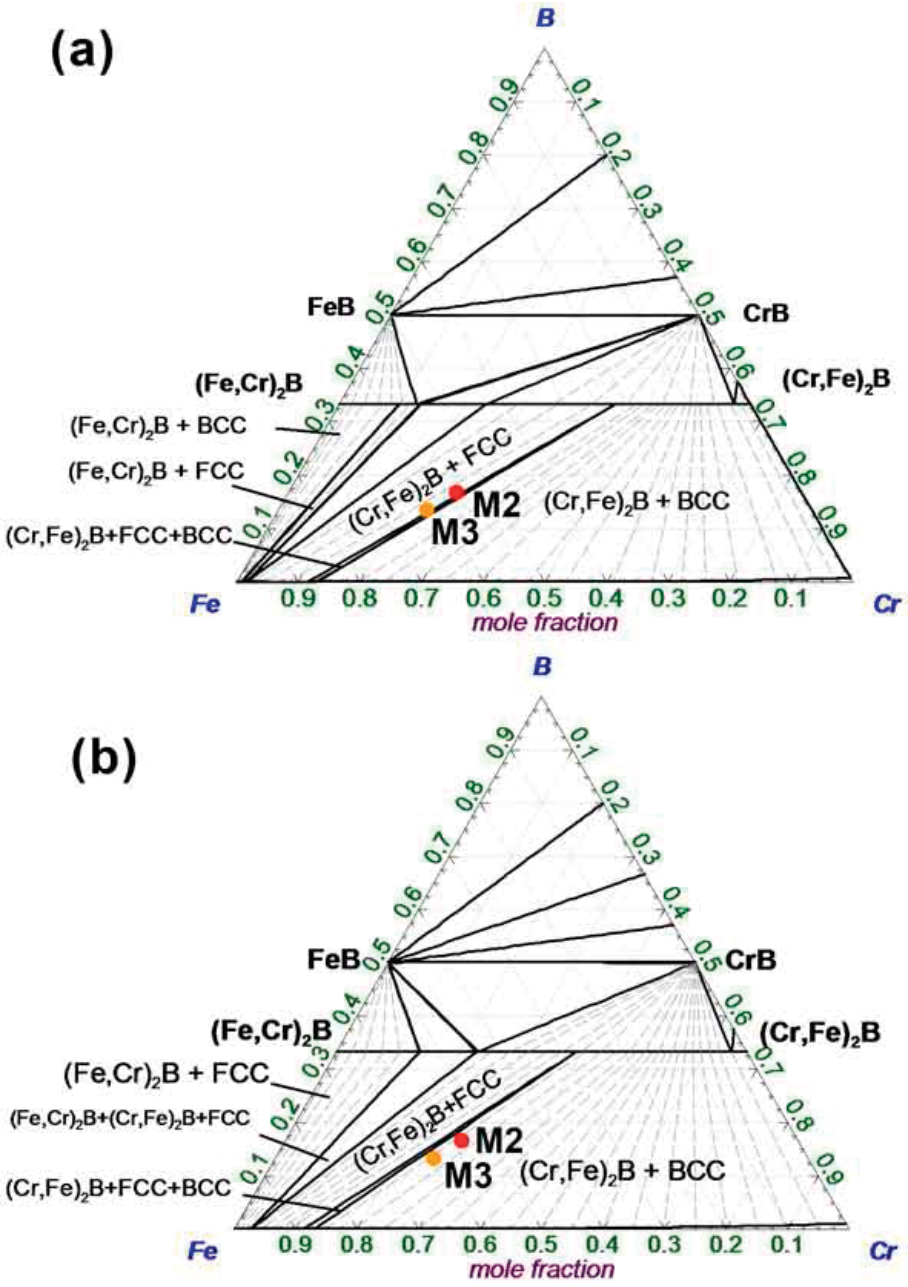

Figure 4.11: Isothermal ternary B–Cr–Fe phase diagrams at (a) 900 ℃ (1,173 K) and (b) 1,100 ℃ (1,373 K). The circles represent approximately the composition of the M2 and M3 specimens.

The composition of M1 and M2 specimens (Table 4.3) was considered as 65%Fe–28.2%Cr–3.8%B–1.5%Si–1.5%Mn (in wt.%) and that of M3 as 70.2%Fe–24%Cr–3%B–1.4%Si–1.4%Si (wt.%). Using thermodynamic calculation based on the Scheil-Gulliver model in the FactSage software, the phase distributions during the solidification were plotted in Figure 4.12 as a function of the temperature for M2 and M3 specimens. In addition, chemical composition of each phase at transition temperatures (liquidus and solidus temperatures) is given in Table 4.6 and Table 4.7.

When M2 specimen (Figure 4.12a and Table 4.6) cooled down, a primary $(Cr,Fe)_2B$ phase (denoted as β) started to solidify at the liquidus temperature (predicted to be 1,476 ℃) and its amount increased up to 26.6 wt.% as the temperature decreased. As a result of the primary $(Cr,Fe)_2B$ phase formation, the concentration of Cr and B decreased in the liquid phase while that of Fe, Mn and Si increased. At 1,248.4 ℃ (modeled to be the eutectic temperature), off-eutectic solidification occurred and resulted in a formation of $(Cr,Fe)_2B$ (denoted as β') and a BCC phase composed of Fe, Cr, Mn, Si and a low concentration of B. As the eutectic solidification was progressing, the chemical composition of the liquid phase was changing, and thus the eutectic temperature was reducing. As a result, the eutectic phases fraction increased as the temperature reduced. At 1,208 ℃, all the remaining liquid solidified and the final modeled percentage of the $(Cr,Fe)_2B$ phase was 41.4 wt.% (26.6 wt.% for the primary and 14.8 wt.% for the eutectic) and that of the BCC solid solution was 58.6 wt.%.

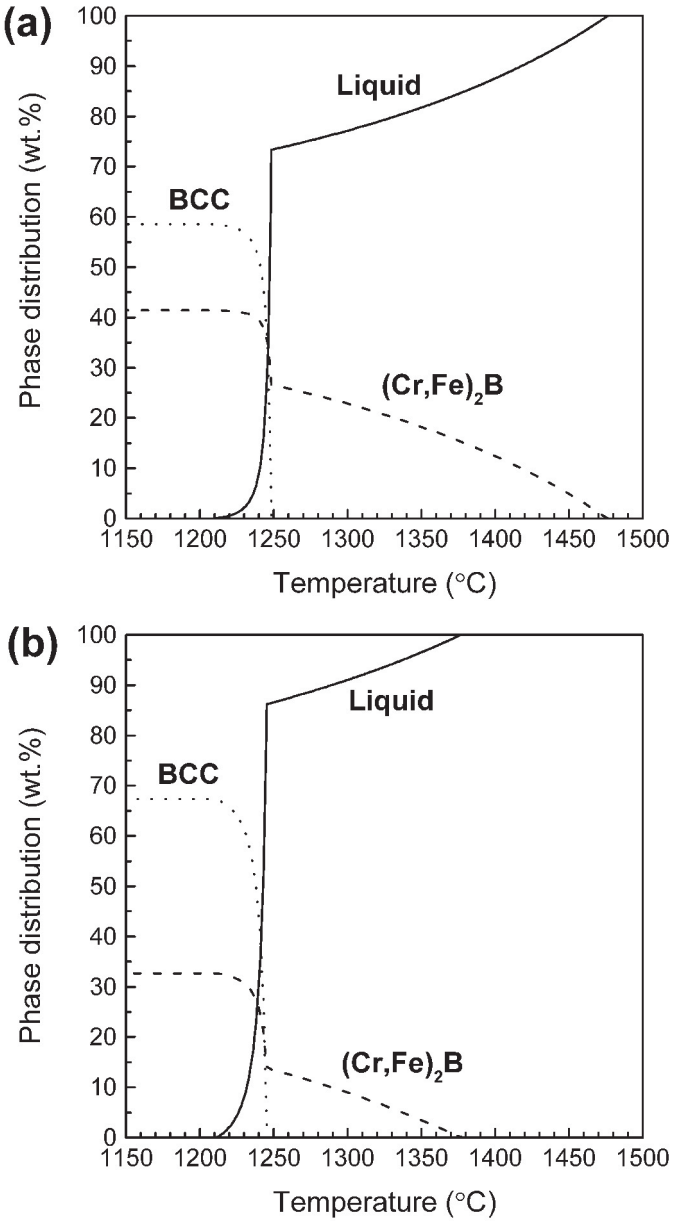

Figure 4.12: The phase distribution as a function of the temperature based on the Scheil-Gulliver model in the FactSage software for (a) M2 specimen: 65%Fe–28.2%Cr–3.8%B–1.5%Si–1.5%Mn (wt.%) and (b) M3 specimen: 70.2%Fe–24%Cr–3%B-1.4%Si–1.4%Si (wt.%)

Table 4.6: The modeled phases weight percent and the chemical composition of each phase for the liquidus and solidus temperatures for M2 specimen: 65%Fe–28.2%Cr–3.8%B–1.5%Si–1.5%Mn (wt.%)

Temperature (℃)	Phase	Phase (Wt.%)	Chemical composition (wt.%)				
			Fe	Cr	B	Si	Mn
1,476	Liquid	100	65.0	28.2	3.8	1.5	1.5
	$(Cr,Fe)_2B$	0	41.5	49.4	9.1	-	-
1,248.4	Liquid	73.4	73.4	20.6	1.9	2.0	2.0
	$(Cr,Fe)_2B$	26.6	41.8	49.1	9.1	-	-
1,208	BCC	58.6	81.6	13.2	0.019	2.6	2.6
	$(Cr,Fe)_2B$	41.4	41.5	49.4	9.1	-	-

Table 4.7: The modeled phases weight percent and the chemical composition of each phase for the liquidus and solidus temperatures for M3 specimen: 70.2%Fe–24%Cr–3%B–1.4%Si–1.4%Mn (wt.%)

Temperature (℃)	Phase	Phase (Wt.%)	Chemical composition (wt.%)				
			Fe	Cr	B	Si	Mn
1,377	Liquid	100	70.2	24.0	3.0	1.4	1.4
	$(Cr,Fe)_2B$	0	43.1	47.8	9.1	-	-
1,245.4	Liquid	86.2	74.5	20.2	2.0	1.6	1.6
	$(Cr,Fe)_2B$	13.8	43.1	47.8	9.1	-	-
1,210	BCC	67.3	83.5	12.3	0.02	2.1	2.1
	$(Cr,Fe)_2B$	32.7	42.7	48.2	9.1	-	-

The solidification behavior for M3 specimen (Figure 4.12b and Table 4.7) was similar to that of M2 specimen. However, the liquidus and eutectic temperatures were lower (1,377 ℃ and 1,245.4 ℃, respectively) and the solidified phases fractions were different. As a result of 20 wt.% Fe dilution (Table 4.3), the modeled $(Cr,Fe)_2B$ fraction of the solidified M3 specimen (at 1,210 ℃) was decreased to 32.7 wt.% (13.8 wt.% for the primary and 18.9 wt.% for the eutectic) and that of the BCC solid solution was increased to 67.3 wt.%.

Therefore, the solidified alloy was hypereutectic, where the primary $(Cr,Fe)_2B$ phase forms first, followed by eutectic formation of the $(Cr,Fe)_2B$ phase and the BCC Fe-based solid solution. Although Do et al. [12, 27] has modeled the solidification path of the Fe–Cr–B-based alloy with various compositions based on the equilibrium calculation, this was the first attempt to simulate the solidification path for the investigated alloy compositions based on the Scheil-Gulliver model.

4.5.2 DSC Analysis

Figure 4.13 shows the DSC result for M2 specimen. There are at least three overlapping melting endothermic peaks. The DSC curve was fitted with three peaks. The total transition enthalpy was 210 J/g, including 16 J/g for peak 1, 143 J/g for peak 2 and 51 J/g for peak 3. Partial melting (peak 1) started at 1,205 ℃ followed by two melting reactions (peaks 2 and 3). The measured melting temperature was in agreement with the thermodynamic calculations (Figure 4.12a and Table 4.6), where the complete solidification occurred at 1,208 ℃ and the predicted eutectic temperature was 1,248.4 ℃. For similar alloys to those studied here, two previous

research groups reported the formation of the liquid by eutectic reaction of the α-Fe phase and $(Cr,Fe)_2B$ to be between 1,150 ℃ to 1,272 ℃, depending on the composition of the alloy [11, 30].

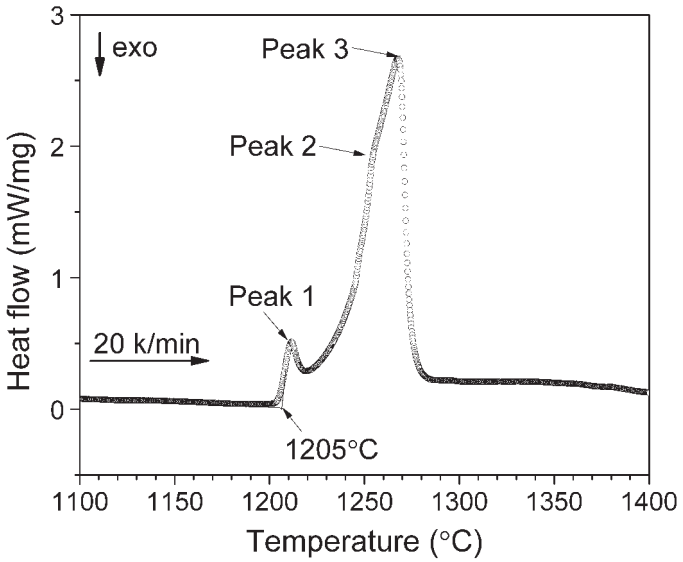

Figure 4.13: DSC curve for the specimen M2

The eutectic solidification seemed to occur at three steps. Small portion (24.3%) of the remaining liquid phase solidified first. As a result, the liquid composition changed and consequently the eutectic temperature reduced. Then, the second solidification (68.1%) occurred at lower temperature. For the same reason, all the remaining liquid solidified to the eutectic phases (7.6%) at further lower temperature. Therefore, the peaks 1, 2 and 3 (Figure 4.13) represented the eutectic solidification steps 3, 2 and 1, respectively. Sercombe and Schaffer [28] reported similar behavior to that observed here (Figure 4.13), where they observed a small peak at 1,150 ℃ followed by a superimposed main melting peak for melting of the Fe–Cr–B–Ni–C alloy.

4.5.3 Microstructure Characterization

Based on the experimental results, the light-contrast matrix (Figure 4.2b) corresponds to Fe-based BCC solid solution containing mainly Cr, Mn and Si. While B was not detected in the EDS analysis (Figure 4.3c), its concentration in the matrix would be 0.02 wt.%, as predicted by thermodynamic calculation (Table 4.6). Guo and Kelly [45] found that B solubility in the similar matrix ranges between 0.01–0.5 wt.%, which is much higher than that in pure iron (0.005 wt.%). This increased solubility of B is associated with alloying element addition of Cr, Mn and Si [45]. The atomic radii of Cr (0.166 nm) and Mn (0.161 nm) are larger than Fe (0.156 nm) whereas that of Si (0.111 nm) is smaller [84]. Thus, their existence in Fe could lead to expansion of the interstitial sites, allowing a higher quantity of B to dissolve. The substitution solution of Cr and Mn contributed also to the small increase of the measured lattice parameter (2.878 ± 0.006 Å) compared to that of the pure α-Fe (2.866 Å) [77], as shown in Table 4.5. Silicon which is smaller than Fe would decrease the lattice parameter, but this effect was hidden because of the smaller concentration of Si compared to Cr in our alloy. The increase of the α-Fe lattice parameter as a result of Cr addition was also investigated and confirmed by Calos et al. [85] (cited in [45]).

The dark-contrast particles (β and β') correspond to the orthorhombic Cr-rich M_2B-type phase (M = Cr, Fe), in which Fe is dissolved. This phase was conventionally denoted as $(Cr,Fe)_2B$ by previous researchers [11, 12, 48, 86, 87]. It has been shown that up to 75% of Cr atoms in the orthorhombic Cr_2B can be replaced by Fe atoms [46–48]. It has been found that when Fe replaces Cr, the lattice parameters of Cr_2B decrease [46, 47]. Thus, the lattice parameters of the Cr_2B is reduced from

$a = 14.708$ Å, $b = 7.419$ Å, $c = 4.25$ Å (for pure Cr_2B) [56] to the values shown in Table 4.5 as measured here and by previous researchers [46], which were similar.

Using the measured lattice parameters values, the composition of the $(Cr,Fe)_2B$ in the deposited alloy can be estimated. Using a calculation by Christodoulou and Calos [48], Fe/Cr ratio in the $(Cr,Fe)_2B$ phase was estimated to be 1.02. Using a calculation by Kayser and Kayser [56], the Fe/Cr ratio was estimated to be 1.5. According to EDS analysis, the Fe/Cr ratio was 1.44 ± 0.08. The ratio measured by EDS was expected to be reliable because the absorption of the Fe and Cr in the boride particles was similar as shown by the Monte Carlo simulation using CASINO software [88].

Whereas Calos et al. [85] (cited in [48]) found that Si segregates entirely into the matrix, few counts for Si were detected in β and β' particles. The Monte Carlo simulation using CASINO software [88] was performed to estimate the beam interaction within these particles. The simulation showed that the generated characteristic X-rays can reach up to 1 µm depth in these particles. Since the thickness of β' particles was close to 1 µm, the detected Si (Figure 4.3b) was likely from the interaction volume of the beam with the matrix. The small peak of Si in β particles (Figure 4.3a) probably originated from the matrix as well.

The volume fractions of the solidified phases based on thermodynamic modeling (Table 4.6 and Table 4.7) were calculated, by assuming the density of $(Cr,Fe)_2B$ as 6.8 g/cm^3 and that of the matrix as 7.61 g/cm^3, and presented in Table 4.4. Because the chemical compositions of M1 and M2 specimens were similar (Table 4.3), their calculated volume fractions were also similar. The calculated volume fractions by

thermodynamic modeling were similar to that measured by image analysis for M1, M2 and M3 specimens. This indicates that thermodynamic calculation using the Scheil-Gulliver model was in fact a valid approximation.

While the phases shown in the BSE micrograph (Figure 4.2) and analyzed by the EDS (Figure 4.3) were same for M1, M2 and M3 specimens, the measured and calculated volume fraction of the boride particles (β and β') and the matrix were different, as shown in Table 4.4. When the heat input increased during the welding, the Fe dilution increased, as shown in Figure 4.1 and Table 4.3. As a result, B concentration decreased in the deposition and thus $(Cr,Fe)_2B$ particles fraction decreased. This decrease is in agreement with Do et al. investigation for similar alloy [12].

Although some studies [59, 89] have reported the shape of the boride particles for the similar alloy as irregular plate, others [12, 13, 22] have claimed needle or rod shape. The SE micrograph of the deep etched specimen (Figure 4.5) confirmed that the shape of the β and β' particles was irregular plate-like. The variation of the boride shape between the investigations could be attributed to the cooling rate variation. Furthermore, some samples in the previous investigations have not been etched deeply enough to clearly distinguish the particles' shape. In sliding and abrasive wear, these boride plates would enhance the wear resistance compared to the needle or rod particles because they extend deeper inside the matrix and are harder to be pulled out. The formation of boride plates adds an advantage to the CSC-MIG process over the fabrication processes that provide high solidification rate.

The brightness level changing from β boride particle to particle (Figure 4.6) was

due to crystallographic orientation changing from particle to particle, as confirmed by the EBSD patterns (Figure 4.7). This phenomenon is called channeling effect. The crystallographic orientation changing was also observed within β particle (Figure-Figure 4.8a) as confirmed by the EBSD map (FigureFigure 4.8c). This orientation variations within β particle formed as a result of the crystal growth direction changing during solidification by displacement twinning, similar to what was observed in Si plates in Si-Al alloy [90, 91]. To the best of our knowledge, the orientation variation observed in the β particles at this scale has not been observed in previous works.

The parallel fringes observed within β' particles (Figure 4.9) were stacking faults. Similar stacking faults fringes have been observed in $(Cr,Fe)_2B$ [86, 87, 92], Cr_7C_3 [93], $(Cr,Fe)_7(C,B)_3$ [89] and TiB [94]. The stacking fault crystallographic plane in $(Cr,Fe)_2B$ has been found to be (1 0 0) [86, 87]. While the cause of this fault has not been well understood, some explanations have been offered. Goldfarb et al. [87] claimed that the stacking faults introduced as a result of the solid state transformation of the tetragonal $(Fe,Cr)_2B$ phase into the orthorhombic $(Cr,Fe)_2B$ phase through atomic substitution and structural adjustment [86]. Dudzinski et al. [93] suggested the origin of the stacking faults in M_7C_3 as thermal or mechanical stresses that formed in the solidified crystal and caused a plastic deformation of the crystal by partial dislocations in the fault planes.

These stacking faults (Figure 4.9) most probably formed during nucleation and growth of the boride particles. It was unlikely that the tetragonal $(Fe,Cr)_2B$ phase formed or transformed, as proposed. It was claimed [46] that the $(Cr,Fe)_2B$ is isomorphous in crystal structure with Mn_4B, which means 50% of the B-sites can be

empty and thus become $(Cr,Fe)_4B$. This metastable boride may form first during initial solidification and then transforms to the stable $(Cr,Fe)_2B$ phase by the generation of the stacking faults. It should be noted that these fringes have been shown in the TEM analysis for the Fe–Cr–B-based alloy fabricated by the other processes [14, 24] though the authors did not pay attention of them.

In addition to the effect of Fe substitution, the existence of these defects may explain why the $(Cr,Fe)_2B$ particle has higher hardness values (24 GPa, Chapter 7) than Cr_2B (13 GPa) [95] and Fe_2B (18 GPa) [95]. The high hardness of this boride plays a major role of the mechanical properties and wear performance of this alloy.

4.6 Conclusion

The CSC-MIG, as a deposition technique, was used to deposit the Fe–28.2%Cr–3.8%B–1.5%Si–1.5%Mn (wt.%) alloy onto the 1020 plain carbon steel. The solidification and microstructure evolution were investigated and the following conclusions can be drawn:

1. The alloy was successfully deposited with continuous beads as well as negligible cracks and spatter that usually form with the conventional MIG process. Moreover, the deposition did not contain oxides or porosity that were observed with thermal spray processes, except for the low heat input deposition.

2. During solidification, the primary $(Cr,Fe)_2B$ particles formed first, followed by the eutectic formation of $(Cr,Fe)_2B$ particles and the Fe-based BCC solid solution matrix containing Cr, Mn and Si. This hypereutectic microstructure

was composed of the matrix and $(Cr,Fe)_2B$ plates, which would improve the wear resistance of this alloy compared to the $(Cr,Fe)_2B$ rods that formed with thermal spray processes.

3. When the welding heat input increased, the solidification behavior and the phases were similar but the volume fraction of $(Cr,Fe)_2B$ particles decreased as a result of weld dilution.

4. Fault fringes were observed within the $(Cr,Fe)_2B$ particles. They were planar defect as twinning and stacking faults form during solidification in the primary and eutectic boride particles, respectively.

Acknowledgments

We would like to thank Mr. Nicolas Brodusch for the technical assistance. We are also grateful to Mr. Michel Trudeau and Lisa Rodrigue from the Institut de Recherche d'Hydro-Québec (IREQ, Varennes, Canada) for the thin foil preparation as well as Mr. Dave Shepard and Mr. Ilir A. Beta from Netzsch Instruments North America (LLC applications laboratory, Burlington, MA) for the DSC testing. Thanks are also expressed to King Fahd University of Petroleum and Minerals (KFUPM), Dhahran, Saudi Arabia for the scholarship awarded to Ahmad A. Sorour.

CHAPTER 5

Tribology of a Fe–Cr–B-Based Alloy Coating Fabricated by a Controlled Short-Circuit MIG Welding Process

[1]Ahmad A. Sorour[*], Richard R. Chromik[*] and Mathieu Brochu[*]

[*]Department of Mining and Materials Engineering, McGill University, 3610 University Street, Montreal, QC H3A 0C5, Canada

In chapter 4, the solidification and microstructure of the deposited Fe–Cr–B-based alloy by CSC-MIG were studied. In this chapter, hardness of the phases was measured by nanoindentation and that of the bulk weldment by Vicker microhardness. The relation of hardness and boride's fraction was established. Sliding and abrasive wear testings were performed to evaluate the tribology performance and study the wear behavior.

[1]Published: A.A. Sorour, R.R. Chromik and M.Brochu, Metallography, Microstructure, and Analysis, Vol.2, pp. 223–233, 2013

Abstract

The aim of this study was to study the microstructure and tribology of a Fe–Cr–B-based alloy coating deposited by a controlled short-circuit metal inert gas welding process onto a 1020 carbon steel substrate with varying input energies. Microstructure analysis showed that the as-deposited alloy consisted of $(Cr,Fe)_2B$ particles embedded in a BCC solid solution matrix composed of Fe, Cr, Mn and Si. The hardness of $(Cr,Fe)_2B$ particles was 24 GPa. When the input energy increased during welding process, the deposition volume and dilution ratio were increased. As a result, $(Cr,Fe)_2B$ particle volume fraction decreased from 44.6 to 37.2% and the bulk hardness decreased from 6.43 to 5.80 GPa. Dry sliding wear tests were carried out against a stainless steel counterface. The steady state coefficient of friction and the wear rate for the Fe–Cr–B-based alloy were independent of input energy. While the coefficient of friction for the Fe–Cr–B-based alloy was about 20% higher than for the 1030 carbon steel, the wear rate was about 90% lower. The dominant sliding wear mechanisms were adhesion and oxidation. Two-body abrasion wear test using alumina abrasives showed that the wear rate of the Fe–Cr–B-based alloy increased as the input energy increased and was about 90% lower than that of the 1030 carbon steel. The abrasive wear mechanism was microcutting.

Keywords

Fe–Cr–B alloy; Metal matrix composite; CSC-MIG welding; Nanoindentation; Electron microscopy

5.1 Introduction

Dynamic machine components, such as pistons, shafts, journal bearings, cutting tools, pump parts and aeronautical parts, need to be protected against wear. Wear protection can be provided by metal matrix composites (MMCs), which are multiphase materials composed of hard reinforcing particles embedded in a metallic matrix [96]. One of these systems is the Fe–Cr–B-based alloys that contain hard boride particles, namely $(Cr,Fe)_2B$, $(Cr,Fe)_xB$, Cr_2B, $Fe_{1.1}Cr_{0.9}B_{0.9}$, and/or $Cr_{1.65}Fe_{0.35}B_{0.96}$, dispersed in a Fe-based solid solution matrix [8–14,20–22,24,26,58]. This system has been shown to exhibit excellent resistance against sliding and abrasive wear [13,14]. The Fe–Cr–B-based alloys have commonly been applied as a coating using thermal spray processes, such as detonation gun [13,24] and high velocity oxygen fuel (HVOF) [9,14,20–22]. Plasma-transferred arc (PTA) welding process has also been successfully used to fabricate a coating that provides a stronger metallurgical bond between the coating and the substrate and exhibits higher wear resistance when compared to thermal spray processes [9,10,20].

Welding techniques, such as gas metal arc welding (GMAW), plasma arc welding (PAW) and shielded metal arc welding (SMAW), are commonly used for hard-facing to protect the surfaces from wear, corrosion and heat. The metal inert gas (MIG) process, known also as GMAW, is a welding process which uses an arc to melt a constantly fed electrode wire that is transferred to the substrate [36, pp.19–22]. The controlled short-circuit metal inert gas (CSC-MIG) welding process is an improved version of the MIG welding process. In CSC-MIG process, the position and speed of the electrode wire are accurately controlled and thus leads to higher efficiency in

material transfer, better stability and lower heat input [31]. The CSC-MIG welding process was successfully used to deposit the overlay WC/Ni-based wire, which has a Ni sheath filled with FeSiB powder and WC particles, as high quality continuous beads without splatter [71]. The Fe–Cr–B-based alloy, which exhibits high wear resistance, has never been deposited by the CSC-MIG welding process.

Wear resistance of multi-phase materials, such as Fe–Cr–B-based and WC-based, depends on their wear mechanism, which is different from that of single-phase materials [64, 97]. Axen and Jacobson [64] proposed two modes of abrasive wear for two-phase materials, namely, equal wear rates of phases (EW) and equal pressure on phases (EP). In the EW mode, both phases are worn at the same linear rate and it corresponds to the upper limit of wear resistance (ideal state). In the EP mode, the matrix is worn independently, while the reinforcing phase is removed discretely. Thus, the reinforcing phase contributes slightly to wear resistance and the EP mode corresponds to the lower limit of wear resistance. The wear resistance of composite materials should fall somewhere between these limits [64] depending on a reinforcing particles size, matrix hardness, abrasive grit size, and inter-phase bonding [96]. It has been found that the volume fraction, shape, size, and orientation of the hard boride particles affect the wear performance of the Fe–Cr–B alloy [8, 10, 20, 26]. Welding the alloy onto a substrate, such as carbon steel, would cause dilution that changes the composition, microstructure, mechanical properties and consequently wear performance.

The purpose of this work was to study the microstructure and tribology of the Fe–Cr–B-based alloy system deposited by the CSC-MIG welding with varying input

energies. Microstructure characterization was carried out to identify the phases and their distributions, size, shapes and volume fractions. Nanoindentation and microindentation techniques were used to measure the particles and the bulk hardness, respectively. Sliding wear and abrasive wear tests were carried out to study the friction and wear behavior in dry conditions. Post microstructural analysis was performed to investigate the sliding and abrasive wear mechanisms.

5.2 Experimental Procedures

5.2.1 Material

A commercial Fe–Cr–B-based alloy, designated as Armacor M, was selected for this research. It was received as a cored wire designed for twin wire arc spray (TWAS) process. The chemical composition of this alloy, as given by the manufacturer's data sheet, was 26.5–31.5% Cr, 3.4–4.2% B, 1.1–2.1% Si, and 1.1–2.2% Mn (all in wt.%) with the balance being Fe.

5.2.2 CSC-MIG Welding Process

Single bead and multi-pass coatings (adjacent parallel beads) were deposited onto plain carbon steel (AISI 1020) plates, $100 \times 40 \times 3$ mm^3 in dimensions, using the CSC-MIG welding system. This welding system was described in detail elsewhere [71]. The shielding gas was argon with a flow rate of 0.0189 m^3/s (40 cfm). Table 5.1 lists the CSC-MIG welding process parameters used to fabricate three specimens designated as M1, M2 and M3.

Table 5.1: The CSC-MIG welding process parameters

Specimen	M1	M2	M3
Input energy (J/mm)	78 ± 5	220 ± 5	450 ± 10
Arc current (A)	100	200	300
Arc time (s)	0.01	0.01	0.01
Short-circuit current (A)	75	150	200
Short-circuit time (s)	0.01	0.01	0.01
Wire feed speed (mm/s)	183	217	250

5.2.3 Phase and Microstructure Analysis

For cross-sectional analysis, the specimens were cut perpendicular to the welding direction. For surface analysis, the multi-pass deposition beads were ground from the top surface to create a flat surface. For microstructure examination, mechanical properties measurements and wear tests, the specimens were cut, mounted, and then prepared using standard metallographic techniques. They were ground progressively down to 800 grit using SiC papers followed by polishing using diamond solutions to 1 µm finish. After the final polishing with colloidal silica (0.05 µm), the specimens were cleaned in an ultrasonic bath filled with acetone for about 10 min to remove the residual debris and then dried in air.

Phase analysis was performed by x-ray diffraction (XRD) using Cu Kα (λ = 0.15406 nm) radiation. XRD scans were carried out under the operation conditions of 40 kV and 20 mA with a 2θ step size of 0.01 °/s and a dwell time per step of 1 s in the 2θ range of 30°–100°.

Microstructure and chemical analysis were carried out using a light microscope (LM), a field emission scanning electron microscope (FE-SEM), and energy dispersive spectroscopy (EDS). Secondary electron (SE) and back-scattered electron (BSE)

micrographs were acquired at 15 kV accelerating voltage. Post-microstructural analysis of the worn surfaces of both sliding and abrasive wear was also accomplished using the FE-SEM and EDS to investigate the wear mechanisms. Quantitative analysis of the size and morphology of the phases was performed using commercially available image analysis software. Twenty BSE micrographs of each specimen were employed to measure the volume fractions and aspect ratios of the phases. All average values in this research were compared by two-sided t student statistical tests using confidence interval of 99%.

5.2.4 Hardness and Elastic Modulus Measurements

Nanoindentation was used to measure the hardness H and reduced elastic modulus E_r of the phases within the specimens. The measurements were conducted at room temperature ($\sim$ 21 ℃) using a diamond Berkovich tip. The system is equipped with a piezoelectric scanner used to acquire topographical images similar to atomic force microscopy (AFM). The load-controlled indentation cycle was composed of loading for 5 s, holding at maximum load for 5 s and unloading for 5 s. For each phase, 20 indents were performed to obtain mean values and standard deviations. The H and E_r were calculated from the load-displacement curves using Oliver and Pharr method [98]. Because pile-up was observed for all indents, post scanning of each indent was performed to measure the increased contact depth which is used to recalculate the actual contact area and correct the hardness and reduced modulus accordingly, as described in Chapter 7.

Microindentation was used to measure the bulk hardness of the specimens using

the Vickers microhardness tester at room temperature ($\sim$ 21 ℃). The indents were performed on a polished surface under a load of 500 g (4.91 N) with 40 indents onto specimens of each welding condition in Table 5.1 to determine the mean value and standard deviation.

5.2.5 Tribology Tests

Tribological properties and the behavior were evaluated by dry sliding and abrasion wear tests. Dry sliding wear tests were conducted using a custom-built linear reciprocating tribometer (ball-on-flat configuration) [99] in ambient air at room temperature (22.6 ± 0.5℃) and humidity (19 ± 5% RH). The sliding wear tests were performed for two speciments of each welding condition in Table 5.1. Three tests were carried out on each specimen giving a total of six runs for each welding condition. The counterface was a full hard temper wear resistant stainless steel ball (type 440C) with a diameter of 12.7 mm and a hardness of 7.2 ± 0.2 GPa. The track length was 2 mm and a constant sliding speed of 3 mm/s was achieved for at least 95% of the track length. The total sliding distance was 20 m (5,000 cycles) and the reciprocating frequency was 0.632 cycle/s. The normal applied load was 85 g (0.834 N). The frictional force was recorded during the test to calculate the coefficient of friction (COF = frictional force/normal load) [2, pp.209]. Depth profiles of the wear tracks were measured (three measurements per track, one at the middle and the others between the middle and the ends) using a stylus profilometer. The wear volume was calculated by multiplying the average of the three measurements for the wear scar cross-sectional area by the track length (2 mm). Wear rates (in mm^3/Nm) of the specimen was calculated by:

$$\text{Wear rate} = \frac{\text{Wear volume (mm}^3\text{)}}{\text{Load (N)} \times \text{Sliding distance (m)}} \tag{5.1}$$

For comparison and reference purpose, similar wear testing condition was performed onto a medium carbon steel (AISI 1030) specimen. The hardness of this carbon steel was measured using the Vickers microhardness as 169 ± 3 HV (1.65 ± 0.03 GPa).

Two-body abrasion wear tests were conducted in ambient air at room temperature (20 ± 1 ℃) and humidity ($48 \pm 7\%$ RH) using a Loop Abrasion Tester designed for wear tests described in ASTM G174 standard [100] procedure (C). The specimen size of about $32 \times 8 \times 4$ mm was cut from the multi-pass weldment and ground from the top side of the tested surface down to a roughness less than 0.2 µm Ra. The abrasion wear test was repeated three times for each specimen. The normal load was 100 g (0.981 N) and the spindle speed was 100 rpm. The test duration was 75 belt passes with a belt length of 1,295 mm; thus, the total abrasion distance was 97.1 m. The abrasive used was a 30 µm aluminum oxide microfinishing tape. The wear scars were measured at the middle using a non-contact laser profilometer. The wear volume was calculated using geometry calculation as described in ASTM G174 [100]. Abrasion wear rate in (mm^3/m) was calculated by dividing the wear volume by the total abrasion distance (97.1 m). For comparison and reference purpose, same wear test condition was performed onto a medium carbon steel (AISI 1030) specimen of the same reference material described above for sliding wear testing. It should be noted that for all repeated measurements, the average and standard deviation were calculated, and the result was reported in this article as (average ± standard deviation).

5.3 Results and Discussion

5.3.1 Microstructure and Phase Analysis

Figure 5.1 shows cross-sectional light micrographs of the Fe–Cr–B alloy deposited using the CSC-MIG welding process with different heat inputs. Heat input (the amount of energy delivered per unit of length) is a function of voltage, current and welding velocity [35]. When the voltage and current increased (Table 5.1) during the welding process, the heat input increased which caused higher melting masses of the electrode tip and substrate leading to higher deposition volume and weld dilution, respectively. While porosity was observed in M1 specimen, no porosity was observed at higher heat input within M2 and M3 specimens. There was no evidence of weld dilution in M1 specimen. However, the dilution for M2 specimen was 3 ± 2.4 vol.% and that of M3 specimen was 19 ± 6.0 vol.%, as measured using image analysis based on four micrographs for each welding condition.

Figure 5.2 shows SEM (BSE) micrographs of M1, M2 and M3 specimens. The as-deposited alloy consisted of two distinct phases, dark-contrast primary particles (β) and secondary particles (β') impeded in a light-contrast matrix. No cavities or cracks presented at the interface between the particles and the matrix. The distribution of the β particles was uniform throughout the deposition (Figure 5.1), while the β' particles distribution between the β particles were not (Figure 5.2). As the heat input increases, the size and the distance between the β and β' particles slightly increased. Table 5.2 lists the quantitative data analysis based on these SEM (BSE) micrographs. The particles' (β and β') volume fractions for M1 and M2 specimens were equivalent

but were lower for M3 specimen. However, the aspect ratios of β' particles of the specimens were equivalent.

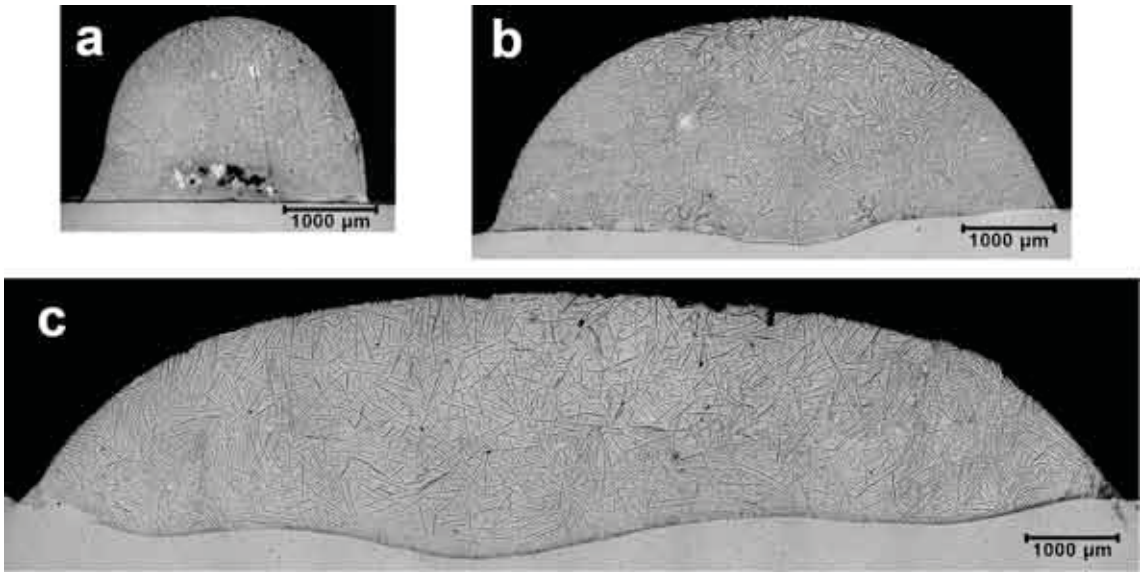

Figure 5.1: Cross-sectional light micrographs of the Fe–Cr–B-based alloy deposited by the CSC-MIG. (a) M1, (b) M2, and (c) M3

Table 5.2: Quantitative data analysis for M1, M2 and M3 specimens

Specimen	Volume fraction (%)		Aspect ratio of the β' particles
	Particles (β and β')	Matrix	
M1	44.6 ± 3.9	55.5 ± 3.9	10.2 ± 3.3
M2	44.2 ± 2.7	55.8 ± 2.8	10.1 ± 4.2
M3	37.2 ± 2.6	62.9 ± 2.7	8.2 ± 3.7

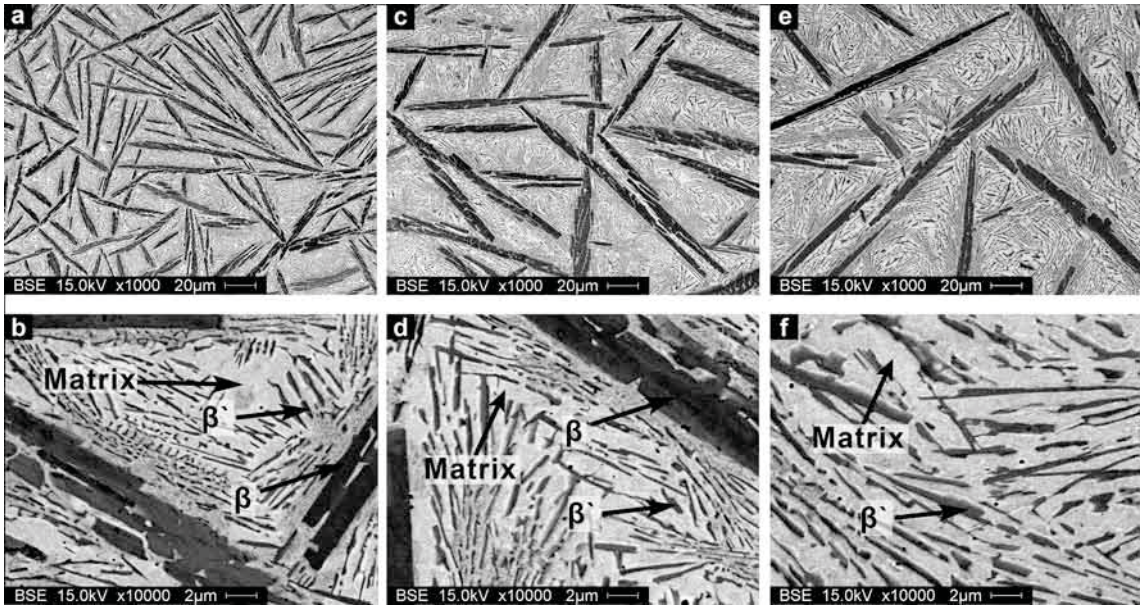

Figure 5.2: SEM (BSE) micrographs of (a, b) M1, (c, d) M2, and (e, f) M3 specimens

The XRD results (Figure 5.3) for the three deposited specimens show one series of peaks that correspond to a body centered cubic (BCC) α-Fe phase (JCPDS#006-0696). The second set corresponds to the orthorhombic structure boride phases, namely $Fe_{1.1}Cr_{0.9}B_{0.9}$ (JCPDS#072-1073) and Cr_2B (JCPDS#003-4131). EDS analysis (Figure 5.4a) shows that the β and β' particles (in Figure 5.2) were rich in B, Cr and Fe, while the matrix was rich in Fe, Cr, Mn and Si (Figure 5.4b). It should be noted that the EDS spectrums of the particles (Figure 5.4a) were similar for all three specimens (M1, M2, and M3) and within the same specimen as well. Likewise, the EDS spectrums of the matrix (Figure 5.4b) were also similar for all specimens and within the same deposition. It is hence concluded that the dark-contrast particles (β and β') correspond to boride of Cr and Fe phase of the type M_2B and the light-contrast matrix corresponds to a BCC solid solution of Fe, Cr, Mn and Si. For

similar Fe–Cr–B-based alloys, it has been reported the boride phase particles as $(Cr,Fe)_2B$ [11, 12]. The formation of the BCC solid solution phase is also consistent with the reported results [8, 9, 12, 14, 22, 24].

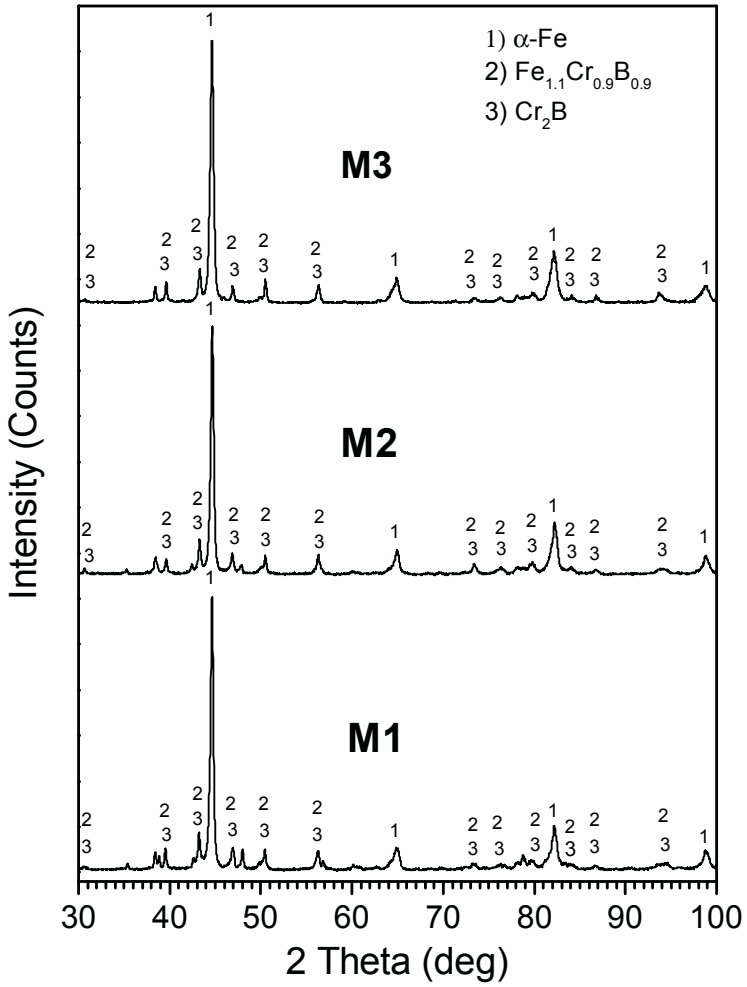

Figure 5.3: XRD results of the deposited alloy specimens

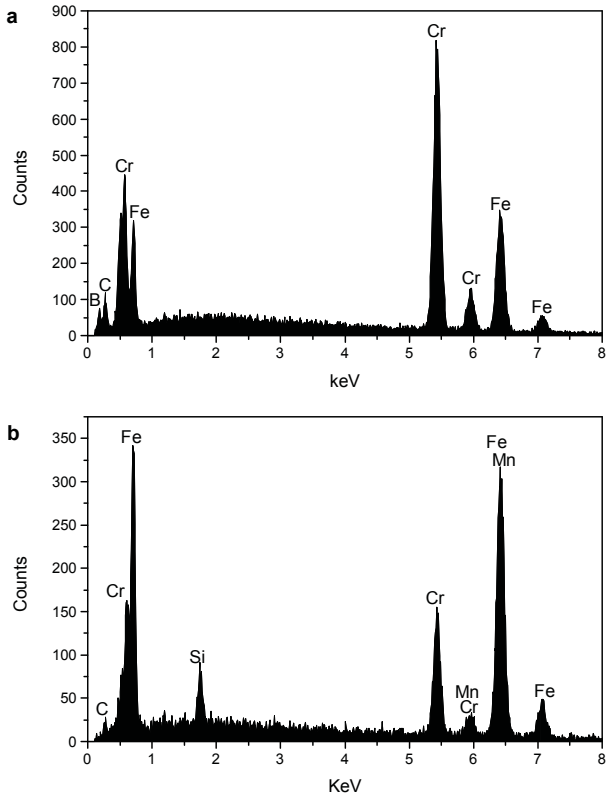

Figure 5.4: Typical EDS analysis of (a) the particles and (b) the matrix for M2 specimen

Nanoindentation was used to measure the hardness and the reduced modulus of both the β particles as well as the mixed region, which involves the β' particles and the matrix. The nanoindentation tests were conducted at the middle regions of the specimens' cross-sections (Figure 5.1). While the mechanical properties of the hard particle can be affected by the matrix properties, simulations by Yan et al. [101, 102] showed that the Oliver–Pharr method [98] can still be applied to measure the elastic modulus and hardness of the particle with sufficient accuracy if the indentation depth is within the particle-dominated depth. For our experiments, the particle-dominated

indentation depth was estimated as explained in [102] and the indentation depth into the β particles was found sufficiently shallow to satisfy the condition set out by Yan et al. [101] for use of the Oliver–Pharr method [98] on particles in composites. Table 5.3 lists the hardness and the reduced modulus of the $(Cr,Fe)_2B$ β particles and the mixed region for M1, M2 and M3 specimens. The hardness and the reduced modulus were each similar among the specimens. The hardness of the $(Cr,Fe)_2B$ particles (β) exhibited a high value of about 24 GPa which was similar to the hardness of the boride layer containing Fe_2B, FeB, Cr_2B, CrB and MnB that can reach up to 2,500 HV ($\sim$ 24.5 GPa) as reported by Ozbek et al. [55]. The hardness of the mixed region was in the range of 8–10 GPa. Figure 5.5 shows the typical load vs. depth curves for the indentation onto the particle and the mixed phase.

The bulk hardness was measured using the Vickers microhardness under 500 g (4.91 N) load and the results are presented in Table 5.3. While the bulk hardness of M1 and M2 specimens were similar, that of M3 specimen was statistically lower. The bulk hardness of M3 specimen was decreased because of the weld dilution that reduced the B concentration and hence reduced the boride particles volume fraction (Table 5.2). This finding is consistent with previous studies [11, 12, 65], which have shown that as the B content increases, the fraction of the hard boride phase increases and consequently the bulk hardness increases. It should be noted that the hardness of the boride particles did not change with the heat input variation.

Table 5.3: Nanoindentation and Vickers microhardness results for M1, M2 and M3 specimens

Specimen	Nanoindentation				Vickers microhardness	
	β particles		Mixed phase			
	H (GPa)	E_r (GPa)	H (GPa)	E_r (GPa)	(HV)	(GPa)
M1	23.6 ± 1.5	300 ± 24	8.1 ± 1.4	224 ± 15	655 ± 41	6.43 ± 0.41
M2	24.1 ± 1.0	318 ± 14	8.5 ± 1.6	226 ± 13	650 ± 58	6.37 ± 0.57
M3	24.5 ± 0.7	318 ± 10	9.8 ± 2.7	239 ± 19	592 ± 40	5.80 ± 0.40

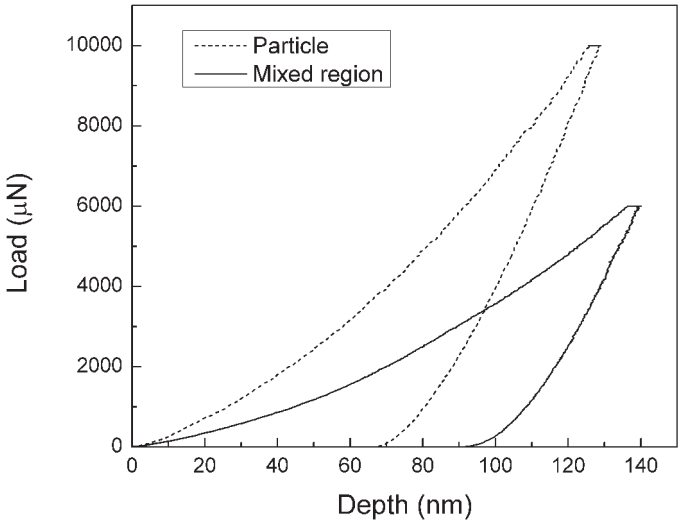

Figure 5.5: Typical load vs. depth curves for the indentation onto the particle and the mixed region for M2 specimen

5.3.2 Sliding Wear

Dry sliding wear test of the Fe–Cr–B-based alloy deposited using the CSC-MIG welding and the 1030 carbon steel was carried out against stainless steel counterface for 20 m sliding distance. Figure 5.6 shows the COF evolution as a function of cycle number and sliding time for M1, M2 and M3 specimens. The COF can be divided into two distinct regions as "running in" and "steady state". The "running in" period represents the first 200 cycles (315 s), as shown in small plot in Figure 5.6, in which

the COF started at about 0.1 and increased progressively until it became stable. The steady state COF was estimated by calculating the average and standard deviation of all the data points (Figure 5.6) for the repeated tests for each specimen after excluding the first 200 cycles ("running in" period) and the results are presented in Table 5.4. The steady state COFs for M1, M2 and M3 specimens were equivalent and were about 20% higher than the carbon steel one.

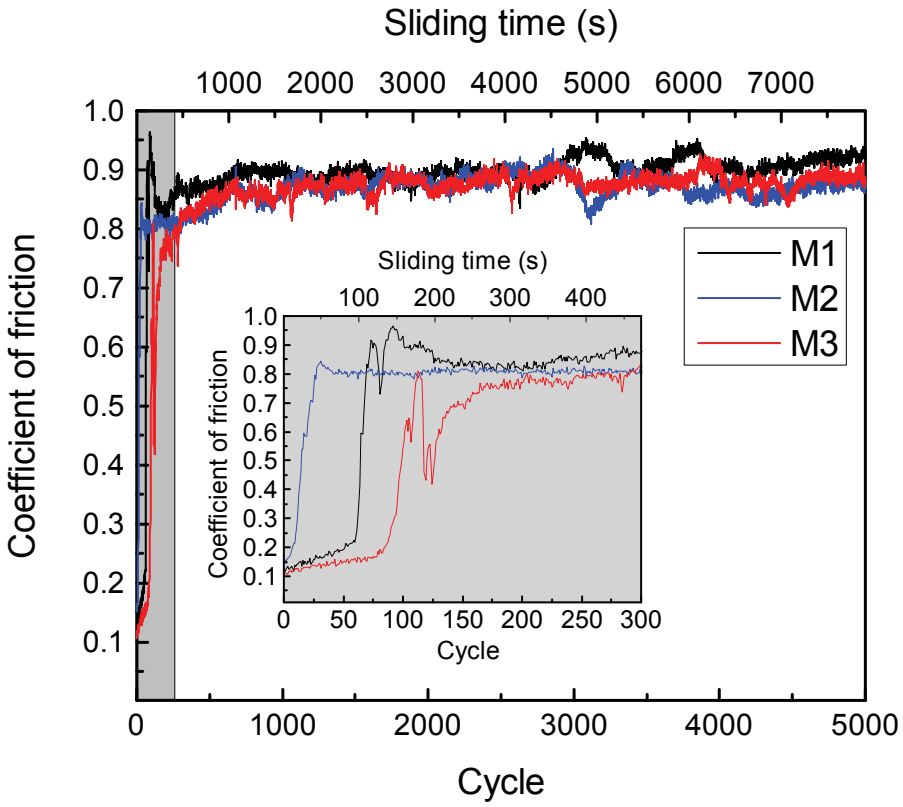

Figure 5.6: The coefficient of friction vs. cycle number and sliding time for the specimens when slid against stainless steel up to 20 m

Table 5.4: Dry sliding wear results of the specimens slid against stainless steel counterface for 20 m sliding distance

Specimen	Steady state COF	Specimen wear volume ($\times 10^{-5}$ mm^3)	Specimen wear rate ($\times 10^{-6}$ mm^3/Nm)	Counterface wear rate ($\times 10^{-6}$ mm^3/Nm)
M1	0.887 ± 0.033	2.92 ± 0.44	1.82 ± 0.28	4.1 ± 0.5
		3.27 ± 0.41	2.04 ± 0.25	53.1 ± 18.8
M2	0.889 ± 0.056	3.51 ± 0.73	2.19 ± 0.46	46.4 ± 17.2
M3	0.885 ± 0.027	3.57 ± 0.66	2.23 ± 0.41	15.9 ± 5.4
1030 carbon steel	0.739 ± 0.044	34.80 ± 5.01	22.03 ± 4.43	13.7 ± 13.0

The wear volumes of M1, M2, M3 and 1030 carbon steel specimens are listed in Table 5.4. The wear volumes of the M1, M2 and M3 specimens were equivalent. Similarly, the wear rates were equivalent, as shown in Table 5.4. The two distinct values of wear volume and wear rate or M1 specimen correspond to data from test-to-test variations that were not correlated to difference between the two specimens of this weld condition. That is, each reported average has data from each of the two weld specimens for M1. While the welding heat input variation affected the microstructure and the hardness, it was not significant enough to change the sliding wear resistance. The wear volumes of the Fe–Cr–B-based alloy were about 90% lower than that of the carbon steel.

The stainless steel counterface was also worn during sliding, as shown in Figure 5.7, and the wear rates of the counterface were presented in Table 5.4. For M2 and M3 specimens, the counterface wear rates were similar from test-to-test and a single average counterface wear rate was calculated for each specimen. However, the counterface wear rate for M1 specimens did not converge to a single average value and instead these specimens exhibited two distinct counterface wear rates. One wear rate

($53.1 \pm 18.8 \times 10^{-6}$ mm^3/Nm) was similar to that measured for M2 specimen, but the other one was significantly lower ($4.1 \pm 0.5 \times 10^{-6}$ mm^3/Nm) and more closer to the counterface wear rate measured for M3 specimen. As the boride particles volume fraction (Table 5.2) and bulk hardness (Table 5.3) of M3 specimen were lower than that of M1 and M2 specimens, it would be expected that the M1 and M2 specimens abrade the counterface at a similar rate, while M3 specimen would abrade it at lower rate. Thus, all of the measurements of the counterface wear rate agree with the hardness and changes in boride volume fraction except for the set of measurements for M1 specimen where the counterface wear rate was low. We hypothesize that this set of data may reflect some microstructural variation in M1 specimen that we have not rigorously studied yet. It is worth mentioning that M1 specimens were the most difficult to fabricate and while care was taken to prepare the specimens for three welding conditions used for this study in the same manner, some small differences in the microstructure, especially the boride distribution at the location where the wear test was conducted could explain these differences.

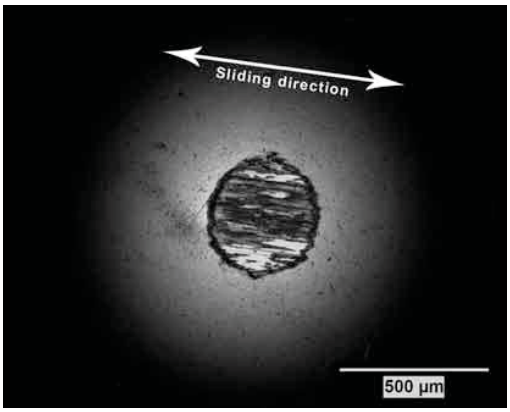

Figure 5.7: Light micrograph of the wear scar on the stainless steel counterface slid against M2 specimen for 20 m

The sliding wear mechanism of the Fe–Cr–B-based alloy was investigated by post microstructure analysis, which showed similar characteristics of the worn surfaces for M1, M2 and M3 specimens. Figure 5.8 shows typical SE and BSE micrographs of the worn surface of M2 specimen after 20 m sliding distance. The entire worn surface was damaged. The damage included (Figure 5.9) matrix removal, matrix oxidation and boride particles (β) microcracking. EDS analysis (Figure 5.9g) indicated that the matrix oxidation is oxides of Fe, Cr, Mn and Si. It was observed that the oxides existed mainly in the regions where the matrix was removed. Moreover, Figure 5.8 shows a build-up oxidized Fe-based material that could be a transferred material from the stainless steel counterpart. In addition, very few fine grooves aligned with the sliding direction were observed (Figure 5.8) due to the presence of hard particles (oxide debris and broken borides) that moved over the surface and scratched the surface.

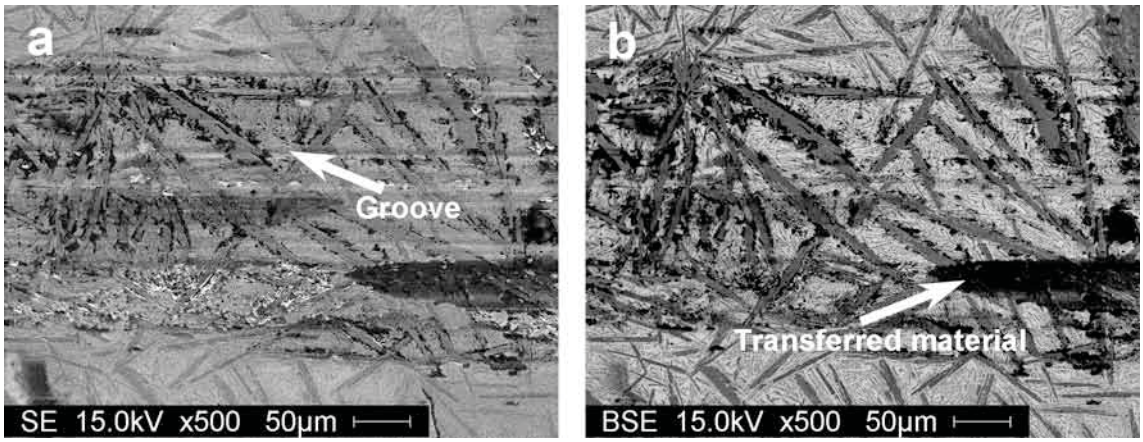

Figure 5.8: (a) SE and (b) BSE micrographs of the wear track of M2 specimen after the wear test

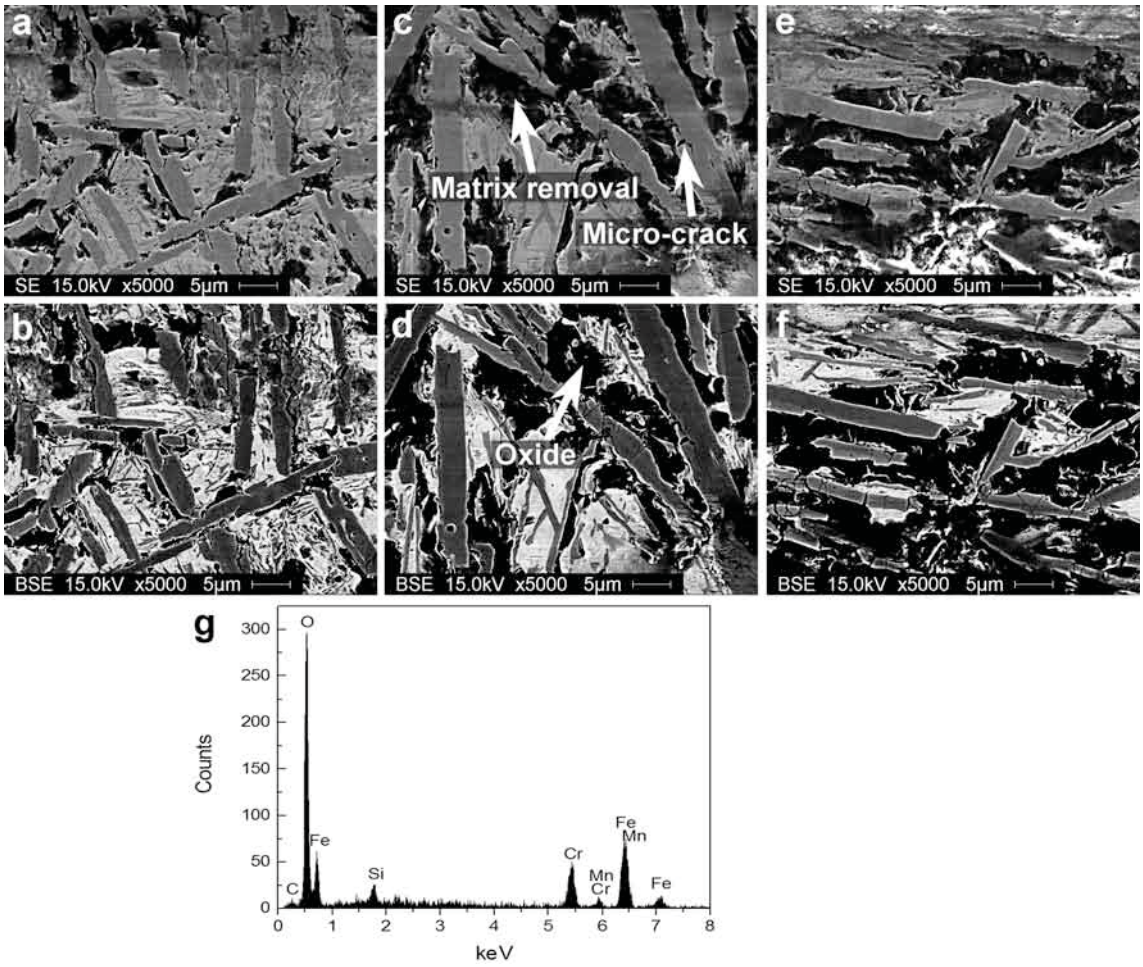

Figure 5.9: SE and BSE micrographs of the wear track after sliding wear test for 20 m sliding distance for the specimens (a, b) M1, (c, d) M2, and (e, f) M3 with (g) a corresponding EDS analysis of the black regions in (d)

The matrix elements oxidized due to the high temperatures at asperities (flash temperature), which could reach up to 1,000 ℃ depending on the applied load, COF and sliding speed [103]. The oxide islands continued to grow and then were detached and pulled out by the adhesion and friction force (shear stress), which also caused material transfer from the softer surface (counterface) to the harder [103]. When the oxidized matrix was removed, the boride particles in contact were no longer supported and thus they were cracked, broken and then removed. It can be concluded that the main wear mechanisms of the Fe–Cr–B alloy, fabricated by the CSC-MIG welding, that slid against stainless steel counterpart at room temperature were adhesive wear and tribo-oxidation (of the matrix) mechanisms, which occurred simultaneously. Similar wear mechanisms (adhesion and mild oxidation) were observed for dry sliding wear of the Fe–Cr–B-based alloy fabricated by the spark plasma sintering (SPS) process with similar test conditions (Chapter 7).

5.3.3 Abrasive Wear

Abrasive wear resistance and behavior were investigated by means of abrasive tester using alumina abrasives (with 30 µm particle size) for the specimens M2, M3 and 1030 carbon steel. The standard coupon size for abrasive wear test could not be fabricated using the M1 condition (Table 5.1) as the deposition volume was low and the multi-pass welding was not successful. Thus, M1 specimen was not tested. Table 5.5 lists the wear volume of the specimens M2, M3 and 1030 carbon steel subjected to same conditions for the purpose of comparison. The wear volume of M2 specimen was lower than that of M3 specimen by about 29%. The wear volumes

of M2 and M3 specimens were lower than that of the carbon steel by about 91 and 87%, respectively. Abrasive wear rates of these specimens, as shown in Table 5.5, followed same trend. The specimen M2 exhibited higher wear resistance because its bulk hardness was higher (Table 5.3) and therefore the penetration depth of the abrasive particles into the specimen surface was reduced [104–107]. Son et al. [11] and Yi et al. [65] also showed that the abrasive wear resistance increases when the bulk hardness and boride fraction increases. The results were also in agreement with previous studies [7, 108] that showed the increasing of wear resistance with the increasing volume fraction of the SiC and Al_2O_3 reinforcements. The hardness of the Fe–Cr–B alloy was much higher than that of carbon steel and thus the penetration depth was lower and the wear resistance was higher.

Table 5.5: Abrasive wear test results for the specimens M2, M3 and 1030 carbon steel

Specimen	Wear volume (mm^3)	Wear rate ($\times 10^{-3}$ mm^3/Nm)
M2	0.16 ± 0.01	1.63
M3	0.22 ± 0.01	2.29
1030 carbon steel	1.76 ± 0.03	18.20

Abrasive wear mechanism was also investigated by post microstructural analysis of the worn surfaces. SE and BSE micrographs of the wear tracks of M2 and M3 specimens (Figure 5.10) show continuous abrasive grooves on the surface. For both specimens (M2 and M3), the grooves width were about 1–3 µm which was much smaller than the abrasive particles size (30 µm), indicating that the penetration depth of the abrasive was low. While no particle removal (pulled out) was observed, some microcracks in the primary boride particles (β) were detected, as shown in

Figure 5.10. Zum Gahr [60] showed that the abrasive wear occurs in four basic modes, which are microploughing, microcutting, microfatigue and microcracking. While microploughing and microcutting are dominant on ductile materials, microcracking is more substantial on brittle materials [63]. The formation of the continuous grooves along minor microcracks within the boride particle (Figure 5.10) implies that the predominant wear mechanism was abrasion in the form of microcutting mode.

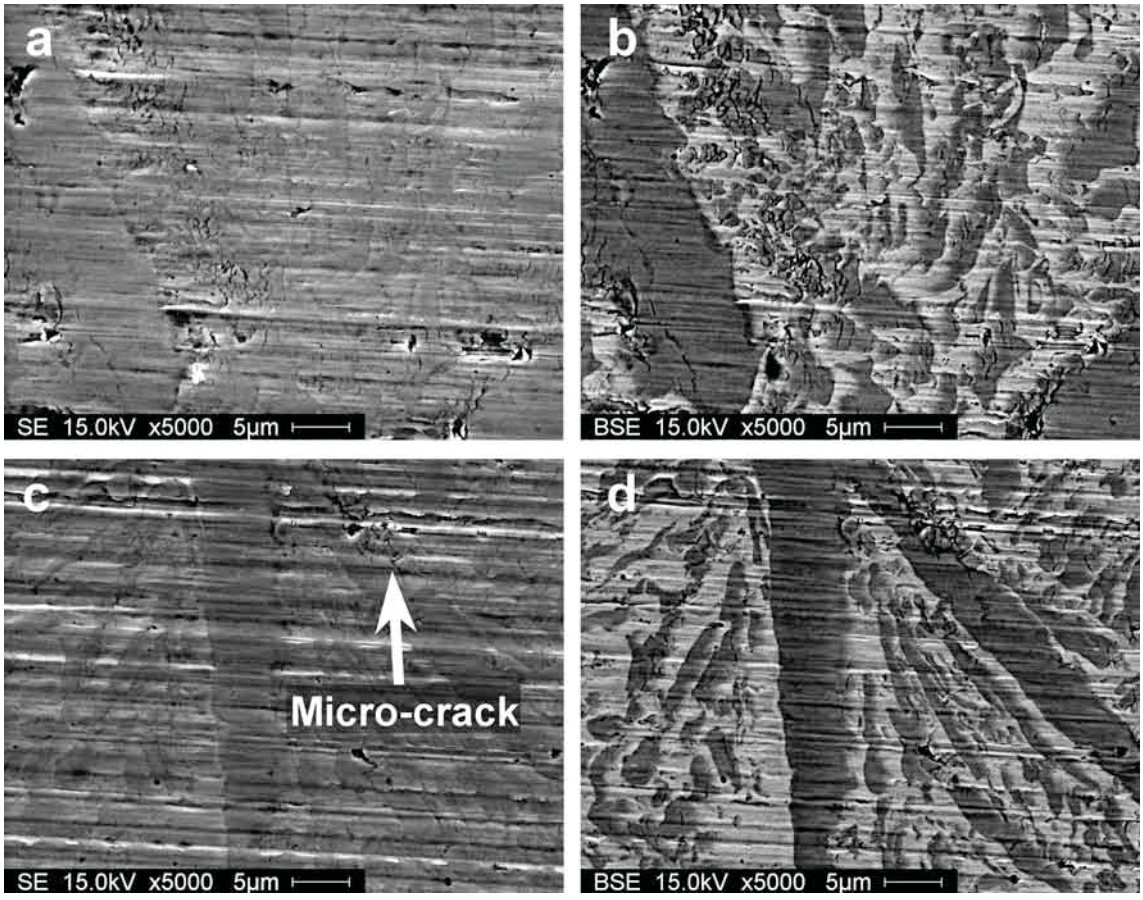

Figure 5.10: SE and BSE micrographs of the worn surfaces after abrasive wear test for the specimens (a, b) M2 and (c, d) M3

Currently, the Fe–Cr–B-based alloy fabricated by the CSC-MIG welding process was tested at low loads, 0.834 N for sliding wear and 0.981 N for abrasive wear. The alloy showed high wear resistance as compared to the 1030 carbon steel. To understand better the wear performance for more severe applications, sliding and abrasive wear tests at higher loads need to be performed. Nevertheless, this investigation provided an indication of the potential for the CSC-MIG process to produce a high wear resistance Fe–Cr–B-based alloy.

5.4 Conclusion

The main questions addressed in this study concerned the investigation of microstrcture and tribological behavior of the Fe–Cr–B-based alloy fabricated by the CSC-MIG welding process at varying conditions. The following conclusions can be drawn.

1. At low heat input, there was some porosity in the weldment and evidence that the bonding to the substrate was not complete. With higher heat inputs, the alloy was deposited and bonded metallurgically onto the 1020 carbon steel substrate with negligible cracks and porosity.

2. The as deposited coating consists of the hard $(Cr,Fe)_2B$ primary and secondary particles embedded in the Fe-based BCC solid solution matrix composed of Fe, Cr, Mn and Si. The hardness and reduced modulus of the primary boride particles are about 24 and 300 GPa, respectively.

3. Welding parameters have affected the microstructure characteristics and the mechanical properties of this alloy. When the heat input increases because of

the current and voltage increasing, the deposition volume and dilution increase. As a result, the $(Cr,Fe)_2B$ particle fraction decreases and thus the bulk hardness decreased.

4. Dry sliding wear test against stainless steel counterface shows that the COF and the wear rate of the deposited alloy were equivalent as a function of input energy. The independence of wear resistance on welding parameters variation can be considered as a good advantage for this welding process. The COF for the Fe–Cr–B-based alloy was about 20% higher than that of the 1030 carbon steel, whereas the wear rate was about 90% lower. The dominant sliding wear mechanisms were adhesion and oxidation.

5. Abrasive wear test using alumina abrasives revealed that the wear rate increased as the input energy increased. The wear rate of the Fe–Cr–B-based alloy was about 90% lower than that of the 1030 carbon steel. The abrasive wear mechanism was microcutting.

Acknowledgments

We would like to thank Dr. S. V. Descartes for commenting on the work in draft. Thanks are also expressed to King Fahd University of Petroleum and Minerals (KFUPM), Dhahran, Saudi Arabia for the scholarship awarded to A.A. Sorour. We also gratefully acknowledge the assistance of the technical staff at Bud Labs (Rochester, NY, USA) for their assistance with the abrasive wear testing.

CHAPTER 6

Microstructure and Densification of Gas Atomized Fe–Cr–B-Based Alloy Powder Consolidated by Spark Plasma Sintering

[1]Ahmad A. Sorour[*], Richard R. Chromik[*] and Mathieu Brochu[*]

[*]Department of Mining and Materials Engineering, McGill University, 3610 University Street, Montreal, QC H3A 0C5, Canada

As the SPS process has been shown to offer improved properties and full consolidation of difficult-to-sinter-powders for shorter holding time compared to other methods, the Fe–Cr–B-based powder was sintered by SPS, and its microstructure and densification were investigated.

[1]Accepted: A.A. Sorour, R.R. Chromik, M. Brochu, Powder Metallurgy, 2014

Abstract

This paper is a study of microstructure and densification of a gas atomized Fe–45Cr–5.9B–2Si–0.1C (wt.%) alloy powder consolidated using the spark plasma sintering (SPS) process. The results showed that the fabricated alloy contained about 65 wt.% $(Cr,Fe)_2B$ plates and 1 wt.% $(Cr,Fe)_7C_3$ precipitates dispersed in a 34 wt.% body-centered cubic Fe-based solid solution matrix containing Cr and Si. The powder was fully densified with solid-state sintering for a short period of time (<10 min). After sintering, the phases did not transform, and the fraction, shape and aspect ratio of $(Cr,Fe)_2B$ did not change. In addition, we adapted the known SPS constitutive densification model from Olevsky and Froyen [43] to include a microstructure factor describing deformation of a metal matrix composite powder. The model was in reasonable agreement with the experimental results.

Keywords

Fe–Cr–B alloy; Metal matrix composite; SPS; Electron microscopy; Densification Modeling

6.1 Introduction

Fe–Cr–B-based alloys can be a good replacement candidate for currently used materials in engineering parts subjected to wear and erosion because of their high hardness, wear resistance and corrosion resistance [8, 11, 14–16, 69, 70]. These alloys are in-situ metal matrix composites (MMC); the reinforcing $(Cr,Fe)_2B$ boride solidifies as a primary solid phase within an Fe-based solid solution matrix during fabrication from liquid metal [8, 11–13, 21–23, 27]. These powder alloys were previously processed using powder-injection molding (PIM) [11, 15, 27, 28], hot-isostatic pressing (HIP) [29] and supersolidus liquid-phase sintering (SLPS) [29] routes.

Table 6.1 presents a summary of the consolidation data obtained in the literature for the PIM and SLPS routes. While the Fe–17Cr–3.4B–1.6Si–0.16C and Fe–43Cr–5.6B–1.8Si–0.17C (wt.%) alloys contained $(Cr,Fe)_2B$ and α-Fe-based matrix, the Fe–30Cr–17Ni–10Co–4Mo–4B–2.5Cu–1.5Si (wt.%) alloy consisted of $(Cr,Fe)_2B$ and γ-Fe-based matrix. The Fe–12Cr–3.5B–4Ni–3.3Mo–2Si–2C–0.2Mn–1.2Cu (wt.%) alloy contained $(Cr,Fe)_2B$, Cr_7C_3, Mo_3B_2 and $Fe_3(C,B)$ dispersed in γ-Fe-based matrix. The phases were independent of the sintering temperature, time and whether liquid phase formed (liquid-state) during sintering or not (solid-state). Full densification was reached when liquid-state sintering was used, while solid-state sintering yielded samples with the remaining porosity (>2.1 vol.%). As the sintering temperature increased, the porosity decreased, while the size of $(Cr,Fe)_2B$ and hardness increased [11]. However, for fully dense samples, the $(Cr,Fe)_2B$ fraction and hardness decreased as the sintering temperature increased [27].

Table 6.1: Literature results for sintering of Fe–Cr–B-based alloys

Alloy composition (wt.%)	Sintering process	Sintering temp.(℃)	Sintering time(min)	Sintering mechanism	Porosity (vol.%)	Ref.
Fe–17Cr–3.4B–1.6Si–0.16C	PIM	1,150	60	solid	2.1	[27]
	PIM	1,200	60	liquid	0.1	[27]
Fe–43Cr–5.6B–1.8Si–0.17C	PIM	1,150	30	solid	2.9	[11]
	PIM	1,250	30	liquid	0.01	[11]
Fe–30Cr–17Ni–10Co–4Mo–	PIM	1,100	30	solid	4.3	[11]
4B–2.5Cu–1.5Si	PIM	1,200	30	liquid	0.01	[11]
Fe–12Cr–3.5B–4Ni–3.3Mo–	SLPS	1,150	10	liquid	0.4	[29]
2Si–2C–0.2Mn–1.2Cu						

As presented, Fe–Cr–B-based alloys are hard to sinter. It has been shown that solid-state sintering can be facilitated through the imposition of an electric current through the powder bed during sintering, a process known as spark plasma sintering (SPS) [32]. The SPS process has been shown to sinter the Fe-based alloys [109–112]. The SPS offers many advantages over the conventional sintering processes, such as lower sintering temperature, shorter sintering time, higher heating rate, which minimize grain growth and lead to improved properties of the sintered materials [32, 33].

The primary aim of this study was to investigate the microstructure and densification development of a gas atomized Fe–Cr–B-based alloy powder sintered by the SPS process. The solidification behavior of the starting powder was studied using thermodynamic calculations and differential scanning calorimeter (DSC) analysis. Microstructural analysis was carried out using X-ray diffraction (XRD), emission scanning electron microscopy (FE-SEM), energy dispersive spectroscopy (EDS) and quantification image analysis. A densification model of this alloy during SPS was also adapted for this powder microstructure and experimentally validated.

6.2 Experimental Procedures

A Fe–Cr–B-based alloy powder, commercially known as Armacor M, was used for this study. The powder was produced by high-pressure argon gas-atomization process. Table 6.2 presents the chemical composition of this alloy, as indicated on the manufacturer's data sheet.

Table 6.2: Chemical composition of the starting Fe–Cr–B-based alloy powder

Element	Fe	Cr	B	Si	C	S
wt.%	Bal.	43.0–46.0	5.6–6.2	1.8–2.3	0.17 max.	0.02 max.
at.%	Bal.	35.8–37.4	22.4–24.2	2.8–3.5	0.6 max.	0.03 max.

The differential scanning calorimeter (DSC) analysis of the starting powder was performed using a Netzsch DSC 404 F1 Pegasus instrument. The powder and the sapphire standard were placed in alumina crucibles and then heated at 20 K/min under argon gas.

To measure the particle size distribution of the powder, 10 micrographs (50X magnification) of the powder were acquiring by a Nickon Epiphot 200 light microscope. The size of 220 powder particles was measured using a Clemex Vision Professional image analysis software.

The starting powder was consolidated using the Thermal Technology Ltd 10-3 SPS system. About 7 g of the powder was pressed in a graphite die under 6.8×10^{-2} Torr vacuum. The sintering process involved heating to 1,150 ℃ at a 200 ℃/min, while the pressure was simultaneously ramped to 50 MPa. A soaking time of 10 min was used. Temperature, pressure and displacement were monitored during the process.

The relative densification occurring during sintering was calculated based on the

displacement of the actuator. The sintered specimens had a disc shape with 20 mm diameter and 3 mm thickness. Density of the sintered specimen was measured using the Archimedes's principle, according to ASTM B962 Standard. The relative density was calculated considering the theoretical density of the alloy as 7.13 g/cm^3 [9].

To characterize the powder cross-section, the powder was hot mounted in conductive graphite filled polymer resin. For the SPS specimen analysis, the specimen was cut using a wafering diamond blade and also hot mounted with the same procedure. The mounted powder and specimen were ground and polished using standard metallography procedures. Final polishing was achieved using 0.05 µm colloidal silica. The polished specimens were cleaned in an ultrasonic bath with acetone for 10 min.

Microstructural analysis was carried out with a Hitachi SU-8000 and Phillips XL 30 field emission scanning electron microscopes (FE-SEM) to acquire secondary electron (SE) and backscattered electron (BSE) micrographs. An Oxford XMax energy dispersive spectrometer (EDS) was used for qualitative elemental analysis. The volume fraction and aspect ratio of the phases were measured by image analysis of three BSE micrographs (10,000x magnification) of each polished specimen. All average values were compared using two-sided Student t tests with a confidence interval of 99%. To investigate the shape of the boride particles, the specimen was deeply etched in a solution composed of one part HCL, one part HNO_3 and one part H_2O for 20 min, followed by imaging.

X-ray diffraction (XRD) analysis was performed with a Philips PW1070 diffractometer employing Cu Kα ($\lambda = 0.15406$ nm) radiation to identify the phases and measure their lattice parameters. XRD scans were made under the operation condi-

tions of 40 kV and 20 mA with a scan rate of 0.02°/s from 30° to 100°. The lattice parameters were calculated using W powder as a standard for peak position correction. The refinement of the patterns was carried out using the XLAT software [72].

6.3 Results and Discussion

6.3.1 Characterization of the Powder

Microstructure Analysis

Figure 6.1a shows SE micrograph of the starting Fe–Cr–B-based alloy powder. The powder has a spherical shape, which is typical of the gas-atomization process. The size distribution of these powder, as measured by image analysis, is presented in Figure 6.1b. The mean diameter of the powder was 118 ± 34 µm.

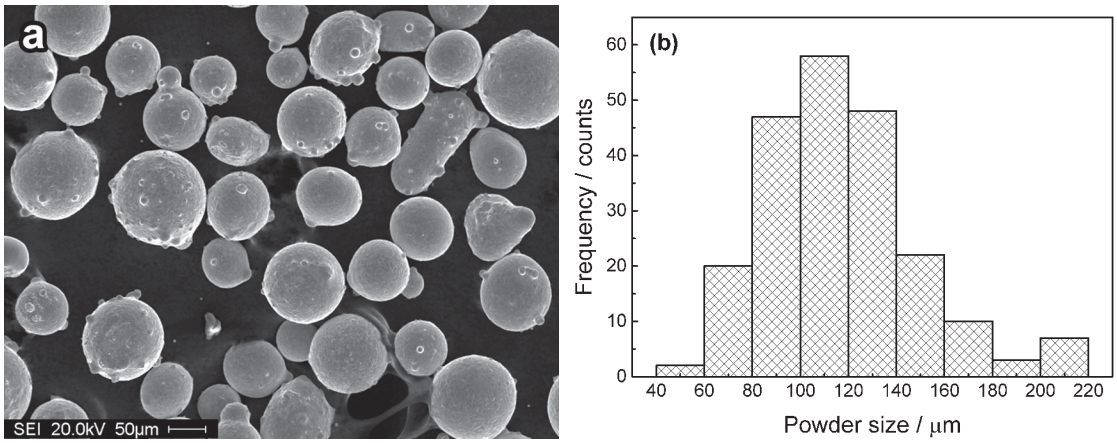

Figure 6.1: (a) SE micrographs and (b) particle size distribution of the starting Fe–Cr–B-based alloy powder fabricated by the gas-atomization process

Figures 6.2 a and b show the BSE micrographs of the polished cross-sectional

powder. It consisted of dark-contrast particles and a light-contrast matrix. EDS analysis showed that the particles were rich in B, Cr and Fe while the matrix was rich in Fe, Cr and Si. Table 6.3 presents the measured volume fractions of the particles and matrix and the aspect ratio of the particles for the starting powder by image analysis of the BSE micrographs.

Table 6.3: Volume fractions of the particles and matrix for the starting powder, sintered specimen and the modeling alloy as well as the measured aspect ratios of the particles

	Volume fraction (vol.%)		Aspect ratio
	Particles	Matrix	of the particles
Gas atomized powder[1]	65.7 ± 1.0	34.3 ± 1.0	6.28 ± 1.30
SPS bulk[1]	66.0 ± 1.1	34.0 ± 1.1	5.77 ± 1.40
Modeled alloy[2]	67.3	32.7	-

[1] Measured by image analysis
[2] Calculated by thermodynamic modeling

Figure 6.3a shows the XRD result for the starting powder. The identified phases were body-centered cubic (BCC) α-Fe (JCPDS#006-0696) [77] and orthorhombic $(Cr,Fe)_2B$ (JCPDS#072-1073) [46]. Therefore, the light-contrast matrix (Figure 6.2b) corresponds to the BCC Fe-based solid solution containing Cr and Si, and the dark-contrast particles correspond to the orthorhombic $(Cr,Fe)_2B$ phase.

Table 6.4 presents the measured lattice parameters of these phases and reported values from the literature. The measured and reported lattice parameters of $(Cr,Fe)_2B$ were similar. The measured lattice parameter of the α-Fe phase for the powder (2.861 ± 0.001 Å) was slightly lower than the one reported for pure α-Fe (2.866 Å).

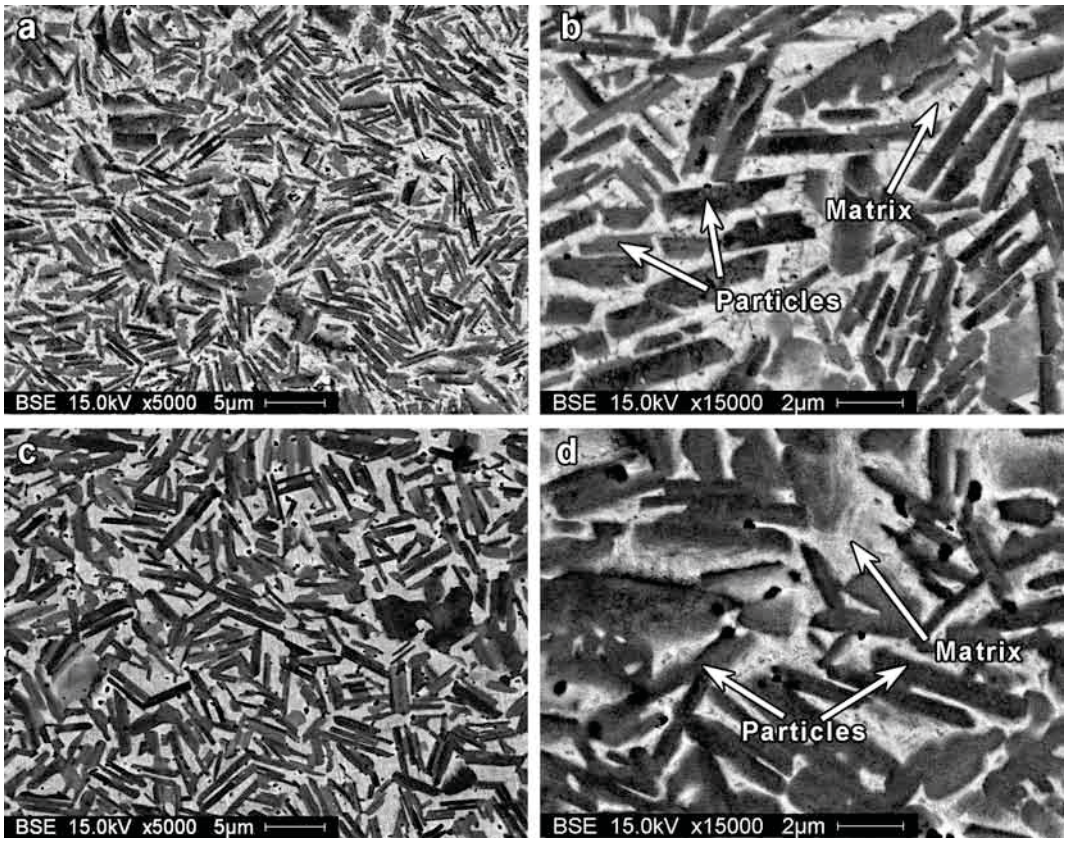

Figure 6.2: BSE micrographs of the as-polished (a,b) starting powder and (c,d) sintered specimen by SPS. The particles refer to the $(Cr,Fe)_2B$ phase, while the matrix refers to the Fe-based solid solution.

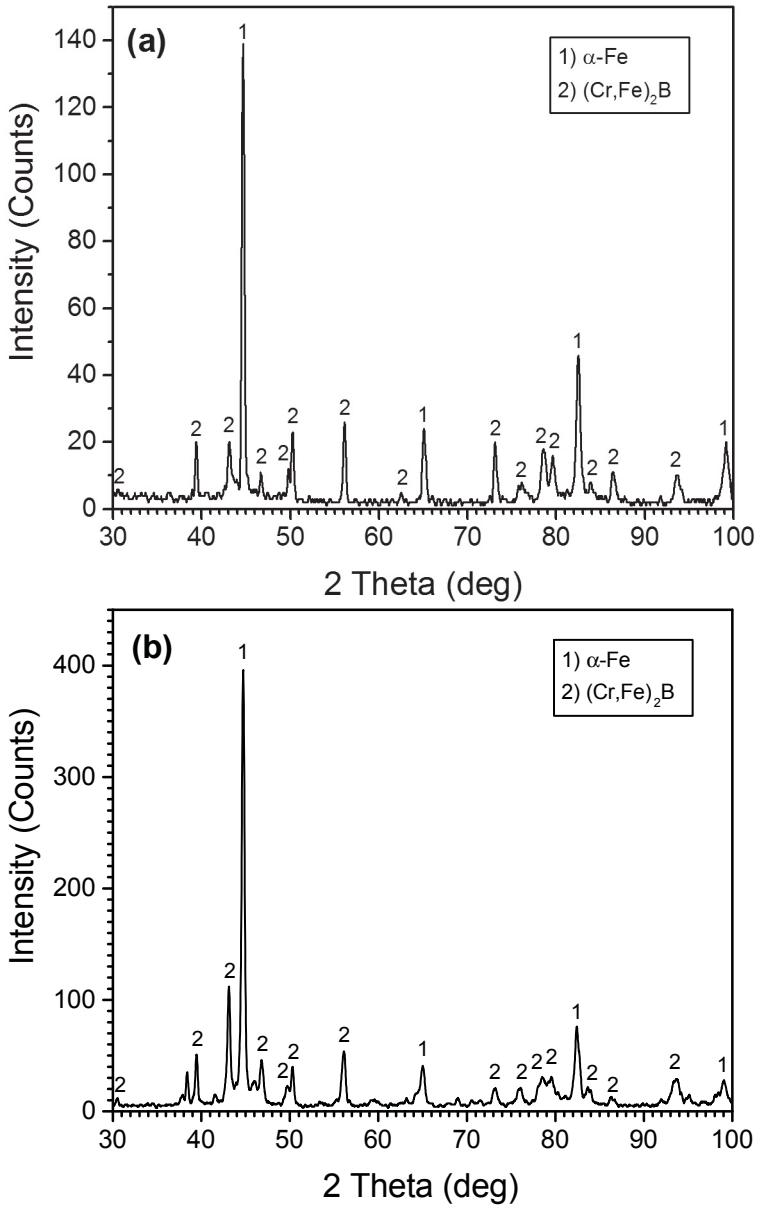

Figure 6.3: XRD results of (a) the starting powder and (b) the sintered specimen by SPS

Table 6.4: Reported and measured lattice parameters of the identified phases of the starting powder and sintered specimen by SPS

		Lattice parameters (Å)			
Material	Phase	a	b	c	Ref.
[1]Fe	α-Fe	2.866	2.866	2.866	[77]
[1]$Fe_{1.1}Cr_{0.9}B_{0.9}$	$(Cr,Fe)_2B$	14.57	7.32	4.22	[46]
[2]Powder	α-Fe	2.861 ± 0.001	2.861 ± 0.001	2.861 ± 0.001	
	$(Cr,Fe)_2B$	14.574 ± 0.001	7.322 ± 0.023	4.227 ± 0.001	
[2]SPS	α-Fe	2.870 ± 0.002	2.870 ± 0.002	2.870 ± 0.002	
	$(Cr,Fe)_2B$	14.672 ± 0.113	7.375 ± 0.416	4.227 ± 0.072	

[1] Reported in the literature
[2] Measured by XRD

Figure 6.4a shows SE micrograph of the etched powder. The shape of the $(Cr,Fe)_2B$ particles was irregular plate-like. Some of these plates were in contact with each other. The number of contact points to the number of plates for six micrographs were measured, and the ratio of points/plates number was 0.44 ± 0.12.

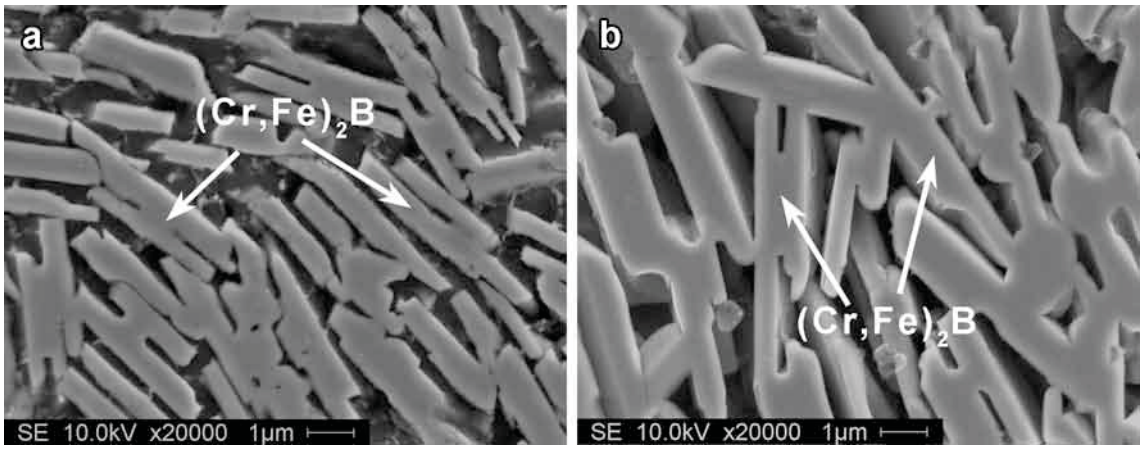

Figure 6.4: SE micrographs of the etched (a) starting powder and (b) sintered specimen, showing the morphology of $(Cr,Fe)_2B$

Thermodynamic Calculations

To further understand the solidified phases, thermodynamic analysis of the solidification of this gas-atomized alloy was performed. The solidification behavior of alloys has been widely studied [80–83] using the Scheil-Gulliver model [75, 76], which assumes infinitely fast diffusion in the liquid phase and zero diffusion in the solid phases. This model was valid for the solidification of the Fe–Cr–B-based alloy fabricated by the controlled short-circuit metal inert gas (CSC-MIG) welding process that yields a 10^2–10^4 °C/s solidification rate (Chapter 4). Since typical cooling rate of Fe-based

alloys fabricated by the gas atomization process is similar (10^3–10^4 ℃/s) [113], this model was applied here for the gas-atomized powder to provide reasonable estimates of the evolution of the phase fractions and solute distribution during the solidification.

Figure 6.5 and Table 6.5 illustrate the phase distribution evolution during solidification and chemical composition of each phase at transition temperatures, as calculated by the FactSage thermochemical software with the FSStel database [73] using the Scheil-Gulliver model [75, 76]. The $(Cr,Fe)_2B$ phase began to solidify at 1,664 ℃ and its content increased as the temperature decreased. At 1,217 ℃, a BCC phase containing Fe, Cr, Si and low contents of B and C started to solidify. At 1,204 ℃, the $(Cr,Fe)_7C_3$ phase formed. The solidification finished at 1,181 ℃, and the modeling alloy contained 64.1 wt.% $(Cr,Fe)_2B$, 35.0 wt.% BCC solid solution and 0.9 wt.% $(Cr,Fe)_7C_3$. The $(Cr,Fe)_2B$ and BCC α-Fe phases were detected by XRD (Figure 6.3a), though $(Cr,Fe)_7C_3$ was not detected because of its low content (0.9 wt.%). In addition, the peaks of $(Cr,Fe)_7C_3$ (JCPDS#005-0720) overlap with those of $(Cr,Fe)_2B$ (JCPDS#072-1073).

The volume fractions of the phases based on thermodynamic modeling (Table 6.5) were calculated and are presented in Table 6.3, assuming the density of $(Cr,Fe)_2B$ and $(Cr,Fe)_7C_3$ as 6.8 g/cm^3 and that of the matrix as 7.6 g/cm^3. The deviation of the calculated volume fractions from those measured by image analysis was less than 5%. This, in fact, indicates a valid approximation of the thermodynamic calculation using the Scheil-Gulliver model.

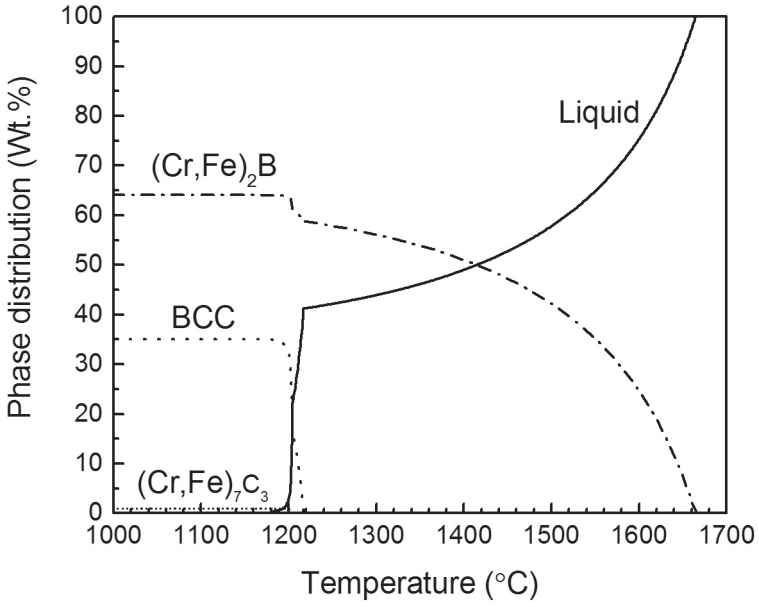

Figure 6.5: The phase distribution as a function of the temperature based on the Scheil-Gulliver model in the FactSage software for the investigated alloy composition: Fe–45Cr–5.9B–2Si–0.1C (wt.%)

Table 6.5: The modeled weight percent and chemical composition of each phase for the transition temperatures of the investigated alloy, as calculated by thermodynamic using the Scheil-Gulliver model

Temperature	Phase	Phase	Chemical composition (wt.%)				
(℃)		(wt.%)	Fe	Cr	B	Si	C
1664	Liquid	100	47.0	45.0	5.9	2.0	0.1
	$(Cr,Fe)_2B$	0	-	-	-	-	-
1217	Liquid	41.2	66.4	27.3	1.2	4.9	0.2
	$(Cr,Fe)_2B$	58.8	33.4	57.4	9.2	-	-
1204	Liquid	22.3	64.4	29.1	1.2	4.9	0.4
	$(Cr,Fe)_2B$	61.3	33.3	57.5	9.2	-	-
	BCC	16.4	74.4	20.0	0.01	5.6	0.05
1181	$(Cr,Fe)_2B$	64.1	33.2	57.6	9.2	-	-
	BCC	35.0	73.1	21.1	0.01	5.7	0.1
	$(Cr,Fe)_7C_3$	0.9	15.8	75.3	-	-	8.9

The equilibrium thermodynamic calculation was also performed to identify whether it agreed to Scheil-Gulliver cooling. The predicted equilibrium stable phases at 1,150 ℃ (sintering temperature) were similar: 64.0 wt.% $(Cr,Fe)_2B$, 35.1 wt.% (Fe,Cr) BCC solid solution and 0.9 wt.% $(Cr,Fe)_7C_3$. The equilibrium solidus temperature was predicted as 1,206 ℃, below which no phase transformation occurred.

DSC analysis

To measure the solidus temperature, DSC analysis of the starting powder was performed; the result is shown in Figure 6.6. A melting endothermic peak started at 1,215 ℃. This peak corresponded to the melting of the phases. This measured melting temperature was in agreement with the calculated one (1,206 ℃) by the equilibrium thermodynamic analysis. Similar behavior for the melting of the Fe–28.2Cr–3.8B–1.5Si–1.5Mn (wt.%) alloy has been found (Chapter 4); a small peak starting at 1,205 ℃ followed by superimposed main melting peaks.

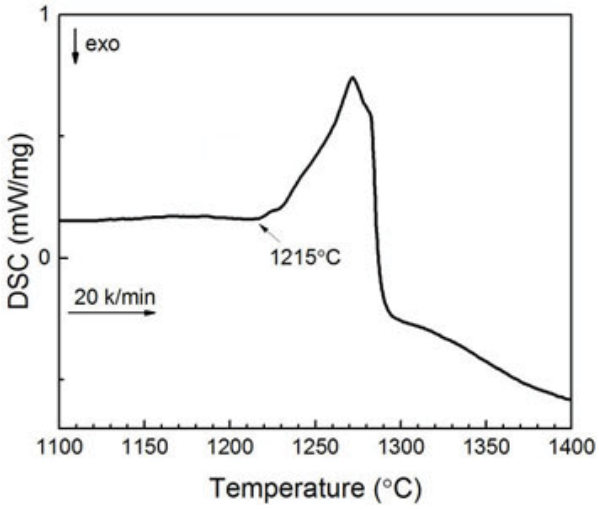

Figure 6.6: DSC curve for the starting powder fabricated by gas atomization

6.3.2 Characterization of the Sintered Specimen

Densification

The Fe–Cr–B-based alloy powder was sintered at 1,150 ℃ for a short period of time (10 min) using the SPS process to produce a bulk specimen. The measured density of the sintered specimen was higher than 98.5% of theoretical density. This full densification occurred at a sintering temperature lower than the solidus temperature (1,215 ℃, Figure 6.6).

Son et al. [11] and Do et al. [27] solid-state sintered the same alloy using the PIM process at the same temperature (1,150 ℃), as presented in Table 6.1. As the sintering time increased from 30 to 60 min, porosity was slightly reduced from 2.9 to 2.1 vol.%. In this investigation, the powder was successfully sintered with a porosity less than 1.5 vol.% at same temperature (1,150 ℃) for a shorter period of time (10 min). This SPS densification improved as compared to PIM mainly because of the application of pressure during the sintering cycle. The pressure has a direct effect on the particle sliding and re-arrangement, plastic deformation and destruction of agglomerates [32]. In addition, the role of electric fields in SPS processing to improve densification should not be ignored. The electric field has a thermal effect (Joule heating) and intrinsic role. Joule heating provides high heating rate (higher sinterability [114]) and creates local thermal gradients that induce the diffusion at particles boundaries. Intrinsically, the electric field enhances mass transport by electromigration [115], increase in point defect concentration [116], decrease in the mobility activation energy for defects [117] and/or dielectric breakdown of oxide layers (in non-conductive powders) [118]. Besides the improvement of the densification, the solid-state sintering maintains the original

structure of the phases and properties, as experimentally shown.

Microstructure Analysis

Figures 6.2c and d and Figure 6.3b show the sintered specimen's BSE micrographs and XRD, respectively. EDS analysis (Figure 6.7) showed that the matrix (S1) was rich in Fe, Cr and Si while the particles (S2) were rich in B, Cr and Fe. In the particles (S2), a small peak of Si was detected. The beam interaction within these particles was estimated by the Monte Carlo simulation using CASINO software [88], and it was found to reach up to 1 µm depth. Because the thickness of the particles was about 1 µm, the spectrum also contains information from the matrix as a result of the interaction volume of the beam with the matrix. In addition to these phases, a few precipitates (S3) that has brighter contrast than the particles (S2) were detected and were rich in C, Cr and Fe.

Similar to the powder, the sintered specimen consisted of the BCC Fe-based solid solution matrix containing Cr and Si, $(Cr,Fe)_2B$ particles and a few precipitates of $(Cr,Fe)_7C_3$. The measured volume fraction and aspect ratio of the particles for the sintered specimen are presented in Table 6.3. The particles' volume fractions and aspect ratios for the powder and sintered specimen were statistically similar.

Table 6.4 presents the measured lattice parameters of these phases. The measured and reported lattice parameters of $(Cr,Fe)_2B$ were similar. The measured lattice parameter of the α-Fe phase for the sintered specimen (2.870 ± 0.002 Å) was slightly higher than the one reported for pure α-Fe (2.866 Å) because of the substitution of Cr, which has larger atomic radii than Fe [84]. Silicon, which is smaller than

Fe [84], would decrease the lattice parameter, but this effect was neglected because of the smaller concentration of Si compared to Cr in the investigated alloy. However, the lattice parameter of the powder (2.861 ± 0.001 Å) was lower than that of the sintered specimen (2.870 ± 0.002 Å). This decrease most probably occurred because the matrix was supersaturated with B as a result of rapid solidification during the gas atomization process, as found by Jin et al. [13].

The shape of the $(Cr,Fe)_2B$ particles for the sintered specimen (Figure 6.4b) was similar to that for the powder (plate-like). However, the connection between plates was increased as a result of the SPS sintering. Due to the applied pressure and high temperature, the sample was deformed and thus the plates were brought into contact. The ratio of points/plates number was increased from 0.44 ± 0.12 (for the starting powder) to 0.73 ± 0.1 (after the sintering). Guo and Kelly [59] found similar shape of the boride phase in the casted Fe–11Cr–1.4B–1.2Si–1.1Ni–0.9Mo–0.7V–0.6Cu–0.2Mn–0.2C alloy. The plates were in contact with each other, and when the alloy was heat treated, the thickness of the plates increased and the connection between them became more prominent.

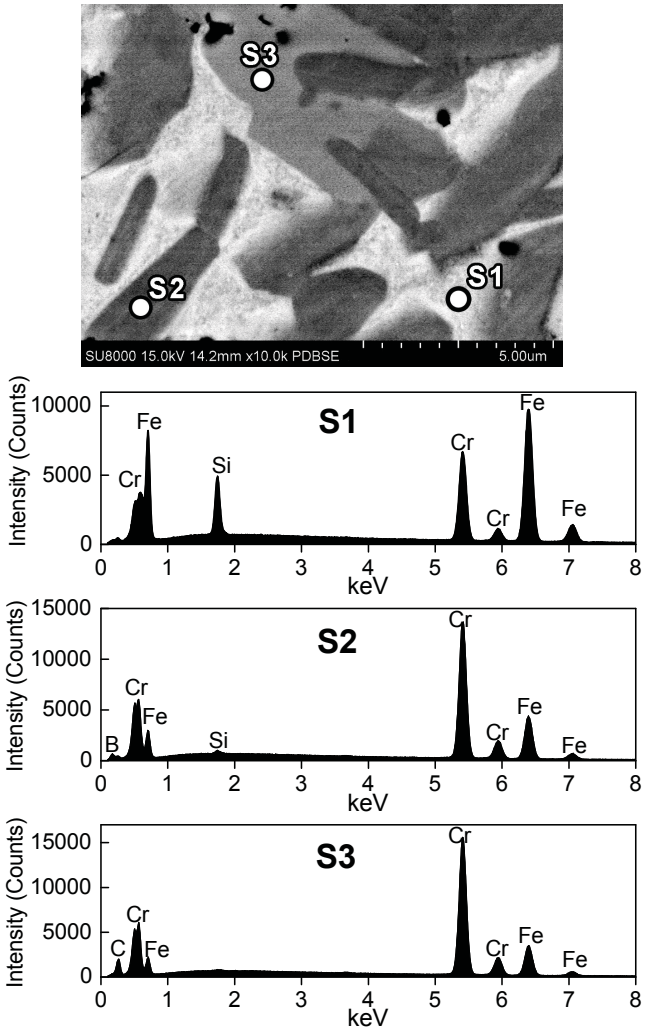

Figure 6.7: BSE micrograph of the sintered specimen with a corresponding EDS analysis at 15 keV accelerating voltage

6.3.3 Densification Modeling

While there is some controversy about the densification mechanisms during SPS, Olevsky and Froyen [43] developed the most complete constitutive model that describes SPS densification. They considered the dominant mass transport mechanisms for SPS densification as power-law creep, grain boundary diffusion, electromigration and surface diffusion. Milligan et al. [44] used the Olevsky and Froyen model [43] to describe the densification of Al–12%Si alloy. In addition, they added the plastic flow criterion developed by Helle et al. [42] to accommodate densification of a deformable alloy. In the present case, there is a lack in mechanical, diffusion and creep data for this matrix in the literature; thus, we used data for 304 stainless steel (Table 6.6) as material parameters as its properties assimilate those of this Fe–Cr–Si–C matrix for the same temperature range [119].

Table 6.6: Material data for the matrix phase

Material property			
Atomic volume	Ω (m^3)	1.21×10^{-29}	[120]
Surface tension	α (J/m^2)	1	[120]
Boundary diffusion			
Grain-boundary diffusion coefficient	$\delta_{gb}D_{gb}$ (m^3/s)	2×10^{-13}	[119]
Activation energy for grain-boundary diffusion	Q_{gb} (kJ/mol)	167	[119]
Power-law creep			
Exponent	m	0.133	[120]
Dorn constant	A	1.5×10^{12}	[120]
Activation energy for power-law creep	Q_{cr} (kJ/mol)	280	[119]

The plastic flow of the matrix (σ_m) reduces with temperature and was evaluated using the JMatPro simulation software [121] for the chemical composition: Fe–21.1Cr–5.7Si–0.1C (wt.%), as predicted by the thermodynamic calculation (Table 6.5). Figure 6.8 shows the evolution of the plastic flow of the matrix as a function of temperature. Above about 600 ℃, there is a sharp decreasing of the plastic flow. This decrease was believed to occur as a result of thermal activation mechanism that induces the dislocation motion to overcome obstacles [122, 123]. The data were exponentially fitted to establish the relation between σ_m (in MPa) and the temperature, T (in Kelvin), as follows:

$$\sigma_m = 1182 \exp\left(-\frac{T}{167.33} + 361\right) \qquad 298 < T < 823\ k \tag{6.1}$$

$$\sigma_m = 1.27 \times 10^6 \exp\left(-\frac{T}{100.13} + 2\right) \qquad T > 823\ k \tag{6.2}$$

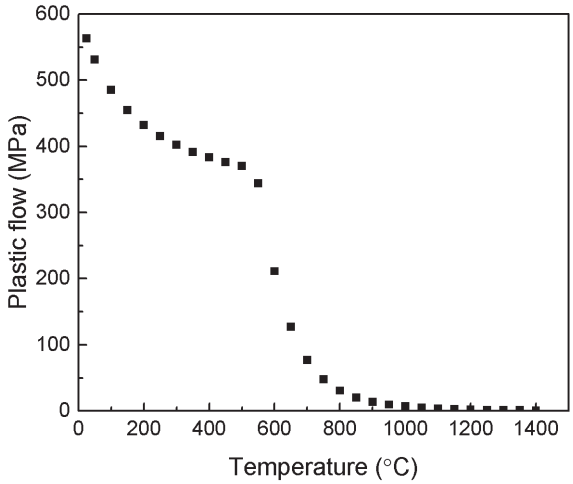

Figure 6.8: Plastic flow for a Fe–21.1Cr–5.7Si–0.1C (wt.%) alloy (matrix) as a function of temperature

The incorporation of a relatively high fraction of the reinforcement $(Cr,Fe)_2B$ plates in the matrix of the investigated alloy resulted in increases in yield strength relative to the matrix material. Xiong et al. [124] found that the deformation of composites is controlled by the matrix deformation and reinforcing reinforcement' movements and rotations. Therefore, the influence of the presence of undeformable particles on the plastic flow of this MMC must be considered in the overall deformation criterion. The compression flow stress of a reinforced composite (σ_c) can be calculated by [124]:

$$\sigma_c = \sigma_m S V_p \sum_{i=1}^{n} \frac{\cos^2 \alpha_i}{n} + \sigma_m \tag{6.3}$$

where σ_m is the flow stress of the matrix, S is the average aspect ratio of the reinforcements, V_p is the reinforcements volume fraction, α_i is the angle between the long axis of the reinforcements and the compressive direction and n is the reinforcements number. σ_m was calculated by Equations 6.1 and 6.2. S and V_p are presented in Table 6.3. The orientation distribution of 160 plates to the compression direction was random as shown in Figure 6.9. As a result, the flow stress of the investigated composite was not influenced during sintering because of the plate orientation changing.

Figure 6.10 compares the modeled overall densification with the experimental data as a function of time and temperature. The model started to deviate at 600 ℃. According to the model, the full densification should be reached at 1,095 ℃ under these pressing conditions.

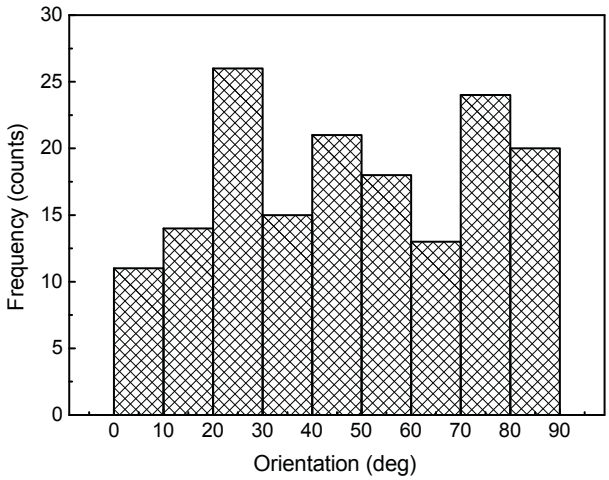

Figure 6.9: Orientation distribution frequency of the plates to the compression direction

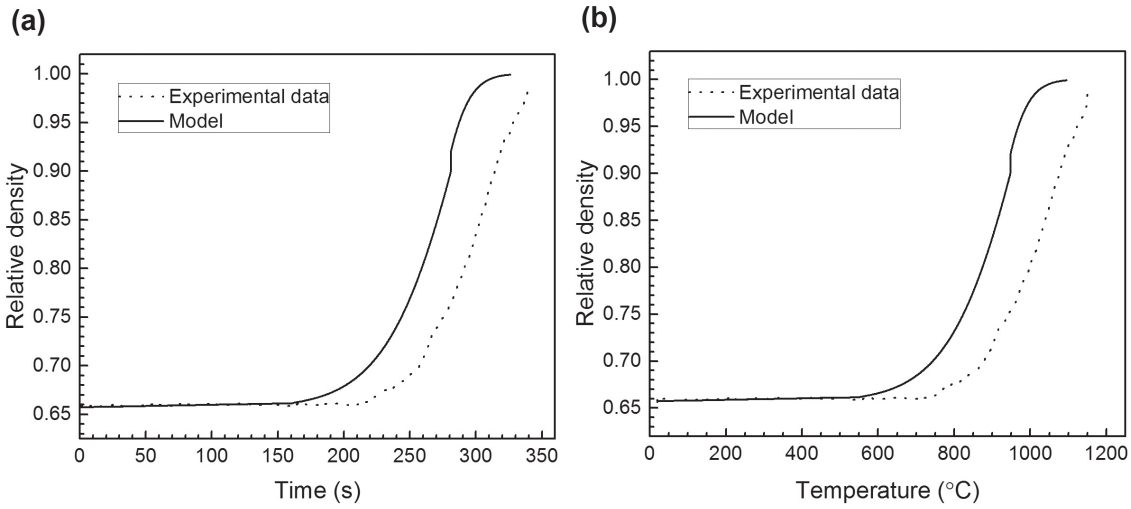

Figure 6.10: The calculated density by the densification model as a function of (a) time and (b) temperature vs. the experimental data

The deviation between the experimental data and model prediction of the densification may be attributed to one or more of the followings:

1. It has been found that the punches exhibited higher temperature than the sample, regardless of the sample's conductivity [125–127]. This temperature gradient decreased as the sintering temperature increased. In the used SPS system, the temperature was monitored during the process by a thermocouple that was placed inside the lower punch and was 2–3 mm below the sample. Therefore, the measured temperature was higher than the actual one inside the sample. The experimental densification curve (Figure 6.10) should be shifted to the left.

2. During the SPS process, the $(Cr,Fe)_2B$ plates sintered together, as shown in Figure 6.4. The ratio of the contact points to the plate number of the starting powder was 0.44 ± 0.12, and it increased to 0.73 ± 0.1 after the SPS sintering at 1150 ℃ for 10 min. The formation of this network between plates increased the yield strength of the matrix, and thus it has slow down the densification. Figure 6.11 shows that when the densification starts, the densification rate of the model is higher than that of the experimental data up to about 970 ℃.

The model approached the experimental data at high temperature because i) the temperature difference between the punch and the sample decreased, and ii) the contribution of the reinforcement on the yield strength of the composite was reduced at high temperature and thus the effect of the network formation between plates was diminished.

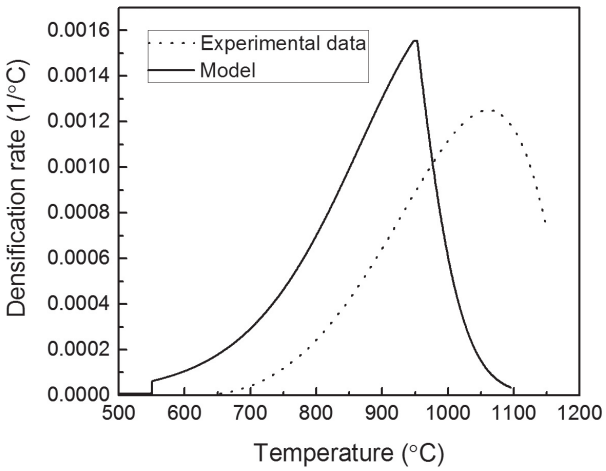

Figure 6.11: Densification rate for the densification curves that were calculated by the model and measured experimentally

Using this model, the densification map of this alloy as sintered by SPS at 200 ℃/min heating rate as a function of sintering temperature, time and pressure is shown in Figure 6.12. The sintering temperature linearly increased with time. As the temperature increased, the specimen density increased. When the sintering pressure increases from 50 to 150 MPa, while keeping the other parameters constant, the sintering temperature to reach full densification (100%) decreases from 1085 to 916 ℃.

The sintering temperature and time at which full densification reaches were also calculated as a function of the volume fraction and aspect ratio of the plates, as shown in Figures 6.13. As the volume fraction or aspect ratio of the $(Cr,Fe)_2B$ phase decrease, the temperature decreases. The fraction of $(Cr,Fe)_2B$ can be mainly decreased by reducing the B content [12, 27]. If the alloy do not contain this reinforcement plates, full densification occurs at 937 ℃. The aspect ratio of the $(Cr,Fe)_2B$ plates can

be reduced by heat treatment [12, 59], and full densification should be reach at 971 ℃ when the aspect ratio is unity.

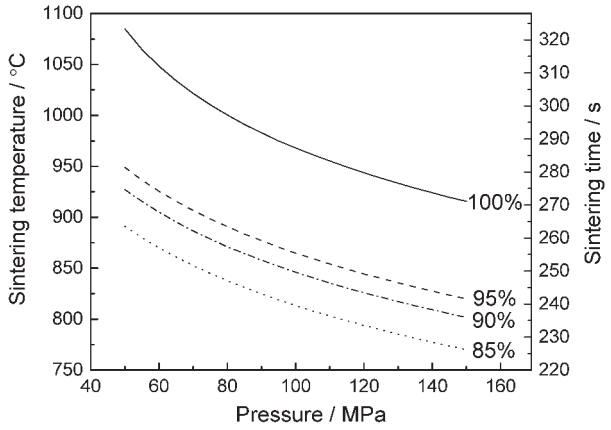

Figure 6.12: Densification map of the sintered alloy by SPS at 200 ℃/min as a function of sintering temperature, time and pressure

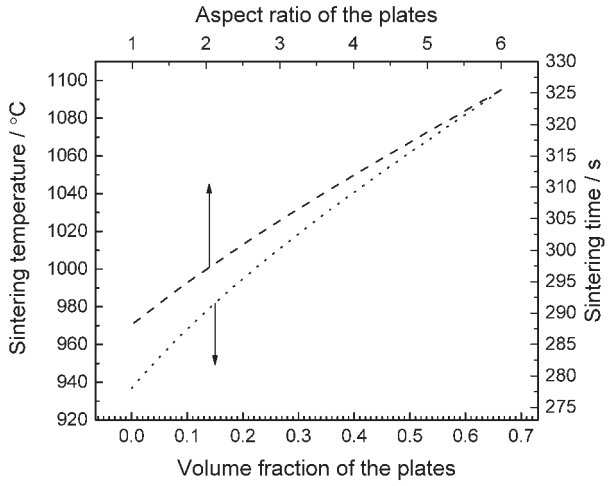

Figure 6.13: Full densification sintering temperature and time as a function of volume fraction and aspect ratio of the reinforcement $(Cr,Fe)_2B$ plates

6.4 Conclusion

In the present study, the gas atomized Fe–45Cr–5.9B–2Si–0.1C (wt.%) alloy powder was sintered using the SPS process. The microstructure and densification were investigated, and the following conclusions can be drawn. The alloy was fully sintered at temperature lower than solidus temperature for a short period of time. The solidified powder and sintered specimen mainly contained the primary $(Cr,Fe)_2B$ plates and the Fe-based bcc solid solution matrix composed of Cr and Si. In addition, the alloy contained a small amount of the $(Cr,Fe)_7C_3$ precipitate. Because the fraction, shape and aspect ratio of $(Cr,Fe)_2B$ did not change as a result of the sintering, the properties were expected to be similar before and after sintering. The accepted constitutive SPS densification model was augmented by including the effect of the hard $(Cr,Fe)_2B$ reinforcement to describe the densification evolution of this MMC during the SPS process. The model was in reasonable agreement with the experimental results.

Acknowledgments

We would like to thank Liquid Metal (CA, USA) for the powder provided, Sente Software Ltd (UK) for the high temperature strength calculations and Netzsch Instruments North America (LLC applications laboratory, Burlington, MA) for the DSC testing. We are grateful to King Fahd University of Petroleum and Minerals (KFUPM, Dhahran, Saudi Arabia) for the scholarship awarded to Ahmad A. Sorour.

CHAPTER 7

Microstructure and Tribology of Spark Plasma Sintered Fe–Cr–B Metamorphic Alloy Powder

[1]Ahmad A. Sorour[*], Holger W. Strauss[*], Richard R. Chromik[*] and Mathieu Brochu[*]

[*]Department of Mining and Materials Engineering, McGill University, 3610 University Street, Montreal, QC H3A 0C5, Canada

In chapter 6, the densification and microstructure of the gas atomized Fe–Cr–B-based alloy powder sintered by SPS were studied. In this chapter, hardness of the phases was measured by nanoindentation and that of the bulk specimen by Vicker microhardness. Dry sliding testing was performed to evaluate the tribology performance and study the wear behavior.

[1]Published: A.A. Sorour, H.W. Strauss, R.R. Chromik and M.Brochu, Tribology Letter, Vol.44, pp. 269–278, 2011

Abstract

The spark plasma sintering (SPS) process was used to fabricate a bulk Fe–Cr–B alloy (known as Armacor M) from gas-atomized powders. The purpose of this work was to study the microstructure, hardness and tribology of this sintered bulk alloy. Post microstructure and mechanical characterizations were performed to investigate the effects of wear on the microstructure and mechanical properties. Microstructural analysis using X-ray diffraction (XRD), scanning electron microscopy (SEM) and energy dispersive spectroscopy (EDS) showed that SPS successfully produced a fully dense bulk material containing 67 vol.% $(Cr,Fe)_2B$ particles dispersed in 33 vol.% solid solution matrix consisting of Fe, Cr and Si. Using nanoindentation, the hardness of the $(Cr,Fe)_2B$ particles and the matrix was found to be 24 and 6 GPa, respectively. From microindentation, the bulk hardness of the sintered alloy was 9.7 GPa (991 HV). Dry sliding wear testing under mild conditions (i.e., initial Hertzian mean contact pressure of 280 MPa) was conducted against a stainless steel counterface. The steady state coefficient of friction against Armacor M was about 0.82. The wear of Armacor M proceeded primarily by adhesive and mild oxidative wear. The wear volume for Armacor M was 80% less than that of carbon steel and its wear rate was 5.53×10^{-6} mm^3/Nm.

Keywords

Unlubricated wear; Adhesive wear; Oxidative wear; Borides; Ferrous alloys; Hardness

7.1 Introduction

Fe–Cr–B metamorphic alloys were first invented and commercialized by Scruggs [66]. They have been reported to exhibit excellent sliding and abrasive wear resistance [13, 14]. Therefore, they are good candidates for parts subjected to dry surface sliding such as bearings, shafts and other rotating equipment parts. Also, they have a potential to be used in applications involving erosion such as turbines, pipes and pumps. These alloys are often applied as a coating to reduce wear of the components used in these applications. The coatings of Fe–Cr–B metamorphic alloys have been fabricated by detonation gun thermal spray [13, 23, 24], high velocity oxygen fuel (HVOF) thermal spray [8, 14, 20], plasma transferred arc (PTA) weld-surfacing [10, 20] and high-energy electron beam irradiation (HEEBI) [8] processes. For all of these fabrication processes, microstructure analysis showed that the coating consisted of boride particles such as $Cr_{1.65}Fe_{0.35}B_{0.96}$ and/or Cr_2B dispersed in Fe-Cr solid solution matrix [8, 10, 13, 14, 20, 23, 24]. Although the existing phases are usually crystalline, HVOF spray produces a trace amount of amorphous phase and oxides [8, 20].

These specific alloys sometimes exhibit what is called a metamorphic transformation. When subjected to an external deformation such as wear, the solid solution matrix transforms to an amorphous phase, whereas the boride particles remain crystalline [13, 23, 24]. It was found that this metamorphic transformation depends mainly on the phase composition of the solid solution matrix [13] that is mainly determined by the process conditions. When the fabrication process involves melting and subsequent rapid solidification of the alloy such as HVOF spray and detonation gun at high gas content, thermal dissolution of the boride phase supplies boron into

the solid solution and increases its boron concentration [23, 24]. The metamorphic transformation occurs only when the boron concentration in the Fe-Cr solid solution phase reaches a certain critical limit (10 at.% based on Egami criterion [68] calculation) [23, 24]. This few-microns amorphous layer was confirmed by TEM and yielded a coefficient of friction (COF) as low as 0.1 and thus contributing to the high wear resistance [23]. Moreover, it was shown that the COF decreased as the Fe-Cr solid solution volume fraction increased [13, 23]. It is worth mentioning that when the fabrication processes such as HVOF involve slight oxidation, B and Si oxidize and thus their concentrations decrease to an extent that the elastic mismatch energy is reduced and thus the transformation is impeded [13].

Although the metamorphic transformation lowers the COF and improves the wear resistance, the density and microstructure of a Fe–Cr–B alloy coupon also play a major role on the wear resistance [20]. Wear performance and overall hardness are affected by the boride particle shape, size, volume fraction, distribution, orientation, modulus of elasticity and relative hardness that vary as a function of the process parameters [8, 20, 26]. When the boride phase has higher hardness, a larger size and perpendicular orientation to the wear track, the wear performance improves [10, 20].

Because of the importance of the microstructure and density, which depend on the fabrication process and parameters, selecting a fabrication process capable of producing a fully dense material with a controllable microstructure is very critical. Powder metallurgy is a well known process to control the microstructure of the bulk samples. Spark plasma sintering (SPS) is a novel process that uses pulsed high DC current with uniaxial pressure to rapidly consolidate powders of metals, ceramics and

composite materials [32]. It can produce a densely bulk material free of oxides with a minimal grain growth and a controlled microstructure because of a short sintering time [128, 129]. Consolidation using SPS of several systems has been reported but no investigation on the Fe–Cr–B alloy system was reported.

In this study, the SPS process was used to fabricate a bulk Fe–Cr–B alloy from gas-atomized powders. The main advantages of this process over currently used processes are to form a fully dense material free of oxides and imposing minimal microstructure changes after consolidation when compared with the gas-atomized powder. The purpose of this work was to study the microstructure, hardness and tribology of this sintered bulk alloy. Post microstructure and mechanical characterizations were performed to investigate the effects of wear on the microstructure and mechanical properties.

7.2 Experimental Procedures

7.2.1 Material

The material investigated in this research is commercially known as Armacor M, a brand name of Liquidmetal Technology, Lake Forest, CA, USA. The received powder was produced by high pressure argon gas atomization method. The spherical powder has a particle size of 40–100 µm as shown in Figure 7.1a. The chemical composition of the powder is listed in Table 7.1

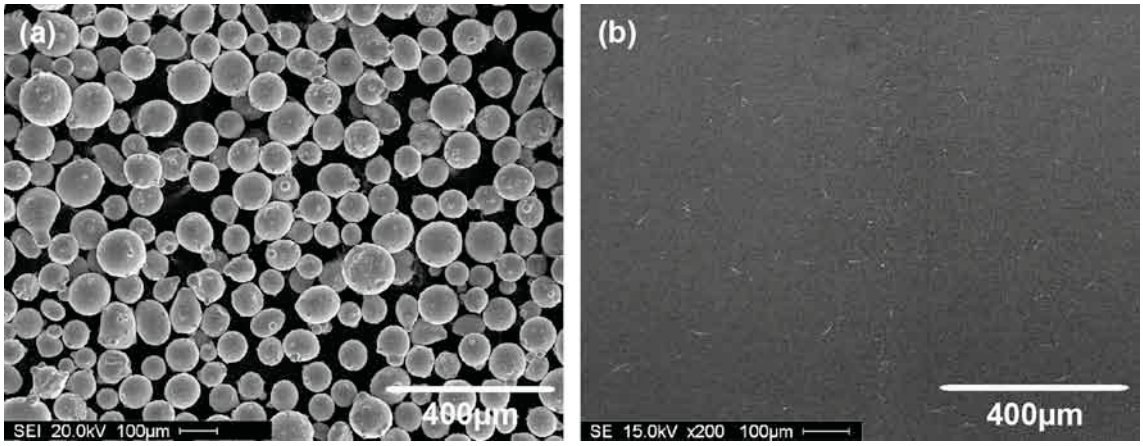

Figure 7.1: SEM (SE) micrograph of Armacor M (a) starting powder as received and (b) polished sintered specimen

Table 7.1: Chemical composition of Armacor M powder as received

Element	Fe	Cr	B	Si	C	S
wt.%	Bal.	43–46	5.6–6.2	1.75–2.25	0.17 max.	0.02 max.

7.2.2 Spark Plasma Sintering (SPS)

To fabricate bulk specimens, the powder was consolidated using the spark plasma sintering (SPS) system (Model 10-3 from Thermal Technology Inc., Santa Rosa, CA, USA), which has a capability of 10 tons force and a 3,000 A power supply. About 10 g of the powder was pressed in a graphite die under a 6×10^{-2} Torr vacuum. The powder was heated from 25 ℃ to 1,150 ℃ at 225 ℃/min. The holding time at sintering temperature (1,150 ℃) was 10 min. The loading pressure was maintained constant at 50 MPa during the cycle. The sintered specimens had a disc shape; 20 mm diameter and 3 mm thickness. The density of the sintered specimen was determined using Archimedes method.

7.2.3 Microstructure and Phase Analysis

For microstructural analysis and mechanical properties measurement, the bulk specimens were cut, mounted and then prepared using standard metallographic techniques. They were ground down to 800 grit using SiC papers followed by polishing using diamond solutions of 9, 3 and then 1 µm sizes. After the final polishing with colloidal silica (0.05 µm), the specimens were rinsed with acetone.

The phase analysis was performed using X-ray diffractometer (Philips PW1070; Cu Ka radiation) under the operation conditions of 40 kV and 20 mA with a scan rate of 0.025 deg/s. A Philips XL 30 Field Emission Scanning Electron Microscopy (FE-SEM) was used to acquire secondary electrons (SE) as well as backscattered electrons (BSE) micrographs. Oxford XMax Energy Dispersive Spectroscopy (EDS) and EDAX Phoenix EDS were used for elemental analysis. The Oxford XMax EDS is a Silicon Drift Detector (SDD) with a collection area of 80 mm^2 and a polymer-based window. Quantitative analysis was performed using commercially available image analysis software (Clemex Vision Professional 5.0, Clemex Technology Inc., Longueuil, QC, Canada) to measure the aspect ratio and volume fraction of the phases based on three micrographs acquired at different magnifications and involved more than 60 particles.

7.2.4 Hardness and Elastic Modulus Measurements

Hardness (H) and reduced elastic modulus (E_r) of each phase within the specimen were measured by nanoindentation conducted at room temperature ($\sim$ 21 ℃) using a Ubi-3 system (Hysitron Inc., Minneapolis, MN, USA) with a diamond Berkovich tip.

The system is equipped with a piezoelectric scanner used to acquire topographical images similar to atomic force microscopy (AFM). Prior to each indentation, a surface image of the specimen was acquired to identify the major phases within the microstructure and then to locate the indenter on the required location. The load-controlled indentation cycle was composed of loading for 5 s, holding at maximum load for 5 s and unloading for 5 s. The peak loads were controlled to be between 1.5 mN and 7 mN, where the loads used for each phase were chosen such that the contact depth (h_p) was between 60 nm and 100 nm. For each phase, ten indents were performed to obtain mean values and standard deviations. The H and E_r were calculated from the load-displacement curves using Oliver and Pharr method [98]. However, pile-up was observed for all indents and thus contact areas needed to be recalculated taking into account the increase in the contact depth because of pile-up. To achieve this, post scanning of each indent was performed and the increase in the contact depth was measured using software (provided by the instrument manufacturer). Then, the contact area was recalculated using the area function determined by calibration indentation on fused quartz.

Microindentation was used to measure the hardness of the overall sintered bulk specimen using a Clark Microhardness Tester (Model CM-100 AT) with Vickers diamond indenter. The measurements were performed on a polished surface at room temperature ($\sim$ 21 ℃) under a load of 300 g with 16 indents to obtain mean values and standard deviations. Post optical graphs of the indents were acquired and were used to measure the indent size using image analysis software. Hardness was calculated using the standard definition of Vickers hardness and also based on the projected

contact area in units of GPa [130, 131]. To compare Vickers and nanoindentation results, the Vickers hardness should be calculated based on the projected area because the nanoindentation hardness is based on the projected area [130].

7.2.5 Tribology Tests

Wear testing was performed using a custom-built linear reciprocating tribometer (ball-on-flat configuration) [132]. All wear tests were conducted in dry sliding conditions (unlubricated) in ambient air at room temperature ($\sim$ 21 °C) and room humidity (37–42% RH). Each wear test condition was repeated three times. The counterpart was a bearing stainless steel ball (type 440C) with a diameter of 12.7 mm (0.5 inch) and a hardness of about 7.2 ± 0.2 GPa. The track length was 2 mm and the sliding speed was kept constant at 3 mm/s. Depth profiles of the wear tracks were measured (three measurements per track) using a stylus profilometer. The wear volume was calculated by taking the average of these three measurements for the cross-sectional area of the wear scar and multiplying it by the track length (2 mm). Microstructural and mechanical characterizations of worn surfaces were accomplished by SEM, EDS and nanoindentation. To determine the wear volume of the slider, optical microscopy was used to acquire a micrograph of the wear scar after each wear test to measure the scar diameter. Then, the wear volume was calculated using a method described by Whitenton and Blau [133] and also described in ASTM Standard G99 [134]. For comparison purposes, the same wear tests and analysis were conducted onto a medium-carbon steel (AISI 1030) specimen, which has a hardness of 169 ± 3 HV (1.65 ± 0.03 GPa).

7.3 Results and Discussion

7.3.1 Microstructure and Phase Analysis

Figure 7.1a and b shows the secondary electron (SE) micrograph of Armacor M starting powder as well as polished bulk specimen consolidated by the spark plasma sintering (SPS) process. The powder was spherical in shape, which is typical for the gas atomization process. The bulk specimen analysis (Figure 7.1b) showed no cracks, pores or porosity. The measured density of the bulk specimens (about 7.02 g/cm^3) was higher than 97% of the theoretical density (7.24 g/cm^3 [10]) of Armacor M powder. For this consolidation conducted at 1,150 ℃ for 10 min, conditions were sufficient to produce specimens free of cracks and pores with high density and low porosity.

Phase identification for the starting powder and sintered specimen was conducted with X-ray diffraction (XRD) analysis and the results are shown in Figure 7.2. Sharp diffraction peaks indicated that the phases are crystalline. Before and after consolidation, the spectra showed peaks of a bcc structure of Fe (JCPDS 6-0696) and Cr (JCPDS 1-1261) crystalline phase. Also, peaks of boride phases were detected, such as $Cr_{1.65}Fe_{0.35}B_{0.96}$ (JCPDS 35-1180), Cr_2B (JCPDS 38-1399) and/or CrB (JCPDS 32-0277). Peak convolution for these phases prevented complete identification. In addition, FeB (JCPDS 32-0463) phase peaks were detected only from the sintered bulk specimen indicating some small precipitation of this phase occurred during the consolidation.

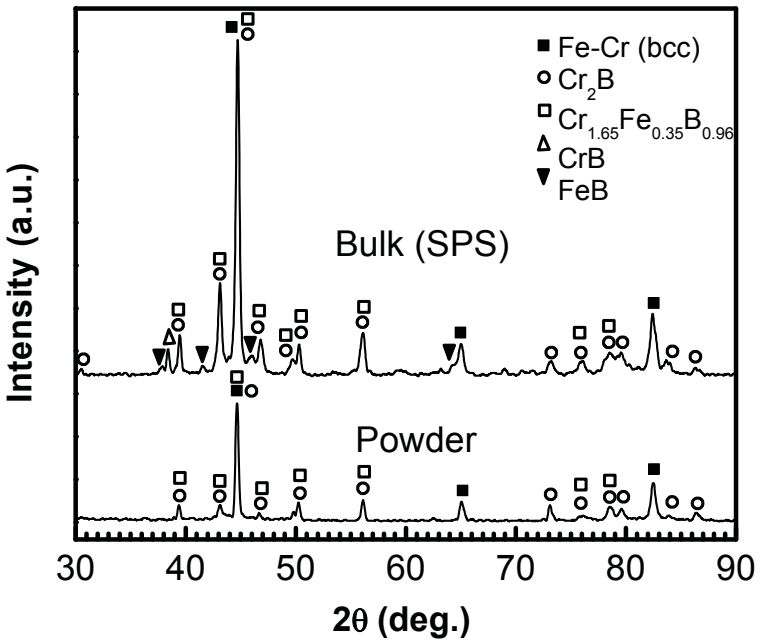

Figure 7.2: XRD results of Armacor M starting powder and sintered bulk specimen

Figure 7.3a and b shows the backscattered electron (BSE) micrograph of the starting powder and the sintered bulk specimen, respectively. Both microstructures showed two distinct phases as rod-like particles (dark phase) dispersed in a matrix (light phase). EDS analysis showed that the corresponding phases in the starting powder and bulk specimen have the same chemical constituents. The EDS analysis of the particles (Figure 7.3c) indicates a Cr-rich phase containing Fe and B. The matrix (Figure 7.3d) is rich in Fe and contains Cr and Si.

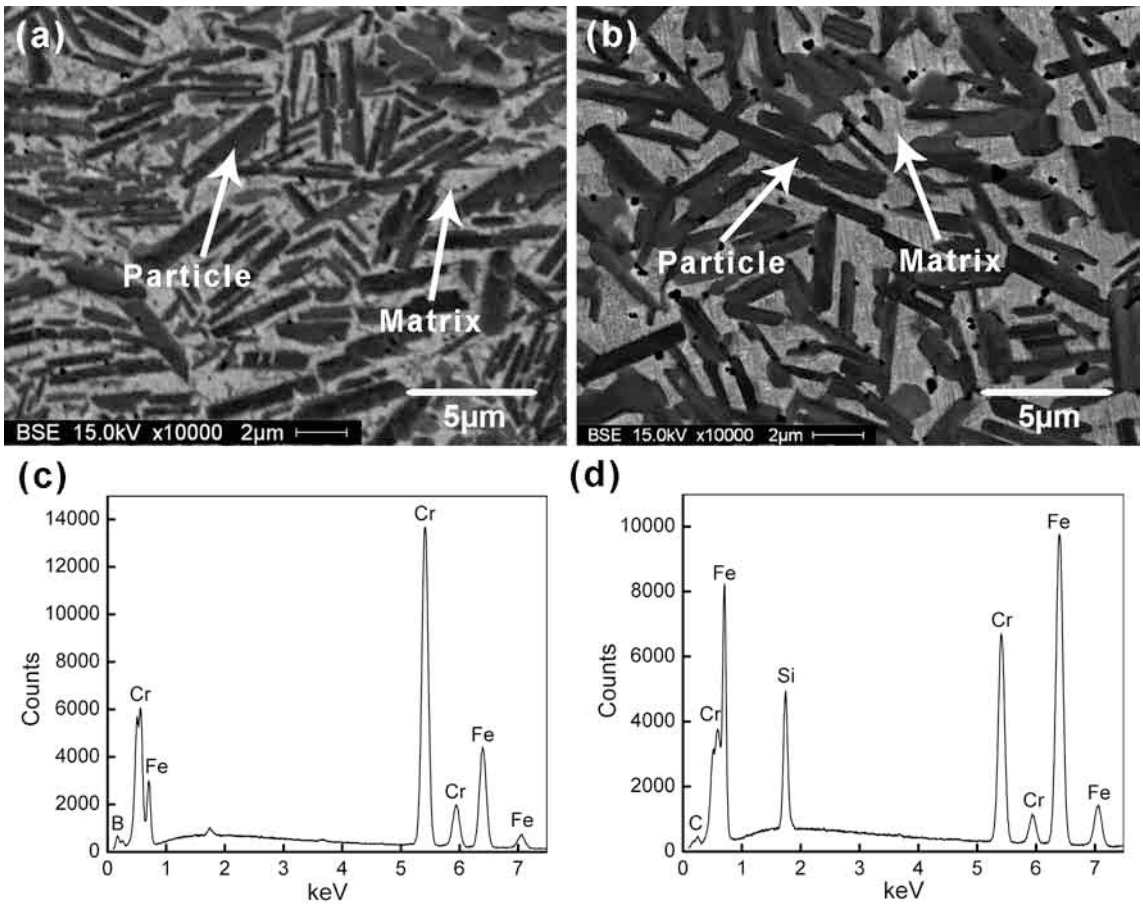

Figure 7.3: SEM (BSE) micrograph of Armacor M (a) starting powder and (b) sintered bulk specimen with a corresponding EDS analysis using Oxford XMax EDS of (c) particles and (d) matrix

Based on XRD results (Figure 7.2), the particles seem to be $Cr_{1.65}Fe_{0.35}B_{0.96}$ which was also reported for the same alloy fabricated by other methods [8, 58]. The Cr_2B phase, which was also detected by XRD (Figure 7.2), has been reported for the same alloy [10, 20] and was shown by TEM as nanoparticles (less than about 200 nm in diameter) [23, 24]. Thus, it could exist in the investigated sintered alloy as nano-precipitates that could not be confirmed by SEM and EDS.

The matrix of the sintered specimen by SPS is identified to be Fe-based solid solution composed of Fe, Cr and Si. The matrix contains zero or a very low level (less than a detectability limit of EDS) of boron. The absence of boron in the solid solution was expected because the solid solution phase of the gas atomized powder as shown by H.W. Jin et al. revealed no boron peak using Auger elemental analysis [24]. Also, the SPS is a solid state consolidation process that did not involve melting and rapid solidification. In contrast, the deposited alloy by the detonation gun had a significant amount of boron ($\sim$ 7 at.%) in the solid solution as a result of melting and rapid solidification [24]. Boron plays an important role for the metamorphic transformation that occurs when the boron concentration in the Fe-Cr solid solution is more than 10 at.% [23]. In our case, the B concentration in the solid solution of the sintered specimen was lower than the critical concentration (10 at.%). Therefore, it is expected that the metamorphic transformation will not occur in the alloy fabricated by SPS process in this investigation.

Table 7.2 summarizes the quantitative image analysis results of the aspect ratio of the boride particles and their volume fraction for the starting powder and the bulk specimen sintered by SPS. The average aspect ratio of the boride particles in the

powder (5.02) was equivalent to that of the sintered specimen (5.01). Similarly, the volume fraction of the particles was statistically similar for the starting feedstock (63.2 ± 3.2) and after consolidation (66.8 ± 2.1). Lee et al. [8] showed that the particle volume fraction for the same alloy studied here but fabricated differently was 63.9 ± 5.2 using high energy electron beam irradiation (HEEBI) and was 75.5 ± 6.4 using the high velocity oxygen fuel (HVOF) thermal spray process. The volume fraction of the boride particles changed from one process to another because of the nature of the process parameters [23] that particularly determine the fraction of melted materials and the solidification rate. Moreover, when the Fe–Cr–B metamorphic alloy powder was deposited using detonation gun, the volume fraction of the boride particles decreases from about 39% to 26%, which was associated with thermal dissolution during the thermal spray process [24]. In our case, the SPS process did not involve melting and dissolution during the sintering and thus the boride fraction remained similar as depicted in Table 7.2.

Table 7.2: Quantitative data analysis of the powder and the bulk specimen sintered by SPS

Process/material	Aspect ratio	Volume fraction (%)	
	Particles	Particles	Matrix
Gas atomized powder	5.02 ± 1.1	63.2 ± 3.2	34.8 ± 1.4
SPS bulk	5.01 ± 1.3	66.8 ± 2.1	32.8 ± 1.9
HEEBI surface [8]	63.9 ± 5.2		
HVOF coating [8]	75.5 ± 6.4		

7.3.2 Hardness and Reduced Elastic Modulus

The average hardness (H) and reduced elastic modulus (E_r) of $(Cr,Fe)_2B$ particles (Figure 7.3b) were 24 ± 1 and 320 ± 6 GPa, respectively. Figure 7.4a shows the post AFM micrograph of the particle representative indent in this phase. The average H of the matrix was 6 ± 1 GPa and the average E_r was 238 ± 11 GPa. The post AFM micrograph of the indent on the matrix is shown in Figure 7.4b. The H of the matrix of the same alloy fabricated by HEEBI was reported by Lee et al. [8] as 4.5 GPa (measured by the Vickers microhardness under a 10 g load and calculated based on the projected area), which is lower than that measured by nanoindentation (6 GPa). The penetration depth of nanoindentation was about 100 nm which is lower than that of the Vickers microhardness (about 940 nm). The difference between our measured H and that measured by Lee et al. may be because of an indentation size effect (ISE) [135].

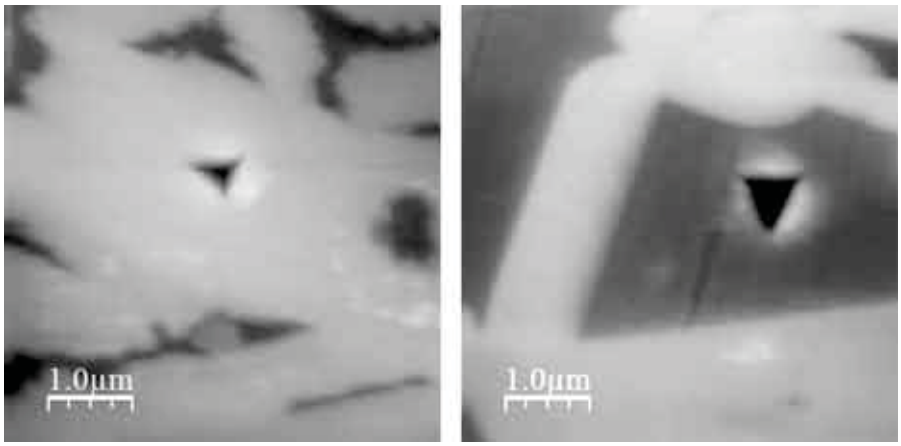

Figure 7.4: AFM micrograph of the indent on Armacor M (a) particle and (b) matrix after the nanoindentation test using Berkovich tip

Microindentation measurements under 300 g load using the Vickers indenter showed that the H of the sintered bulk specimen was 991 ± 30 HV (9.7 ± 0.3 GPa). This H is a combination of the both phases H as well as the interfaces between these phases. The Vickers H under the same load (300 g) of the same alloy fabricated by HEEBI and HVOF was reported as 538 ± 26 HV (~ 5.3 GPa) and 899 ± 94 HV (~ 8.8 GPa), respectively [8]. The difference in the hardness of these materials originates from the difference in the microstructures because the volume fraction and shape of boride and matrix are modified by the process parameters [8]. Other researcher [58] reported the H of the HVOF Armacor M as 12 GPa and the elastic modulus as 210 ± 40 GPa. The volume fraction of the boride phase in the sintered specimen was about 67% and hence its bulk hardness was higher than the one fabricated by HEEBI, which has 64% of the boride phase. Also, the microstructure characteristic, size and distribution of the boride phase differ from process to process and thus result in varying hardness. For the material fabricated here, the morphology of the indent under 1,000 g load (Figure 7.5) showed cracks within the indent. Nevertheless, it did not show any evidence of cracks at the indent corners or the boundary, indicating a high degree of toughness for this metalceramic composite. Indeed, no delamination between the two phases was observed which was attributed to the high adhesion strength between the two phases.

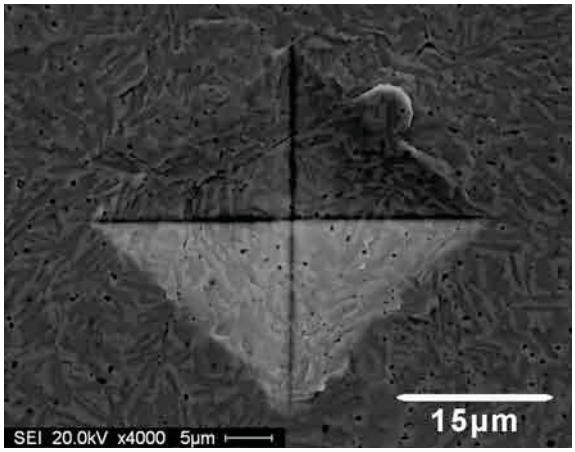

Figure 7.5: SEM (SE) micrograph of the microindent on Armacor M using Vickers tip with load of 1,000 g

7.3.3 Friction and Wear Rate

Tribology tests were performed using dry reciprocating sliding of the investigated alloy against stainless steel ball to evaluate coefficient of friction (COF) and wear resistance. Based on modulus of elasticity (determined by nanoindentation) and the volume fraction of the boride particles and the solid solution matrix (Table 7.2), the applied normal load (0.8 N) resulted in an estimated initial Hertzian mean contact pressure [2] of about 280 MPa.

Figure 7.6 shows the COF evolution as a function of cycle number for the sintered bulk specimen. Initially up to about ten cycles, the COF was low (about 0.2). Then, the COF jumped to about 0.5 and was unstable with high variation and a gradual increase up to 200 cycles. After 200 cycles, the COF reached a steady state value of about 0.82. Based on repeating sliding wear tests with the same parameters and conditions (excluding the first 1,000 cycles), the average steady state COF value was

0.82 ± 0.03 for Armacor M bulk specimen compared with 0.74 ± 0.04 for medium-carbon steel. The COF value of Armacor M sintered by SPS is very close to the value reported for the same alloy slid against alumina and hardened 100Cr6 balls that were 0.83 and 0.94, respectively [58]. Although the metamorphic alloy can have a low COF at about 0.1 [23], the alloy fabricated by SPS exhibited a much higher COF (about 0.82). This difference was expected because the boron concentration in the solid solution phase did not reach the critical value of 10 at.% [23], which is essential for the metamorphic behavior.

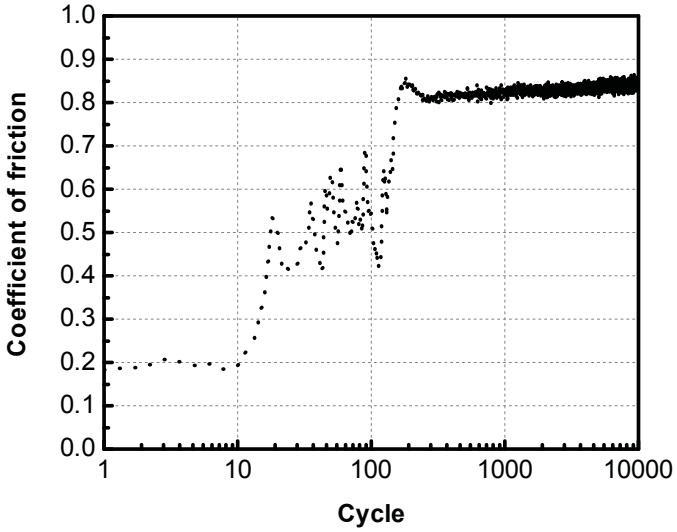

Figure 7.6: The coefficient of friction evolution of Armacor M alloy when slid against stainless steel counterface up to 10,000 cycles

Figure 7.7 shows the wear volume of Armacor M sintered specimen as well as medium-carbon steel as a function of sliding distance. In both materials, wear volume increases as the sliding distance increase. Armacor M exhibited about 80% less wear volume than carbon steel. Based on the wear volume data (Figure 7.7),

the wear rate (sliding wear coefficient, k) [136] of Armacor M alloy was calculated as 5.53×10^{-6} mm^3/Nm compared with 2.52×10^{-5} mm^3/Nm for medium-carbon steel. The typical wear rate of carbon steel was reported between 1×10^{-5} and 4×10^{-5} mm^3/Nm that depends on the sliding speed, normal load, microstructure and hardness [137–140]. The sliding wear coefficient of Armacor M was about 78% less than that of carbon steel.

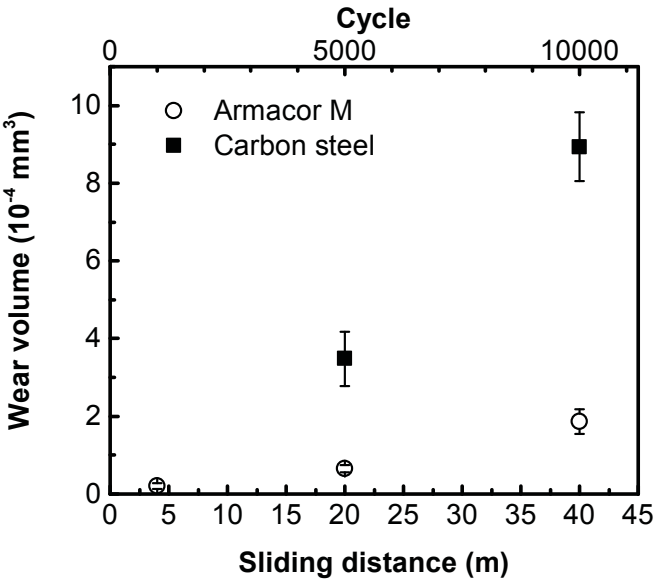

Figure 7.7: Wear volume of the Armacor M and carbon steel worn by the stainless steel counterface as a function of sliding distance. The *error bar* denotes one standard deviation.

The stainless steel ball slider was also worn during sliding as shown in Figure 7.8. Figure 7.9 shows wear volume of the balls used in wear testing against the Armacor M and carbon steel at different cycles. While wear volume values of the ball were not equivalent to wear volume of Armacor M and carbon steel (Figure 7.7), they have a similar trend.

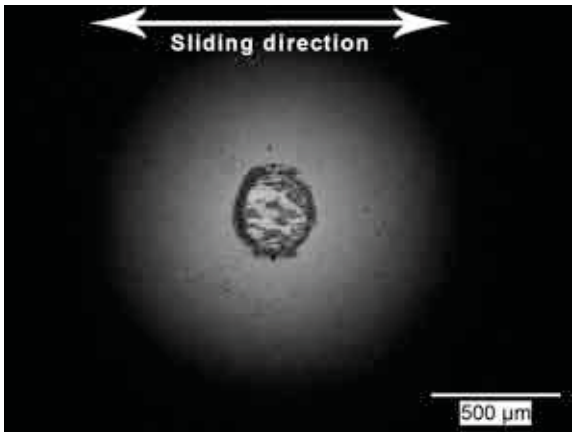

Figure 7.8: Optical micrograph of the wear scar on the stainless steel counterface ball slid against the Armacor M alloy for 20 m

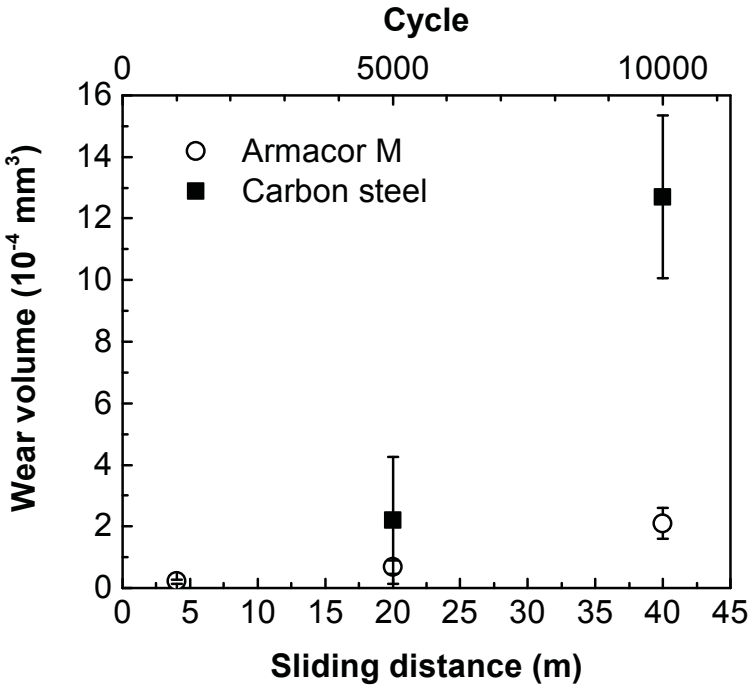

Figure 7.9: Wear volume of the stainless steel counterface when slid against the Armacor M and the carbon steel as a function of sliding distance. The *error bar* denotes one standard deviation

7.3.4 Microstructure Evolution During Wear

Figure 7.10a-d shows BSE micrographs of the sintered Armacor M alloy worn surfaces after 10, 100, 1,000 and 5,000 cycles. Although the boride particles (dark phase) were not damaged, parts of the matrix (light phase) oxidized (according to EDS analysis as shown in Figure 7.10e) and parts were removed at different cycles. During sliding, friction generates heat that increases the contact temperature. This elevated temperature did not oxidize the boride particles because of their high thermodynamic stability. On the other hand, the matrix oxidized because the oxides of its elements (Fe, Cr and Si) are thermodynamically stable at high temperature [141]. The tribo-oxides (oxides formed because of wear) were almost consistent throughout the wear sliding. However, the matrix was initially damaged at ten cycles, completely removed at 100 cycles and partially removed after 1,000 cycles. The Fe-Cr solid solution matrix worn more than the boride during wear because the matrix has lower hardness than the boride phase [10, 20]. The SE micrograph of the wear track after 5,000 cycles (Figure 7.11a) shows distributed debris around the wear track. This debris, which has irregular shape (Figure 7.11b), was confirmed by EDS analysis (Figure 7.11c) as oxides of Fe, Cr and/or Si.

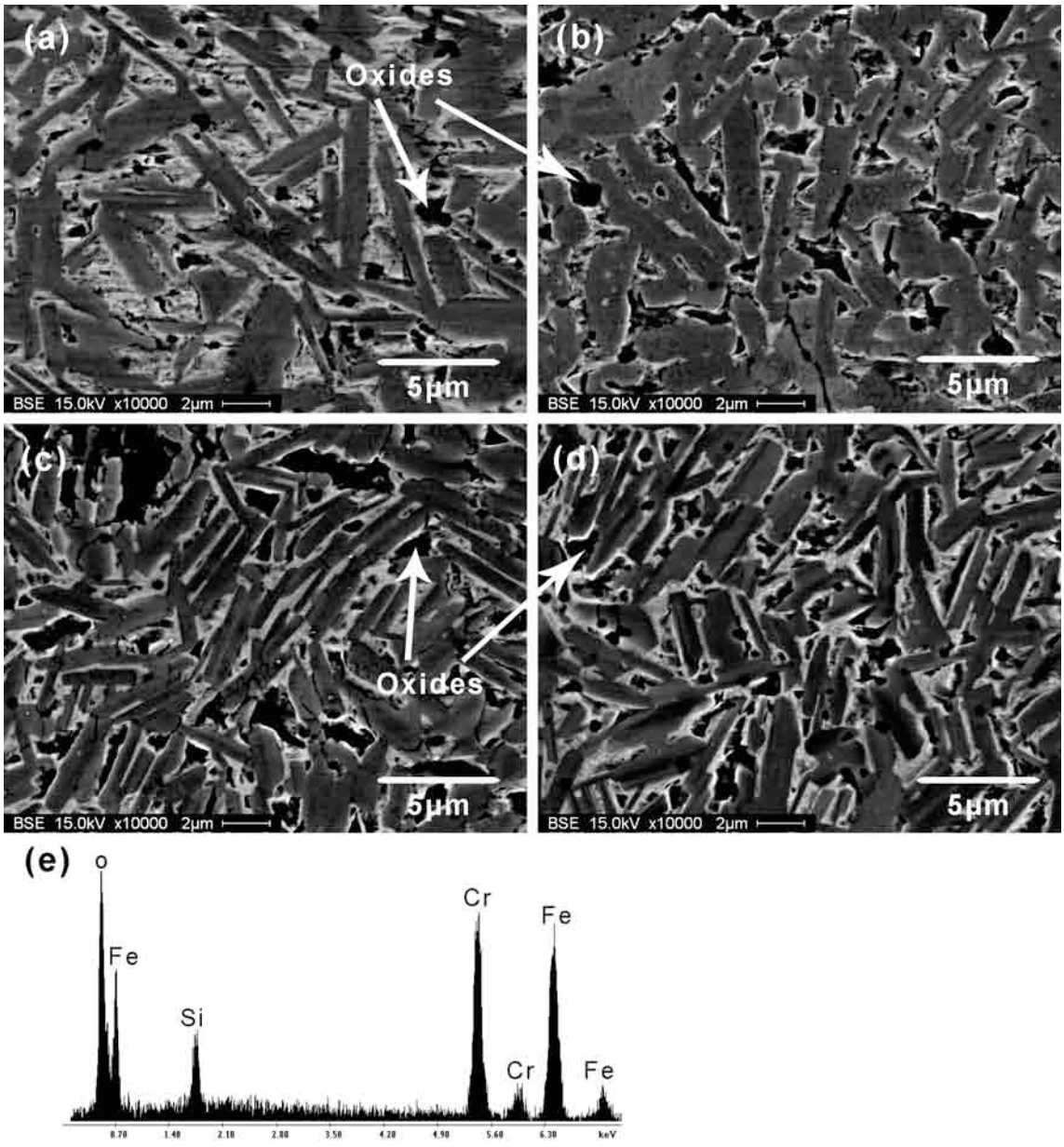

Figure 7.10: SEM (BSE) micrograph of worn surfaces after (a) 10 cycles, (b) 100 cycles, (c) 1,000 cycles and (d) 5,000 cycles with (e) a corresponding EDS analysis (using EDAX Phoenix EDS) of the oxide particles (*black*)

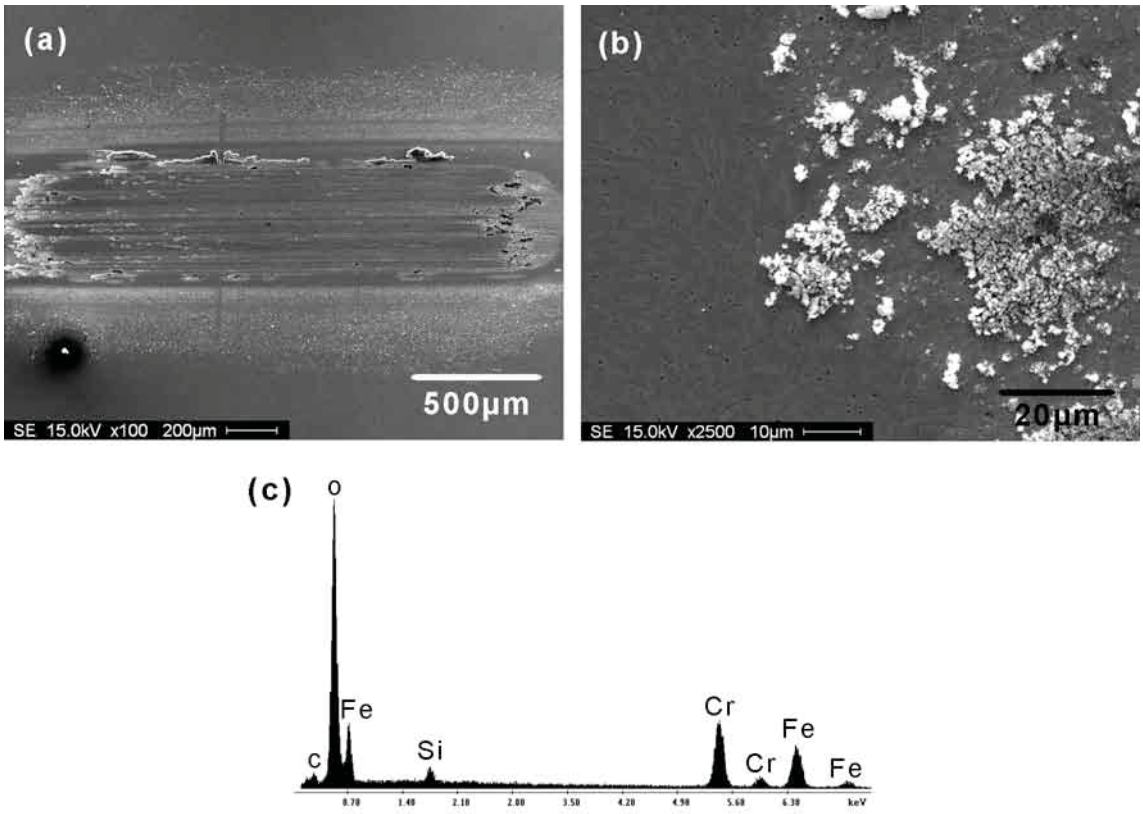

Figure 7.11: SEM (SE) micrograph of (a) the Armacor M wear track after 5,000 cycles and (b) debris at high magnification with (c) a corresponding EDS analysis (using EDAX Phoenix EDS) of the debris

7.3.5 Hardness and Reduced Modulus During Wear

The changes in H and E_r of each phase after 5,000 cycles (20 m sliding distance) were measured also by the nanoindentation. The matrix was partially oxidized and damaged, but nanoindentation was performed on the smooth areas whose smoothness was confirmed by a pre AFM-like scan. Three indents showed that the H and E_r of the boride particles after 5,000 cycles were 25 ± 2 GPa and 328 ± 12 GPa, respectively. These values are statistically equivalent to that obtained for the unworn surface (H of 24 ± 1 GPa and E_r of 320 ± 6 GPa). The H of the solid solution matrix also equivalents in the unworn (6 ± 1 GPa) and worn (7 ± 1 GPa) surfaces. However, E_r decreased slightly from 238 ± 11 GPa (unworn) to 225 ± 17 GPa (worn).

It has been shown that the ability of a material to resist wear is related to the ratio of the hardness and elastic modulus (H/E), which is the elastic strain to failure [142]. The H/E_r ratios of the boride particles before and after wear were the same 0.075 ± 0.003 and 0.076 ± 0.007, respectively. The H/E_r ratio of the matrix increased slightly from 0.025 ± 0.004 to 0.031 ± 0.005. This small increase improves the wear resistance of the matrix and consequently contributes to better overall wear resistance. The H/E_r ratio can change after wear as a result of the hardness decreasing because of tempering at high temperature or hardness increasing as a result of work hardening or the metamorphic transformation [20]. Because the metamorphic transformation did not occur in this alloy as it was confirmed before, the change in the mechanical properties was most probably because of strain hardening but might also be related to oxidation.

7.3.6 Proposed Wear Mechanism

Initially, the COF was low (about 0.2) and no significant surface damage was observed. Concurrently, the Armacor M matrix and the stainless steel counterface oxidized partially as a result of frictional heat. The oxides and the Armacor M matrix were removed by the act of shearing (adhesive wear) forming the debris. At the steady state, the contact pressure dropped because of wear of the slider and also the matrix was also oxidized and removed but the boride particles were worn out simultaneously by adhesion. It could also be because of the fact that the boride particles were pushed inside the matrix. Although the wear mechanism is not fully obvious, we propose that the dominant wear mechanism was a combination of adhesive and mild oxidative wear.

Currently, the Armacor M alloy fabricated by SPS was tested at low load (0.8 N) and short-to-moderate sliding distances. The alloy exhibited high wear resistance compared with a carbon steel as comparison. To more fully understand the wear performance for harsher applications, sliding wear test at higher loads and longer sliding distances as well as abrasive wear tests need to be performed. However, this study provided an indication of the potential for the SPS process to produce a fully dense metal-ceramic composite with high wear resistance.

7.4 Conclusions

1. Spark plasma sintering process was successfully used to fabricate a fully dense bulk material of Armacor M that contains about 67 vol.% $(Cr,Fe)_2B$ hard particles dispersed in 33 vol.% solid solution matrix consisting of Fe, Cr and Si.

2. The bulk hardness of this alloy was 9.7 GPa (991 HV). The hardness of $(Cr,Fe)_2B$ particles was 24 GPa and of the matrix was 6 GPa.

3. The coefficient of friction of Armacor M against stainless steel counterface was about 0.82 which is higher than that of carbon steel (about 0.74). However, the wear volume of Armacor M was 80% less than that of carbon steel and the wear rate was also 78% less.

4. The wear mechanism of Armacor M under dry sliding has been proposed to be a combination of adhesive and mild oxidative wear.

5. The metamorphic transformation did not occur in the Armacor M alloy fabricated by SPS because of the absence of boron in the solid solution phase.

Acknowledgments

We gratefully acknowledge funding from the Canadian Foundation for Innovation. Thanks are also expressed to Liquidmetal Coatings for the supply of the Armacor M powder. We also acknowledge King Fahd University of Petroleum and Minerals (KFUPM), Dhahran, Saudi Arabia for the scholarship awarded to A.A. Sorour.

CHAPTER 8

Final Conclusions

8.1 General Summary

The Fe-28.2Cr-3.8B-1.5Si-1.5Mn (wt.%) cored wire was deposited onto 1020 carbon steel substrate using the CSC-MIG welding process with three deposition conditions. The Fe–45Cr–5.9B–2Si–0.1C (wt.%) gas-atomized powder was consolidated using the SPS process. The main objective of this research was to study the microstructure and tribology of these fabricated alloys. The major findings obtained in the previous studies (Chapters 4–7) can be summarized as follows:

1. The alloy was successfully deposited and bonded metallurgically onto carbon steel using the CSC-MIG welding process. The weldment was continuous and contained neither cracks or spatter, which form with conventional welding processes, nor oxides or porosity, which are often observed with thermal spray processes. The powder was successfully solid-state sintered using the SPS process in a short period of time because of the current enhancement.

2. The solidification of the alloy started with the formation of the primary $(Cr,Fe)_2B$ phase, followed by the eutectic formation of $(Cr,Fe)_2B$ and the BCC phase. Because the powder contained a small amount of C, $(Cr,Fe)_7C_3$ was precipitated at the end of solidification. The exact composition and fraction of the phases were predicted by thermodynamic calculations.

3. The alloy fabricated by CSC-MIG contained 44 wt.% primary and secondary $(Cr,Fe)_2B$ plates as well as the 56 wt.% BCC Fe-based solid solution phase containing Fe, Cr, Mn and Si. The welding heat input did not change the morphology of the phases.

4. The sintered powder was composed of the 65 wt.% $(Cr,Fe)_2B$ plates and 1 wt.% $(Cr,Fe)_7C_3$ precipitates dispersed in the 34 wt.% BCC Fe-based solid solution matrix containing Cr and Si. The sintering by SPS did not change the fraction, shape and aspect ratio of $(Cr,Fe)_2B$.

5. The size of $(Cr,Fe)_2B$ plates varied as a function of composition and process parameters. The weldment had bigger $(Cr,Fe)_2B$ plates than the powder and sintered specimen.

6. The fraction of the $(Cr,Fe)_2B$ phase was determined by the B content. As the B content increased, the volume fraction of $(Cr,Fe)_2B$ increased. Thus, weld dilution should be carefully considered when designing the welding or coating.

7. The hardness of $(Cr,Fe)_2B$ was about 24 GPa. It was independent of the alloy's composition and process parameters.

8. Bulk hardness of the fabricated alloys was mainly affected by the fraction of $(Cr,Fe)_2B$. As the fraction increased, the hardness increased.

9. Abrasive wear resistance increased as the hardness and reinforcement size increased. However, the sliding wear resistance mainly increases as the reinforcement size increases.

10. For the range of testing conditions and the fabricated materials studied in this research, the abrasive wear mechanism was microcutting, while the dominant wear mechanisms were adhesion and mild oxidation

8.2 Contributions to Original Knowledge

This section presents the most important contributions of this research work to current scientific knowledge.

1. It was the first attempt the Fe–Cr–B-based alloy was fabricated using the CSC-MIG welding process. The results showed that CSC-MIG produced better weldment quality of this alloy than the ones fabricated by the currently used thermal spray and conventional welding processes. The CSC-MIG welding could replace the currently used processes.

2. The SPS process was used, for the first time, to consolidate the Fe–Cr–B-based alloy powder. The instantaneous application of current and pressure was successfully able to fully densify the powder with solid-state mechanism for a short period of time.

3. While part of the liquidus surface projection diagram of the ternary Fe–Cr–B system has been calculated and reported before, more information was calculated to cover the full range of Cr and up to 30 at.% B. This diagram provides important and useful solidification information of this system for future research.

4. The solidification behavior of the Fe–Cr–B-based alloys fabricated by gas atomization and CSC-MIG as well as the phases' fraction and composition were modeled for the first time using numerical thermodynamic calculation based on the Scheil-Gulliver model.

5. The constitutive models and yielding criterion were improved by considering, for the first time, the effect of the reinforcement phase to describe the overall spark plasma sintering of this MMC. This model helps us to understand the effect of the process parameters (pressure and temperature) and composite properties (fraction and aspect ratio of the reinforcements) on densification and determines which densification mechanisms are dominant during sintering.

6. A state-of-the-art SEM with the latest attached EDS and other detectors were used to characterize the fabricated alloy, and they provided new results. While a TEM has detected stacking faults within the $(Cr,Fe)_2B$ phase, this advanced SEM was able to detect similar stacking faults with the thin foil specimen. In addition, similar defects at larger scales were observed for the first time and were identified as twinning. Moreover, explanations for the cause of formation of these defects were provided.

7. The hardness of $(Cr,Fe)_2B$ was measured previously by Vickers microhardness but its value was not true because of the effect of the matrix's hardness. In this research, the hardness of $(Cr,Fe)_2B$ was accurately measured by nanoindentation, by eliminating the effect of the matrix's hardness since the indentation depth (about 100 nm) was much smaller than the $(Cr,Fe)_2B$ thickness (about 1 µm). In addition, the hardness of the matrix was accurately measured.

8.3 Recommendations for Future Research

The Fe–Cr–B-based alloys in this research showed a high potential to reduce losses in high-wear applications because of their high hardness, high wear resistance, toughness and easy fabrication using the proposed fabrication processes. Based on the findings of this study, future research directions of these alloys can be suggested to further understand this alloy as follows:

1. The wear resistance of Fe–Cr–B-based alloys has been shown to be improved as the $(Cr,Fe)_2B$ size increases. Heat treatment can increase its size but changes the shape from plate-like to sphere-like, which may reduce the resistance. It is suggested to study the effect of heat treatment of these alloys on the microstructure and tribology.

2. The fabricated alloys in this study showed high wear resistance. However, researchers found that when the Fe–Cr–B-based alloys are fabricated by high solidification rate processes, their crystalline outer surface layer can be transformed into amorphous during wear. This amorphous layer has been suggested to improve wear resistance further. In this study, the amorphous layer did not form because of the relatively slow solidification rate. It is suggested to fabricate this alloy using rapid solidification processes, such as laser remelting and electrospark deposition, or by deformation induced processes, such as cold spray. These processes would produce a very fine, or even an amorphous, matrix with embedded nano-size $(Cr,Fe)_2B$ particles. Studying their tribology and correlating it with microstructure and other properties would help to sort them

using the ones fabricated here and in the literature. The matrix would be supersaturated with B, which may facilitate the metamorphic transformation.

3. Study and correlate the hardness, tribology and microstructure before and after wear of this alloy with varying compositions and process parameters to better understand how to improve mechanical and tribological properties.

4. The densification of the Fe–Cr–B-based alloy powder during the SPS process was modeled. By incorporating this model with thermodynamic, high temperature strength, hardness and abrasive wear models, quantitative relationships can be established between processing, structure, properties and performance of this alloy as processed by SPS.

5. In this research, the wear testing was performed with about 1 N normal load. It is suggested to perform wear tests at higher loads (5–50 N) and longer durations to investigate the possibility of using these alloys in more severe applications. In addition, lubrication sliding wear should be studied to understand the behavior of these alloy in such applications.

References

[1] D. Scott, *Industrial Tribology—The Practical Aspects of Friction, Lubrication and Wear*, vol. 8. Elsevier, 1983.

[2] B. Bhushan, *Introduction to Tribology*. John Wiley & Sons, New York, 2002.

[3] A. Albagachiev, B. Gurskii, Y. Luzhnov, A. Romanova, and A. Chichinadze, "Economic and ecological issues in tribology," *Russian Engineering Research*, vol. 28, no. 10, pp. 959–964, 2008.

[4] I. Tzanakis, M. Hadfield, B. Thomas, S. Noya, I. Henshaw, and S. Austen, "Future perspectives on sustainable tribology," *Renewable and Sustainable Energy Reviews*, vol. 16, no. 6, pp. 4126–4140, 2012.

[5] "Chapter 1 introduction," in *Coatings Tribology Properties, Techniques and Applications in Surface Engineering* (K. Holmberg and A. Matthews, eds.), vol. 28 of *Tribology Series*, pp. 1 – 6, Elsevier, 1994.

[6] M. Rosso, "Ceramic and metal matrix composites: Routes and properties," *Journal of Materials Processing Technology*, vol. 175, no. 13, pp. 364–375, 2006.

[7] K. H. Z. Gahr, "Wear by hard particles," *Tribology International*, vol. 31, no. 10, pp. 587 – 596, 1998.

[8] K. Lee, D.-H. Nam, S. Lee, and C. P. Kim, "Hardness and wear resistance of steel-based surface composites fabricated with Fe-based metamorphic alloy powders by high-energy electron beam irradiation," *Materials Science and Engineering: A*, vol. 428, no. 12, pp. 124–134, 2006.

[9] H.-J. Kim, S. Grossi, and Y.-G. Kweon, "Characterization of Fe–Cr–B based coatings produced by HVOF and PTA processes," *Metals and Materials*, vol. 5, no. 1, pp. 63–72, 1999.

[10] H.-J. Kim, B.-H. Yoon, and C.-H. Lee, "Wear performance of the Fe-based alloy coatings produced by plasma transferred arc weld-surfacing process," *Wear*, vol. 249, no. 1011, pp. 846–852, 2001.

[11] C.-Y. Son, T. Yoon, and S. Lee, "Correlation of microstructure with hardness, wear resistance, and corrosion resistance of powder-injection-molded specimens of Fe-alloy powders," *Metallurgical and Materials Transactions A*, vol. 40, no. 5, pp. 1110–1117, 2009.

[12] J. Do, H.-J. Lee, C. Jeon, D. Ha, C. Kim, B.-J. Lee, S. Lee, and Y. Shin, "Effects of Cr and B contents on volume fraction of $(Cr,Fe)_2B$ and hardness in Fe-based alloys used for powder injection molding," *Metallurgical and Materials Transactions A*, vol. 43, no. 7, pp. 2237–2250, 2012.

[13] H. W. Jin, Y. M. Rhyim, C. G. Park, and M. C. Kim, "Microstructure and wear-resistance of Fe–Cr–B base metamorphic alloys," *Metals and Materials-korea*, vol. 3, no. 1, pp. 60–64, 1997.

[14] A. H. Dent, A. J. Horlock, D. G. McCartney, and S. J. Harris, "The structure and properties of two Fe–Cr–B based coatings sprayed using HVOF," in *Thermal spray forum*, pp. 917–923, 1997.

[15] C. K. Kim, C.-Y. Son, D. J. Ha, T. S. Yoon, S. Lee, and N. J. Kim, "Microstructure and mechanical properties of powder-injection-molded products of Cu-based amorphous powders and Fe-based metamorphic powders," *Materials Science and Engineering: A*, vol. 476, no. 12, pp. 69 – 77, 2008.

[16] D. Branagan, W. Swank, D. Haggard, and J. Fincke, "Wear-resistant amorphous and nanocomposite steel coatings," *Metallurgical and Materials Transactions A*, vol. 32, no. 10, pp. 2615–2621, 2001.

[17] K. Lee, D.-H. Nam, and S. Lee, "Correlation of microstructure with hardness and wear resistance in (CrB, MoB)/steel surface composites fabricated by high-energy electron beam irradiation," *Metallurgical and Materials Transactions A*, vol. 37, no. 3, pp. 663–673, 2006.

[18] K. Venugopal and M. Agrawal, "Evaluation of arc sprayed coatings for erosion protection of tubes in atmospheric fluidised bed combustion (AFBC) boilers," *Wear*, vol. 264, no. 12, pp. 139 – 145, 2008.

[19] D. Scruggs, "The tribology of amorphous surfaces formed by wear of thermal spray coatings," vol. 1, pp. 249–252, 1998.

[20] H.-J. Kim, S. Grossi, and Y.-G. Kweon, "Wear performance of metamorphic alloy coatings," *Wear*, vol. 232, no. 1, pp. 51 – 60, 1999.

[21] G. Bolelli, B. Bonferroni, J. Laurila, L. Lusvarghi, A. Milanti, K. Niemi, and P. Vuoristo, "Micromechanical properties and sliding wear behaviour of hvof-sprayed fe-based alloy coatings," *Wear*, vol. 276277, no. 0, pp. 29 – 47, 2012.

[22] K. Chokethawai, D. McCartney, and P. Shipway, "Microstructure evolution and thermal stability of an fe-based amorphous alloy powder and thermally sprayed coatings," *Journal of Alloys and Compounds*, vol. 480, no. 2, pp. 351 – 359, 2009.

[23] H. W. Jin, C. G. Park, and M. C. Kim, "Friction-induced amorphous phase formation observed in Fe–Cr–B–Ni–Mo alloy thermal spray coatings," *Scripta Materialia*, vol. 41, no. 6, pp. 589 – 595, 1999.

[24] H. W. Jin, C. G. Park, and M. C. Kim, "Microstructure and amorphization induced by frictional work in Fe–Cr–B alloy thermal spray coatings," *Surface and Coatings Technology*, vol. 113, no. 1-2, pp. 103 – 112, 1999.

[25] H. Jin, C. Park, and M. Kim, "In situ TEM heating studies on the phase transformation of metastable phases in Fe–Cr–B alloy spray coatings," *Materials Science and Engineering: A*, vol. 304–306, no. 0, pp. 321–326, 2001.

[26] E. Yun and S. Lee, "Improvement of hardness and wear resistance in stainless-steel-based surface composites fabricated by high-energy electron beam irradiation," *Surface and Coatings Technology*, vol. 200, no. 11, pp. 3478–3485, 2006.

[27] J. Do, C. Jeon, C. P. Kim, B.-J. Lee, S. Lee, E.-S. Lee, T. S. Yoon, and Y. S. Shin, "Effects of $(Cr,Fe)_2B$ borides on hardness in powder-injection-molded product fabricated with Fe-based alloy powders," *Materials Science and Engineering: A*, vol. 556, pp. 366–372, 2012.

[28] T. B. Sercombe and G. B. Schaffer, "The sintering of an Fe–Cr–Ni–B–C powder," *Materials Science and Engineering: A*, vol. 528, no. 2, pp. 751–755, 2010.

[29] A. Rottger, S. Weber, and W. Theisen, "Supersolidus liquid-phase sintering of ultrahigh-boron high-carbon steels for wear-protection applications," *Materials Science and Engineering: A*, vol. 532, no. 0, pp. 511–521, 2012.

[30] J. Cabral Miramontes, J. Barceinas Snchez, F. Almeraya Caldern, A. Martnez Villafae, and J. Chacn Nava, "Effect of boron additions on sintering and densification of a ferritic stainless steel," *Journal of Materials Engineering and Performance*, vol. 19, no. 6, pp. 880–884, 2010.

[31] G. Huismann, "Direct control of the material transfer, the Controlled Short Circuiting (CSC)-MIG process," in *Proceeding of the Gas Metal Arc Welding for 21st Century Conference, Orlando, Florida, USA*, pp. 165–172, 2000.

[32] Z. A. Munir, U. Anselmi-Tamburini, and M. Ohyanagi, "The effect of electric field and pressure on the synthesis and consolidation of materials: A review of the spark plasma sintering method," *Journal of Materials Science*, vol. 41, no. 3, pp. 763–777, 2006.

[33] R. Orru, R. Licheri, A. M. Locci, A. Cincotti, and G. Cao, "Consolidation/synthesis of materials by electric current activated/assisted sintering," *Materials Science and Engineering: R: Reports*, vol. 63, no. 46, pp. 127–287, 2009.

[34] Z. A. Munir, D. V. Quach, and M. Ohyanagi, "Electric current activation of sintering: A review of the pulsed electric current sintering process," *Journal of the American Ceramic Society*, vol. 94, no. 1, pp. 1–19, 2011.

[35] H. Granjon, *Fundamentals of Welding Metallurgy*. Abington Pub., Cambridge, England, 1st ed., 1991.

[36] S. Kou, *Welding Metallurgy*. Wiley-Interscience, 2nd ed., 2003.

[37] J. Norrish and D. Cuiuri, "The controlled short circuit GMAW process: A tutorial," *Journal of Manufacturing Processes*, no. 0, 2013.

[38] K. Furukawa, "New CMT arc welding process—welding of steel to aluminium dissimilar metals and welding of super-thin aluminium sheets," *Welding International*, vol. 20, no. 6, pp. 440–445, 2006.

[39] T. Hungria, J. Galy, and A. Castro, "Spark plasma sintering as a useful technique to the nanostructuration of piezo-ferroelectric materials," *Advanced Engineering Materials*, vol. 11, no. 8, pp. 615–631, 2009.

[40] J. Garay, "Current-activated, pressure-assisted densification of materials," *Annual Review of Materials Research*, vol. 40, no. 1, pp. 445–468, 2010.

[41] Z. Zhaohui, W. Fuchi, W. Lin, L. Shukui, and S. Osamu, "Sintering mechanism of large-scale ultrafine-grained copper prepared by SPS method," *Materials Letters*, vol. 62, no. 24, pp. 3987 – 3990, 2008.

[42] A. Helle, K. Easterling, and M. Ashby, "Hot-isostatic pressing diagrams: New developments," *Acta Metallurgica*, vol. 33, no. 12, pp. 2163–2174, 1985.

[43] E. Olevsky and L. Froyen, "Constitutive modeling of spark-plasma sintering of conductive materials," *Scripta Materialia*, vol. 55, no. 12, pp. 1175–1178, 2006.

[44] J. Milligan, R. Gauvin, and M. Brochu, "Consolidation of cryomilled Al–Si using spark plasma sintering," *Philosophical Magazine*, vol. 93, no. 19, pp. 2445–2464, 2013.

[45] C. Guo and P. Kelly, "Boron solubility in Fe–Cr–B cast irons," *Materials Science and Engineering: A*, vol. 352, no. 12, pp. 40–45, 2003.

[46] B. E. Brown and D. J. Beerntsen, "Refinement of an iron chromium boride with the Mn_4B structure," *Acta Crystallographica*, vol. 17, no. 4, pp. 448–450, 1964.

[47] B. Aronsson, "The crystal structure of Mo_5SiB_2," *Acta Chemica Scandinavica*, vol. 12, no. 1, pp. 31–37, 1958.

[48] P. Christodoulou and N. Calos, "A step towards designing Fe–Cr–B–C cast alloys," *Materials Science and Engineering: A*, vol. 301, no. 2, pp. 103–117, 2001.

[49] A. Bondar, "Boron–Chromium–Iron," in *Iron Systems, Part 1* (G. Effenberg and S. Ilyenko, eds.), vol. 11D1 of *Landolt-Brnstein - Group IV Physical Chemistry*, pp. 403–432, Springer Berlin Heidelberg, 2008.

[50] M. Borlera and G. Pradelli, "On the system Iron-Chromium-Boron. reports about solid state equilibria in the system at 1250 C (in italian)," *Metall. Ital.*, vol. 65, no. 7–8, pp. 421–424, 1973.

[51] C. Gianoglio, G. Pradelli, and M. Vallino, "Solid state equilibria in the Cr-Fe-B system at the temperature of 1373 k," *Metall. Sci. Technol.*, vol. 1, no. 2, pp. 51–57, 1983.

[52] A. Gorbunov and F. M. Boduryan, "On phase equilibria in the ternary system Chromium-Boron-Iron," *Metallurgiya (in Russian)*, vol. 16, pp. 172–178, 1976.

[53] M. Chepiga and Y. B. Kuzma, "Phase equilibria in the Chromium-Iron-Boron system," *Izv. VUZ Chern. Metall. (in Russian)*, vol. 3, pp. 127–130, 1970.

[54] H. Kaneko, T. Nishizawa, and A. Chiba, "Borides in stainless steel," *Nippon Kinzoku Gakkai-Si (J. Jpn. Inst. Met.) (in Japanese)*, vol. 30, no. 2, pp. 157–163, 1966.

[55] I. Ozbek, S. Sen, M. Ipek, C. Bindal, S. Zeytin, and A. H. Ucisik, "A mechanical aspect of borides formed on the AISI 440C stainless-steel," *Vacuum*, vol. 73, no. 34, pp. 643 – 648, 2004.

[56] F. X. Kayser and G. F. Kayser, "A re-examination of the Kraft and Flinn diffraction data for Cr_2B, $(Cr,Fe)_2B$, and the boride phase in Fe + 18.5 wt % Ni + 20 wt % Cr + B alloys," *Journal of Materials Science*, vol. 34, no. 6, pp. 1271–1275, 1999.

[57] J. W. Yoo, S. H. Lee, C. S. Yoon, and S. J. Kim, "The effect of boron on the wear behavior of iron-based hardfacing alloys for nuclear power plants valves," *Journal of Nuclear Materials*, vol. 352, no. 13, pp. 90–96, 2006.

[58] I. Manna, P. Chattopadhyay, F. Banhart, J. Croopnick, and H.-J. Fecht, "Microstructural evolution of wear-resistant FeCrB and FeCrNiCoB coating alloys during high-energy mechanical attrition," *Wear*, vol. 264, pp. 940–946, 2008.

[59] C. Guo and P. M. Kelly, "Modeling of spatial distribution of the eutectic M_2B borides in Fe–Cr–B cast irons," *Journal of Materials Science*, vol. 39, no. 3, pp. 1109–1111, 2004.

[60] K. H. Zum Gahr, *Microstructure and wear of materials*, vol. 10. Elsevier, North Holland, Amsterdam, 1987.

[61] J. R. Davis, *Surface Engineering for Corrosion and Wear Resistance*. ASM International, Materials Park, OH, 2001.

[62] "Chapter 3 tribology of coatings," in *Coatings Tribology Properties, Techniques and Applications in Surface Engineering* (K. Holmberg and A. Matthews, eds.), vol. 28 of *Tribology Series*, pp. 33 – 124, Elsevier, 1994.

[63] K. H. Zum Gahr, "Modelling of two-body abrasive wear," *Wear*, vol. 124, no. 1, pp. 87 – 103, 1988.

[64] N. Axn and S. Jacobson, "A model for the abrasive wear resistance of multiphase materials," *Wear*, vol. 174, no. 12, pp. 187 – 199, 1994.

[65] D. Yi, J. Xing, S. Ma, H. Fu, Y. Li, W. Chen, J. Yan, J. Zhang, and R. Zhang, "Investigations on microstructures and two-body abrasive wear behavior of Fe–B cast alloy," *Tribology Letters*, vol. 45, no. 3, pp. 427–435, 2012.

[66] D. M. Scruggs, "Materials transformable from the nonamorphous to the amorphous state under frictional loadings," 1988. US Patent 4,725,512.

[67] R. B. Schwarz and W. L. Johnson, "Formation of an amorphous alloy by solid-state reaction of the pure polycrystalline metals," *Phys. Rev. Lett.*, vol. 51, pp. 415–418, Aug 1983.

[68] T. Egami and Y. Waseda, "Atomic size effect on the formability of metallic glasses," *Journal of Non-Crystalline Solids*, vol. 64, no. 12, pp. 113 – 134, 1984.

[69] S. Ma, J. Xing, D. Yi, H. Fu, J. Zhang, Y. Li, Z. Zhang, G. Liu, and B. Zhu, "Effects of chromium addition on corrosion resistance of Fe–3.5B alloy in liquid zinc ," *Surface and Coatings Technology*, vol. 205, no. 2122, pp. 4902–4909, 2011.

[70] S. Ma, J. Xing, H. Fu, D. Yi, J. Zhang, Y. Li, Z. Zhang, B. Zhu, and S. Ma, "Interfacial morphology and corrosion resistance of Fe–B cast steel containing chromium and nickel in liquid zinc," *Corrosion Science*, vol. 53, no. 9, pp. 2826–2834, 2011.

[71] P. Vespa, P. Pinard, R. Gauvin, and M. Brochu, "Analysis of WC/Ni-based coatings deposited by controlled short-circuit MIG welding," *Journal of Materials Engineering and Performance*, vol. 21, no. 6, pp. 865–876, 2012.

[72] B. Rupp, "XLAT—a microcomputer program for the refinement of cell constants," *Scripta Metallurgica*, vol. 22, pp. 69–92, 1988.

[73] C. W. Bale, E. Blisle, P. Chartrand, S. A. Decterov, G. Eriksson, K. Hack, I. H. Jung, Y. B. Kang, J. Melanon, A. D. Pelton, C. Robelin, and S. Petersen, "FactSage thermochemical software and databases—recent developments," *Calphad*, vol. 33, no. 2, pp. 295 – 311, 2009.

[74] M. Hillert, B. Jansson, and B. Sundman, "Application of the compound energy model to oxide systems," *Z. Metallkd.*, vol. 79, no. 2, pp. 81–87, 1988.

[75] E. Scheil, "Bemerkungen zur schichtkristallbildung," *Zeitschrift fr Metallkunde*, vol. 34, pp. 70–72, 1942.

[76] G. Gulliver, "The quantitative effect of rapid cooling upon the constitution of binary alloys," *The journal of the institute of metals*, vol. 9, pp. 120–157, 1913.

[77] H. E. Swanson, R. K. Fuyat, and G. M. Ugrinic, "Standard X-ray diffraction powder patterns," 1955.

[78] P. Villars, A. Prince, and H. Okamoto, *Handbook of Ternary Alloy Phase Diagrams*. ASM International, Materials Park, OH, 1995.

[79] D. W. Heard, S. Brophy, and M. Brochu, "Solid freeform fabrication of Al-Si components via the CSC-MIG process," *Canadian Metallurgical Quarterly*, vol. 51, no. 3, pp. 302–312, 2012.

[80] J. D. Robson and P. B. Prangnell, "Modelling Al_3Zr dispersoid precipitation in multicomponent aluminium alloys," *Materials Science and Engineering A*, vol. 352, no. 12, pp. 240–250, 2003.

[81] A. Heckl, R. Rettig, and R. Singer, "Solidification characteristics and segregation behavior of nickel-base superalloys in dependence on different rhenium and ruthenium contents," *Metallurgical and Materials Transactions A*, vol. 41, no. 1, pp. 202–211, 2010.

[82] Y. F. Cui, X. Zhang, G. L. Xu, W. J. Zhu, H. S. Liu, and Z. P. Jin, "Thermodynamic assessment of Co–Al–W system and solidification of Co-enriched ternary alloys," *Journal of Materials Science*, vol. 46, no. 8, pp. 2611–2621, 2011.

[83] F. Huang, X. Wang, J. Zhang, C. Ji, Y. Fang, and Y. Yu, "In situ observation of solidification process of AISI 304 austenitic stainless steel," *Journal of Iron and Steel Research*, vol. 15, no. 6, pp. 78–82, 2008.

[84] E. Clementi, D. L. Raimondi, and W. P. Reinhardt, "Atomic Screening Constants from SCF Functions. II. Atoms with 37 to 86 Electrons," *The Journal of Chemical Physics*, vol. 47, no. 4, pp. 1300–1307, 1967.

[85] N. Calos, P. Christodoulou, E. Graham, L. Bekessy, and D. Cousens, *Structural studies of ferrous alloys containing boron.* internal report, The University of Queensland, 1999.

[86] L. Yijian and H. Jian, "Borides in microcrystalline Fe–Cr–Mo–B–Si alloys," *Journal of Materials Science*, vol. 26, no. 10, pp. 2833–2840, 1991.

[87] I. Goldfarb, W. D. Kaplan, S. Ariely, and M. Bamberger, "Fault-induced polytypism in $(Cr,Fe)_2B$," *Philosophical Magazine A*, vol. 72, no. 4, pp. 963–979, 1995.

[88] D. Drouin, A. R. Couture, D. Joly, X. Tastet, V. Aimez, and R. Gauvin, "CASINO V2.42—A fast and easy-to-use modeling tool for scanning electron microscopy and microanalysis users," *Scanning*, vol. 29, no. 3, pp. 92–101, 2007.

[89] S. Ma, J. Xing, H. Fu, Y. Gao, and J. Zhang, "Microstructure and crystallography of borides and secondary precipitation in 18 Cr–4 Ni–1 Mo–3.5 B–0.27 C steel," *Acta Materialia*, vol. 60, no. 3, pp. 831–843, 2012.

[90] M. Shamsuzzoha and L. M. Hogan, "Twinning in fibrous eutectic silicon in modified Al–Si Alloys," *Journal of Crystal Growth*, vol. 72, no. 3, pp. 735 – 737, 1985.

[91] M. Shamsuzzoha and L. M. Hogan, "Crystal morphology of unmodified aluminium-silicon eutectic microstructures," *Journal of Crystal Growth*, vol. 76, no. 2, pp. 429 – 439, 1986.

[92] H. R. Zhang and O. A. Ojo, "Cr-rich nanosize precipitates in a standard heat-treated Inconel 738 superalloy," *Philosophical Magazine*, vol. 90, no. 6, pp. 765–782, 2010.

[93] W. Dudzinski, J. P. Morniroli, and M. Gantois, "Stacking faults in chromium, iron and vanadium mixed carbides of the type M_7C_3," *Journal of Materials Science*, vol. 15, no. 6, pp. 1387–1401, 1980.

[94] A. Genc, R. Banerjee, D. Hill, and H. L. Fraser, "Structure of TiB precipitates in laser deposited in situ, Ti–6Al–4V–TiB composites," *Materials Letters*, vol. 60, no. 7, pp. 859 – 863, 2006.

[95] M. M. Gauthier, *Crystallography and Engineering Properties of Ceramics: Engineering Properties of Borides: Engineering Property Data, Engineered Materials Handbook Desk Edition, www.asminternational.org.* ASM International, 1995.

[96] R. L. Deuis, C. Subramanian, and J. M. Yellup, "Abrasive wear of aluminium composites—a review," *Wear*, vol. 201, no. 12, pp. 132 – 144, 1996.

[97] M. R. Thakare, J. A. Wharton, R. J. K. Wood, and C. Menger, "Effect of abrasive particle size and the influence of microstructure on the wear mechanisms in wear-resistant materials," *Wear*, vol. 276277, no. 0, pp. 16 – 28, 2012.

[98] W. C. Oliver and G. M. Pharr, "An improved technique for determining hardness and elastic modulus using load and displacement sensing indentation experiments," *Journal of Materials Research*, vol. 7, pp. 1564–1583, 1992.

[99] R. R. Chromik, H. W. Strauss, and T. W. Scharf, "Materials phenomena revealed by insitu tribometry," *JOM*, vol. 64, no. 1, pp. 35–43, 2012.

[100] "ASTM Standard G174: Standard test method for measuring abrasion resistance of materials by abrasive loop contact," 2009.

[101] W. Yan, C. L. Pun, Z. Wu, and G. P. Simon, "Some issues on nanoindentation method to measure the elastic modulus of particles in composites," *Composites Part B: Engineering*, vol. 42, no. 8, pp. 2093 – 2097, 2011.

[102] W. Yan, C. L. Pun, and G. P. Simon, "Conditions of applying Oliver-Pharr method to the nanoindentation of particles in composites," *Composites Science and Technology*, vol. 72, no. 10, pp. 1147 – 1152, 2012.

[103] S. C. Lim and M. F. Ashby, "Wear-mechanism maps," *Acta Metallurgica*, vol. 35, no. 1, pp. 1 – 24, 1987.

[104] Y. Sahin and V. Kilicli, "Abrasive wear behaviour of SiCp/Al alloy composite in comparison with ausferritic ductile iron," *Wear*, vol. 271, no. 1112, pp. 2766 – 2774, 2011.

[105] R. L. Deuis, C. Subramanian, and J. M. Yellup, "Three-body abrasive wear of composite coatings in dry and wet environments," *Wear*, vol. 214, no. 1, pp. 112 – 130, 1998.

[106] N. Axen and S. Jacobson, "Transitions in the abrasive wear resistance of fibre- and particle-reinforced aluminium," *Wear*, vol. 178, no. 12, pp. 1 – 7, 1994.

[107] M. M. Khruschov, "Principles of abrasive wear," *Wear*, vol. 28, no. 1, pp. 69 – 88, 1974.

[108] C. Garca-Cordovilla, J. Narciso, and E. Louis, "Abrasive wear resistance of aluminium alloy/ceramic particulate composites," *Wear*, vol. 192, no. 12, pp. 170 – 177, 1996.

[109] O. A. Graeve, R. Kanakala, L. Kaufman, K. Sinha, E. Wang, B. Pearson, G. Rojas-George, and J. C. Farmer, "Spark plasma sintering of Fe-based structural amorphous metals (SAM) with Y2O3 nanoparticle additions," *Materials Letters*, vol. 62, no. 1718, pp. 2988–2991, 2008.

[110] J. Kim, H. Ryu, J. Kim, B. Kim, Y. Kim, and H. Kim, "Synthesis and densification of Cu added Fe-based BMG composite powders by gas atomization and electrical explosion of wire," *Journal of Alloys and Compounds*, vol. 483, no. 12, pp. 28–31, 2009.

[111] S. P. Harimkar, S. R. Paital, A. Singh, R. Aalund, and N. B. Dahotre, "Microstructure and properties of spark plasma sintered Fe–Cr–Mo–Y–B–C bulk metallic glass," *Journal of Non-Crystalline Solids*, vol. 355, no. 4344, pp. 2179–2182, 2009.

[112] G. Xie, H. Kimura, D. V. Louzguine-Luzgin, H. Men, and A. Inoue, "SiC dispersed Fe-based glassy composite cores produced by spark plasma sintering and their high frequency magnetic properties," *Intermetallics*, vol. 20, no. 1, pp. 76–81, 2012.

[113] E. Lavernia and N. Grant, "Spray deposition of metals: A review," *Materials Science and Engineering*, vol. 98, no. 0, pp. 381–394, 1988.

[114] E. A. Olevsky, S. Kandukuri, and L. Froyen, "Consolidation enhancement in spark-plasma sintering: Impact of high heating rates," *Journal of Applied Physics*, vol. 102, no. 11, pp. 1–11, 2007.

[115] N. Bertolino, J. Garay, U. Anselmi-Tamburini, and Z. Munir, "Electromigration effects in al-au multilayers," *Scripta Materialia*, vol. 44, no. 5, pp. 737 – 742, 2001.

[116] P. Asoka-Kumar, M. Alatalo, V. J. Ghosh, A. C. Kruseman, B. Nielsen, and K. G. Lynn, "Increased elemental specificity of positron annihilation spectra," *Phys. Rev. Lett.*, vol. 77, pp. 2097–2100, 1996.

[117] J. E. Garay, S. C. Glade, U. Anselmi-Tamburini, P. Asoka-Kumar, and Z. Munir, "Electric current enhanced defect mobility in Ni_3Ti intermetallics," *Applied Physics Letters*, vol. 85, no. 4, pp. 573–575, 2004.

[118] E. A. Olevsky and L. Froyen, "Impact of thermal diffusion on densification during sps," *Journal of the American Ceramic Society*, vol. 92, pp. 122–132, 2009.

[119] E. Arzt, M. Ashby, and K. Easterling, "Practical applications of hotisostatic pressing diagrams: Four case studies," *Metallurgical Transactions A*, vol. 14, no. 1, pp. 211–221, 1983.

[120] H. J. Frost and M. F. Ashby, *Deformation mechanism maps: the plasticity and creep of metals and ceramics*. Pergamon press, 1982.

[121] N. Saunders, Z. Guo, X. Li, A. Miodownik, and J.-P. Schill, "Using JMatPro to model materials properties and behavior," *JOM*, vol. 55, no. 12, pp. 60–65, 2003.

[122] D. Morris, M. Muoz-Morris, and C. Baudin, "The high-temperature strength of some Fe_3Al alloys," *Acta Materialia*, vol. 52, no. 9, pp. 2827–2836, 2004.

[123] R. C. Dimitriu and H. K. D. H. Bhadeshia, "Hot strength of creep resistant ferritic steels and relationship to creep rupture data.," *Materials Science & Technology*, vol. 23, no. 9, pp. 1127–1131, 2007.

[124] Z. Xiong, L. Geng, and C. Yao, "Investigation of high-temperature deformation behavior of a SiC whisker reinforced 6061 aluminium composite," *Composites Science and Technology*, vol. 39, no. 2, pp. 117–125, 1990.

[125] K. Matsugi, H. Kuramoto, T. Hatayama, and O. Yanagisawa, "Temperature distribution at steady state under constant current discharge in spark sintering process of Ti and Al_2O_3 powders," *Journal of Materials Processing Technology*, vol. 134, no. 2, pp. 225 – 232, 2003.

[126] A. Zavaliangos, J. Zhang, M. Krammer, and J. R. Groza, "Temperature evolution during field activated sintering," *Materials Science and Engineering: A*, vol. 379, no. 12, pp. 218–228, 2004.

[127] C. Wang, L. Cheng, and Z. Zhao, "FEM analysis of the temperature and stress distribution in spark plasma sintering: Modelling and experimental validation," *Computational Materials Science*, vol. 49, no. 2, pp. 351–362, 2010.

[128] V. Mamedov, "Spark plasma sintering as advanced PM sintering method," *Powder Metallurgy*, vol. 45, no. 4, pp. 322–328, 2002.

[129] R. Vintila, A. Charest, R. A. L. Drew, and M. Brochu, "Synthesis and consolidation via spark plasma sintering of nanostructured Al-5356/B4C composite," *Materials Science and Engineering: A*, vol. 528, no. 13-14, pp. 4395 – 4407, 2011.

[130] A. C. Fischer-Cripps, *Nanoindentation*. Springer, New York, 2004.

[131] R. R. Chromik, R. P. Vinci, S. L. Allen, and M. R. Notis, "Nanoindentation measurements on Cu-Sn and Ag-Sn intermetallics formed in Pb-free solder joints," *Journal of Materials Research*, vol. 18, pp. 2251–2261, 2003.

[132] H. W. Strauss, R. R. Chromik, S. Hassani, and J. E. Klemberg-Sapieha, "In situ tribology of nanocomposite Ti–Si–C–H coatings prepared by PE-CVD," *Wear*, vol. 272, no. 1, pp. 133 – 148, 2011.

[133] E. P. Whitenton and P. J. Blau, "A comparison of methods for determining wear volumes and surface parameters of spherically tipped sliders," *Wear*, vol. 124, no. 3, pp. 291 – 309, 1988.

[134] "ASTM Standard G99: Standard test method for wear testing with a pin-on-disk apparatus," 2006.

[135] G. M. Pharr, E. G. Herbert, and Y. Gao, "The indentation size effect: A critical examination of experimental observations and mechanistic interpretations," *Annual Review of Materials Research*, vol. 40, pp. 271 – 292, 2010.

[136] A. L. Greer, K. L. Rutherford, and I. M. Hutchings, "Wear resistance of amorphous alloys and related materials," *International Materials Reviews*, vol. 47, no. 2, pp. 87–112, 2002.

[137] Y. Wang, T. Lei, and J. Liu, "Tribo-metallographic behavior of high carbon steels in dry sliding: I. Wear mechanisms and their transition," *Wear*, vol. 231, no. 1, pp. 1 – 11, 1999.

[138] Y. Wang, T. Lei, and J. Liu, "Tribo-metallographic behavior of high carbon steels in dry sliding: II. Microstructure and wear," *Wear*, vol. 231, no. 1, pp. 12–19, 1999.

[139] C. Navas, I. Garca, X. Ye, J. de Damborenea, and J. Celis, "Role of contact frequency on the wear rate of steel in discontinuous sliding contact conditions," *Wear*, vol. 260, no. 910, pp. 1096 – 1103, 2006.

[140] R. Tyagi, S. K. Nath, and S. Ray, "Dry sliding friction and wear in plain carbon dual phase steel," *Metallurgical and Materials Transactions A*, vol. 32, no. 2, pp. 359–367, 2001.

[141] G. Straffelini, D. Trabucco, and A. Molinari, "Oxidative wear of heat-treated steels," *Wear*, vol. 250, no. 112, pp. 485 – 491, 2001.

[142] A. Leyland and A. Matthews, "On the significance of the H/E ratio in wear control: a nanocomposite coating approach to optimised tribological behaviour," *Wear*, vol. 246, no. 12, pp. 1 – 11, 2000.